Selected for a Viewpoint in *Physics*

PHYSICAL REVIEW C **81**, 034911 (2010)

Detailed measurement of the e^+e^- pair continuum in $p+p$ and Au+Au collisions at $\sqrt{s_{NN}} = 200$ GeV and implications for direct photon production

A. Adare,[9] S. Afanasiev,[23] C. Aidala,[10] N. N. Ajitanand,[50] Y. Akiba,[44,45] H. Al-Bataineh,[39] J. Alexander,[50] A. Al-Jamel,[39] K. Aoki,[29,44] L. Aphecetche,[52] R. Armendariz,[39] S. H. Aronson,[4] J. Asai,[45] E. T. Atomssa,[30] R. Averbeck,[51] T. C. Awes,[40] B. Azmoun,[4] V. Babintsev,[19] G. Baksay,[15] L. Baksay,[15] A. Baldisseri,[12] K. N. Barish,[5] P. D. Barnes,[32] B. Bassalleck,[38] S. Bathe,[5] S. Batsouli,[10,40] V. Baublis,[43] F. Bauer,[5] A. Bazilevsky,[4] S. Belikov,[4,22,*] R. Bennett,[51] Y. Berdnikov,[47] A. A. Bickley,[9] M. T. Bjorndal,[10] J. G. Boissevain,[32] H. Borel,[12] K. Boyle,[51] M. L. Brooks,[32] D. S. Brown,[39] D. Bucher,[35] H. Buesching,[4] V. Bumazhnov,[19] G. Bunce,[4,45] J. M. Burward-Hoy,[32] S. Butsyk,[32,51] S. Campbell,[51] J.-S. Chai,[24] B. S. Chang,[59] J.-L. Charvet,[12] S. Chernichenko,[19] J. Chiba,[25] C. Y. Chi,[10] M. Chiu,[10,20] I. J. Choi,[59] T. Chujo,[56] P. Chung,[50] A. Churyn,[19] V. Cianciolo,[40] C. R. Cleven,[17] Y. Cobigo,[12] B. A. Cole,[10] M. P. Comets,[41] P. Constantin,[22,32] M. Csanád,[14] T. Csörgő,[26] T. Dahms,[51] K. Das,[16] G. David,[4] M. B. Deaton,[1] K. Dehmelt,[15] H. Delagrange,[52] A. Denisov,[19] D. d'Enterria,[10] A. Deshpande,[45,51] E. J. Desmond,[4] O. Dietzsch,[48] A. Dion,[51] M. Donadelli,[48] J. L. Drachenberg,[1] O. Drapier,[30] A. Drees,[51] A. K. Dubey,[58] A. Durum,[19] V. Dzhordzhadze,[5,53] Y. V. Efremenko,[40] J. Egdemir,[51] F. Ellinghaus,[9] W. S. Emam,[5] A. Enokizono,[18,31] H. En'yo,[44,45] B. Espagnon,[41] S. Esumi,[55] K. O. Eyser,[5] D. E. Fields,[38,45] M. Finger Jr.,[6,23] M. Finger,[6,23] F. Fleuret,[30] S. L. Fokin,[28] B. Forestier,[33] Z. Fraenkel,[58,*] J. E. Frantz,[10,51] A. Franz,[4] A. D. Frawley,[16] K. Fujiwara,[44] Y. Fukao,[29,44] S.-Y. Fung,[5] T. Fusayasu,[37] S. Gadrat,[33] I. Garishvili,[53] F. Gastineau,[52] M. Germain,[52] A. Glenn,[9,53] H. Gong,[51] M. Gonin,[30] J. Gosset,[12] Y. Goto,[44,45] R. Granier de Cassagnac,[30] N. Grau,[22] S. V. Greene,[56] M. Grosse Perdekamp,[20,45] T. Gunji,[8] H.-Å. Gustafsson,[34,*] T. Hachiya,[18,44] A. Hadj Henni,[52] C. Haegemann,[38] J. S. Haggerty,[4] M. N. Hagiwara,[1] H. Hamagaki,[8] R. Han,[42] H. Harada,[18] E. P. Hartouni,[31] K. Haruna,[18] M. Harvey,[4] E. Haslum,[34] K. Hasuko,[44] R. Hayano,[8] M. Heffner,[31] T. K. Hemmick,[51] T. Hester,[5] J. M. Heuser,[44] X. He,[17] H. Hiejima,[20] J. C. Hill,[22] R. Hobbs,[38] M. Hohlmann,[15] M. Holmes,[56] W. Holzmann,[50] K. Homma,[18] B. Hong,[27] T. Horaguchi,[44,54] D. Hornback,[53] M. G. Hur,[24] T. Ichihara,[44,45] K. Imai,[29,44] M. Inaba,[55] Y. Inoue,[44,46] D. Isenhower,[1] L. Isenhower,[1] M. Ishihara,[44] T. Isobe,[8] M. Issah,[50] A. Isupov,[23] B. V. Jacak,[51,†] J. Jia,[10] J. Jin,[10] O. Jinnouchi,[45] B. M. Johnson,[4] K. S. Joo,[36] D. Jouan,[41] F. Kajihara,[8,44] S. Kametani,[8,57] N. Kamihara,[44,54] J. Kamin,[51] M. Kaneta,[45] J. H. Kang,[59] H. Kanou,[44,54] T. Kawagishi,[55] D. Kawall,[45] A. V. Kazantsev,[28] S. Kelly,[9] A. Khanzadeev,[43] J. Kikuchi,[57] D. H. Kim,[36] D. J. Kim,[59] E. Kim,[49] Y.-S. Kim,[24] E. Kinney,[9] A. Kiss,[14] E. Kistenev,[4] A. Kiyomichi,[44] J. Klay,[31] C. Klein-Boesing,[35] L. Kochenda,[43] V. Kochetkov,[19] B. Komkov,[43] M. Konno,[55] D. Kotchetkov,[5] A. Kozlov,[58] A. Král,[11] A. Kravitz,[10] P. J. Kroon,[4] J. Kubart,[6,21] G. J. Kunde,[32] N. Kurihara,[8] K. Kurita,[44,46] M. J. Kweon,[27] Y. Kwon,[53,59] G. S. Kyle,[39] R. Lacey,[50] Y.-S. Lai,[10] J. G. Lajoie,[22] A. Lebedev,[22] Y. Le Bornec,[41] S. Leckey,[51] D. M. Lee,[32] M. K. Lee,[59] T. Lee,[49] M. J. Leitch,[32] M. A. L. Leite,[48] B. Lenzi,[48] H. Lim,[49] T. Liška,[11] A. Litvinenko,[23] M. X. Liu,[32] X. Li,[7] X. H. Li,[5] B. Love,[56] D. Lynch,[4] C. F. Maguire,[56] Y. I. Makdisi,[3,4] A. Malakhov,[23] M. D. Malik,[38] V. I. Manko,[28] Y. Mao,[42,44] L. Mašek,[6,21] H. Masui,[55] F. Matathias,[10,51] M. C. McCain,[20] M. McCumber,[51] P. L. McGaughey,[32] Y. Miake,[55] P. Mikeš,[6,21] K. Miki,[55] T. E. Miller,[56] A. Milov,[51] S. Mioduszewski,[4] G. C. Mishra,[17] M. Mishra,[2] J. T. Mitchell,[4] M. Mitrovski,[50] A. Morreale,[5] D. P. Morrison,[4] J. M. Moss,[32] T. V. Moukhanova,[28] D. Mukhopadhyay,[56] J. Murata,[44,46] S. Nagamiya,[25] Y. Nagata,[55] J. L. Nagle,[9] M. Naglis,[58] I. Nakagawa,[44,45] Y. Nakamiya,[18] T. Nakamura,[18] K. Nakano,[44,54] J. Newby,[31] M. Nguyen,[51] B. E. Norman,[32] R. Nouicer,[4] A. S. Nyanin,[28] J. Nystrand,[34] E. O'Brien,[4] S. X. Oda,[8] C. A. Ogilvie,[22] H. Ohnishi,[44] I. D. Ojha,[56] H. Okada,[29,44] K. Okada,[45] M. Oka,[55] O. O. Omiwade,[1] A. Oskarsson,[34] I. Otterlund,[34] M. Ouchida,[18] K. Ozawa,[8] R. Pak,[4] D. Pal,[56] A. P. T. Palounek,[32] V. Pantuev,[51] V. Papavassiliou,[39] J. Park,[49] W. J. Park,[27] S. F. Pate,[39] H. Pei,[22] J.-C. Peng,[20] H. Pereira,[12] V. Peresedov,[23] D. Yu. Peressounko,[28] C. Pinkenburg,[4] R. P. Pisani,[4] M. L. Purschke,[4] A. K. Purwar,[32,51] H. Qu,[17] J. Rak,[22,38] A. Rakotozafindrabe,[30] I. Ravinovich,[58] K. F. Read,[40,53] S. Rembeczki,[15] M. Reuter,[51] K. Reygers,[35] V. Riabov,[43] Y. Riabov,[43] G. Roche,[33] A. Romana,[30,*] M. Rosati,[22] S. S. E. Rosendahl,[34] P. Rosnet,[33] P. Rukoyatkin,[23] V. L. Rykov,[44] S. S. Ryu,[59] B. Sahlmueller,[35] N. Saito,[29,44,45] T. Sakaguchi,[4,8,57] S. Sakai,[55] H. Sakata,[18] V. Samsonov,[43] H. D. Sato,[29,44] S. Sato,[4,25,55] S. Sawada,[25] J. Seele,[9] R. Seidl,[20] V. Semenov,[19] R. Seto,[5] D. Sharma,[58] T. K. Shea,[4] I. Shein,[19] A. Shevel,[43,50] T.-A. Shibata,[44,54] K. Shigaki,[18] M. Shimomura,[55] T. Shohjoh,[55] K. Shoji,[29,44] A. Sickles,[51] C. L. Silva,[48] D. Silvermyr,[40] C. Silvestre,[12] K. S. Sim,[27] C. P. Singh,[2] V. Singh,[2] S. Skutnik,[22] M. Slunečka,[6,23] W. C. Smith,[1] A. Soldatov,[19] R. A. Soltz,[31] W. E. Sondheim,[32] S. P. Sorensen,[53] I. V. Sourikova,[4] F. Staley,[12] P. W. Stankus,[40] E. Stenlund,[34] M. Stepanov,[39] A. Ster,[26] S. P. Stoll,[4] T. Sugitate,[18] C. Suire,[41] J. P. Sullivan,[32] J. Sziklai,[26] T. Tabaru,[45] S. Takagi,[55] E. M. Takagui,[48] A. Taketani,[44,45] K. H. Tanaka,[25] Y. Tanaka,[37] K. Tanida,[44,45] M. J. Tannenbaum,[4] A. Taranenko,[50] P. Tarján,[13] T. L. Thomas,[38] M. Togawa,[29,44] A. Toia,[51] J. Tojo,[44] L. Tomášek,[21] H. Torii,[44] R. S. Towell,[1] V.-N. Tram,[30] I. Tserruya,[58] Y. Tsuchimoto,[18,44] S. K. Tuli,[2] H. Tydesjö,[34] N. Tyurin,[19] C. Vale,[22] H. Valle,[56] H. W. van Hecke,[32] J. Velkovska,[56] R. Vertesi,[13] A. A. Vinogradov,[28] M. Virius,[11] V. Vrba,[21] E. Vznuzdaev,[43] M. Wagner,[29,44] D. Walker,[51] X. R. Wang,[39] Y. Watanabe,[44,45] J. Wessels,[35] S. N. White,[4] N. Willis,[41] D. Winter,[10] C. L. Woody,[4] M. Wysocki,[9] W. Xie,[5,45] Y. L. Yamaguchi,[57] A. Yanovich,[19] Z. Yasin,[5] J. Ying,[17] S. Yokkaichi,[44,45] G. R. Young,[40] I. Younus,[38] I. E. Yushmanov,[28] W. A. Zajc,[10] O. Zaudtke,[35] C. Zhang,[10,40] S. Zhou,[7] J. Zimányi,[26,*] and L. Zolin[23]

(PHENIX Collaboration)

[1]*Abilene Christian University, Abilene, Texas 79699, USA*
[2]*Department of Physics, Banaras Hindu University, Varanasi 221005, India*
[3]*Collider-Accelerator Department, Brookhaven National Laboratory, Upton, New York 11973-5000, USA*
[4]*Brookhaven National Laboratory, Upton, New York 11973-5000, USA*
[5]*University of California-Riverside, Riverside, California 92521, USA*
[6]*Charles University, Ovocný trh 5, Praha 1, 116 36, Prague, Czech Republic*
[7]*China Institute of Atomic Energy (CIAE), Beijing, People's Republic of China*
[8]*Center for Nuclear Study, Graduate School of Science, University of Tokyo, 7-3-1 Hongo, Bunkyo, Tokyo 113-0033, Japan*
[9]*University of Colorado, Boulder, Colorado 80309, USA*
[10]*Columbia University, New York, New York 10027 and Nevis Laboratories, Irvington, New York 10533, USA*
[11]*Czech Technical University, Zikova 4, 166 36 Prague 6, Czech Republic*
[12]*Dapnia, CEA Saclay, F-91191, Gif-sur-Yvette, France*
[13]*Debrecen University, H-4010 Debrecen, Egyetem tér 1, Hungary*
[14]*ELTE, Eötvös Loránd University, H-1117 Budapest, Pázmány P. s. 1/A, Hungary*
[15]*Florida Institute of Technology, Melbourne, Florida 32901, USA*
[16]*Florida State University, Tallahassee, Florida 32306, USA*
[17]*Georgia State University, Atlanta, Georgia 30303, USA*
[18]*Hiroshima University, Kagamiyama, Higashi-Hiroshima 739-8526, Japan*
[19]*IHEP Protvino, State Research Center of Russian Federation, Institute for High Energy Physics, Protvino, RU-142281, Russia*
[20]*University of Illinois at Urbana-Champaign, Urbana, Illinois 61801, USA*
[21]*Institute of Physics, Academy of Sciences of the Czech Republic, Na Slovance 2, 182 21 Prague 8, Czech Republic*
[22]*Iowa State University, Ames, Iowa 50011, USA*
[23]*Joint Institute for Nuclear Research, RU-141980 Dubna, Moscow Region, Russia*
[24]*KAERI, Cyclotron Application Laboratory, Seoul, Korea*
[25]*KEK, High Energy Accelerator Research Organization, Tsukuba, Ibaraki 305-0801, Japan*
[26]*KFKI Research Institute for Particle and Nuclear Physics of the Hungarian Academy of Sciences (MTA KFKI RMKI), H-1525 Budapest 114, PO Box 49, Budapest, Hungary*
[27]*Korea University, Seoul, 136-701, Korea*
[28]*Russian Research Center "Kurchatov Institute," Moscow, Russia*
[29]*Kyoto University, Kyoto 606-8502, Japan*
[30]*Laboratoire Leprince-Ringuet, Ecole Polytechnique, CNRS-IN2P3, Route de Saclay, F-91128, Palaiseau, France*
[31]*Lawrence Livermore National Laboratory, Livermore, California 94550, USA*
[32]*Los Alamos National Laboratory, Los Alamos, New Mexico 87545, USA*
[33]*LPC, Université Blaise Pascal, CNRS-IN2P3, Clermont-Fd, 63177 Aubiere Cedex, France*
[34]*Department of Physics, Lund University, Box 118, SE-221 00 Lund, Sweden*
[35]*Institut für Kernphysik, University of Muenster, D-48149 Muenster, Germany*
[36]*Myongji University, Yongin, Kyonggido 449-728, Korea*
[37]*Nagasaki Institute of Applied Science, Nagasaki-shi, Nagasaki 851-0193, Japan*
[38]*University of New Mexico, Albuquerque, New Mexico 87131, USA*
[39]*New Mexico State University, Las Cruces, New Mexico 88003, USA*
[40]*Oak Ridge National Laboratory, Oak Ridge, Tennessee 37831, USA*
[41]*IPN-Orsay, Université Paris Sud, CNRS-IN2P3, BP1, F-91406, Orsay, France*
[42]*Peking University, Beijing, People's Republic of China*
[43]*PNPI, Petersburg Nuclear Physics Institute, Gatchina, Leningrad region, RU-188300, Russia*
[44]*RIKEN Nishina Center for Accelerator-Based Science, Wako, Saitama 351-0198, Japan*
[45]*RIKEN BNL Research Center, Brookhaven National Laboratory, Upton, New York 11973-5000, USA*
[46]*Physics Department, Rikkyo University, 3-34-1 Nishi-Ikebukuro, Toshima, Tokyo 171-8501, Japan*
[47]*Saint Petersburg State Polytechnic University, St. Petersburg, Russia*
[48]*Universidade de São Paulo, Instituto de Física, Caixa Postal 66318, São Paulo CEP05315-970, Brazil*
[49]*System Electronics Laboratory, Seoul National University, Seoul, Korea*
[50]*Chemistry Department, Stony Brook University, Stony Brook, SUNY, New York 11794-3400, USA*
[51]*Department of Physics and Astronomy, Stony Brook University, SUNY, Stony Brook, New York 11794, USA*
[52]*SUBATECH (Ecole des Mines de Nantes, CNRS-IN2P3, Université de Nantes) BP 20722-44307, Nantes, France*
[53]*University of Tennessee, Knoxville, TN 37996, USA*
[54]*Department of Physics, Tokyo Institute of Technology, Oh-okayama, Meguro, Tokyo 152-8551, Japan*
[55]*Institute of Physics, University of Tsukuba, Tsukuba, Ibaraki 305, Japan*
[56]*Vanderbilt University, Nashville, Tennessee 37235, USA*
[57]*Waseda University, Advanced Research Institute for Science and Engineering, 17 Kikui-cho, Shinjuku-ku, Tokyo 162-0044, Japan*

[58] *Weizmann Institute, Rehovot 76100, Israel*
[59] *Yonsei University, IPAP, Seoul 120-749, Korea*
(Received 1 December 2009; published 29 March 2010)

PHENIX has measured the e^+e^- pair continuum in $\sqrt{s_{NN}} = 200$ GeV Au+Au and $p+p$ collisions over a wide range of mass and transverse momenta. The e^+e^- yield is compared to the expectations from hadronic sources, based on PHENIX measurements. In the intermediate-mass region, between the masses of the ϕ and the J/ψ meson, the yield is consistent with expectations from correlated $c\bar{c}$ production, although other mechanisms are not ruled out. In the low-mass region, below the ϕ, the $p+p$ inclusive mass spectrum is well described by known contributions from light meson decays. In contrast, the Au+Au minimum bias inclusive mass spectrum in this region shows an enhancement by a factor of $4.7 \pm 0.4^{\text{stat}} \pm 1.5^{\text{syst}} \pm 0.9^{\text{model}}$. At low mass ($m_{ee} < 0.3$ GeV/c^2) and high p_T ($1 < p_T < 5$ GeV/c) an enhanced e^+e^- pair yield is observed that is consistent with production of virtual direct photons. This excess is used to infer the yield of real direct photons. In central Au+Au collisions, the excess of the direct photon yield over the $p+p$ is exponential in p_T, with inverse slope $T = 221 \pm 19^{\text{stat}} \pm 19^{\text{syst}}$ MeV. Hydrodynamical models with initial temperatures ranging from $T_{\text{init}} \simeq 300$–$600$ MeV at times of 0.6–0.15 fm/c after the collision are in qualitative agreement with the direct photon data in Au+Au. For low $p_T < 1$ GeV/c the low-mass region shows a further significant enhancement that increases with centrality and has an inverse slope of $T \simeq 100$ MeV. Theoretical models underpredict the low-mass, low-p_T enhancement.

DOI: 10.1103/PhysRevC.81.034911 PACS number(s): 25.75.Dw

I. INTRODUCTION

Experimental results from the Relativistic Heavy Ion Collider (RHIC) have established that in Au+Au collisions at $\sqrt{s_{NN}} = 200$ GeV matter is created with very high energy density [1], as indicated by the large energy produced transverse to the beam direction [2], as well as by the large energy loss of light [3,4] and heavy quarks [5,6], and is thermalized rapidly, as indicated by the large elliptic flow of these partons [6–9]. Such a high-density thermalized medium is expected to emit thermal radiation [10] in the form of direct photons and dileptons.

Electron-positron pairs, or dileptons in general, are excellent tools for studying collisions of heavy ions at ultrarelativistic energies. Since they are not affected by the strong interaction, and therefore can escape from the dense medium without final-state interaction, dilepton spectra can probe the whole time evolution and dynamics of the collision. Dileptons can also be used to study the properties of low-mass vector mesons ρ, ω, and ϕ in the medium, since their lifetime is shorter or similar (ϕ) to that of the medium. Their spectral properties inside the dense medium can be directly measured through their dilepton decay channels, and thereby one can study the effect of chiral symmetry restoration on these mesons. Furthermore, production of photons can be measured through their conversion to dileptons.

As schematically shown in Fig. 1, the dilepton spectra can be classified into the high-mass region (HMR; $m > 3.2$ GeV/c^2) from J/ψ mass and above, the low-mass region (LMR; $m < 1.2$ GeV/c^2) from the ϕ mass and below, which is further subdivided in LMR I and LMR II as described below, and the intermediate mass region (IMR; $1.2 < m < 2.9$ GeV/c^2) between them.

In the HMR hard scattering on partons in colliding nuclei produces dileptons through the Drell-Yan process ($\bar{q}q \rightarrow l^+l^-$) and correlated semileptonic decays of heavy quark pairs ($b\bar{b} \rightarrow l^+l^-, c\bar{c} \rightarrow l^+l^-$). Dileptons from these hard processes are expected to dominate in the HMR since their mass spectra are harder than that from other possible sources. Thus dileptons in the HMR probe the initial stage of the collision [11]. Charmonia (J/ψ, ψ') and Upsilons are in this mass region and deconfinement [12] and recombination [13,14] effects can be studied from their yields. Little contribution from thermal radiation is expected in the HMR at RHIC energies [11].

In the IMR theoretical models predict that dileptons from the thermalized deconfined phase, the quark-gluon plasma (QGP), are the dominant source of dileptons [15–17]. The measurement of thermal dileptons from QGP can be used to determine the initial temperature of the matter. Here a competing source of dileptons is the semileptonic decay of c and $\bar{c}$, correlated through flavor conservation. The continuum yield in this mass region is sensitive to the energy loss of charm quarks in the medium.

In the LMR dilepton production is expected to be dominated by in-medium decay of ρ mesons in the hadronic gas phase [18–20]. The ρ has a strong coupling to the $\pi\pi$ channel, and its lifetime (1.3 fm/c) is much shorter than the expected lifetime of the hadronic gas. The shape and the yield of the mass spectrum can test predicted in-medium modifications of the properties (the spectral function) of ρ mesons due to chiral symmetry restoration [21]. Dileptons can also arise from other hadronic sources. These dilepton sources compete with a large contribution of e^+e^- pairs from Dalitz decays of pseudoscalar mesons (π^0, η, η') and decays of vector mesons (ρ, ω, ϕ).

In the LMR I (marked with I in Fig. 1) is the quasireal virtual photon region, where the p_T of the dilepton is much greater than its mass ($p_T \gg m_{ll}$). Any source of real photons must also emit virtual photons which convert to low-mass e^+e^- pairs. These low-mass pairs are produced by a higher-order QED correction to the real photon emission process, and their yield is related to that of real photons. Thus e^+e^- pairs in this region provide an alternative method for measuring direct photons. The measurement of the direct photon yield using

*Deceased.
†PHENIX Spokesperson: jacak@skipper.physics.sunysb.edu

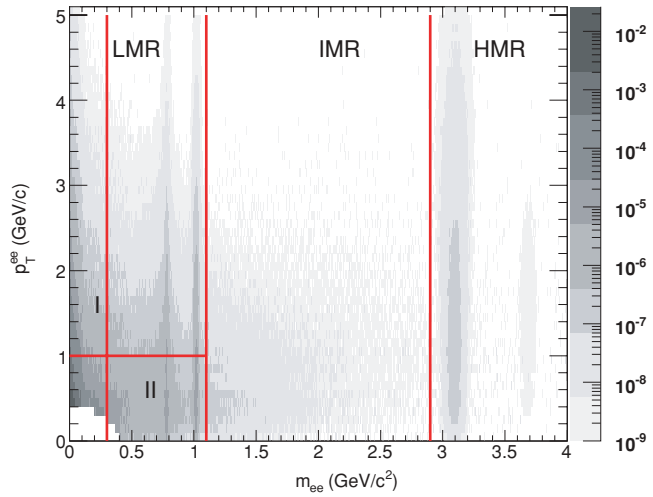

FIG. 1. (Color online) Dilepton spectrum as a function of mass and transverse momentum from a simulation of hadron decays. The high-mass region (HMR; $m_{ee} > 3.2$ GeV/c^2) goes from J/ψ mass and above, the low-mass region (LMR; $m_{ee} < 1.2$ GeV/c^2) from the ϕ mass and below, and the intermediate mass region (IMR; $1.2 < m_{ee} < 2.9$ GeV/c^2) between them. In the LMR at low-p_T (II), dilepton production is expected to be dominated by the hadronic gas phase. Part of the LMR, where $p_T \gg m_{ll}$, specifically $m_{ee} < 0.3$ GeV/c^2 and $p_T > 1$ GeV/c (I), is the quasireal virtual photon region. The z axis shows the dilepton yield from the hadron decays according to the color scheme plotted on the right.

low-mass lepton pairs was first used at the CERN ISR [22]. UA1 observed that the low-mass dimuon cross section was consistent with the "internal conversion" of direct photons [23].

The discovery of a large enhancement of the dilepton yield in the LMR in ion-ion collisions by HELIOS/3 [24] and CERES [25] at the CERN Super Proton Synchrotron (SPS) has triggered a broad theoretical investigation of modifications of properties of hadrons in a dense medium and of how these modifications relate to chiral symmetry restoration [21,26,27]. These studies advanced with the availability of more precise data from NA60 and CERES [28–30] and HADES [31]. Most theoretical studies suggest that in-medium modifications of the ρ meson, with its short lifetime and its strong coupling to the $\pi\pi$ channel, are primarily responsible for the enhancement.

In the LMR II (marked with II in Fig. 1) the CERES data show that the enhancement increases significantly faster than linearly with charged particle density and is concentrated at very low pair p_T [29]. This behavior is consistent with the interpretation that the excess is due to annihilation processes. NA60 recently confirmed the excess of dileptons in the LMR in In+In collisions at 158A GeV with a high-statistics dimuon measurement [28]. NA60 also observed that the inverse slope parameter $T_{\rm eff}$ of the pair-p_T spectra rises with dimuon mass in the LMR [32].

An enhanced yield was also observed in the IMR by HELIOS/3 [24,33], NA38/50 [34,35], and NA60 [28,32]. The NA60 data suggest that the enhancement cannot be attributed to decays of D mesons but may result from prompt production, as expected for thermal radiation [36]. Furthermore, NA60 measures the inverse slope parameter of pair-p_T spectra in the IMR around 190 MeV, independent of mass and significantly lower than those found at masses below 1 GeV/c^2 [32,36].

The PHENIX experiment at RHIC has measured the dilepton continuum in a new energy regime, $\sqrt{s_{NN}} = 200$ GeV, for $p+p$ and Au+Au collisions. In this article we present results from Au+Au collisions taken in 2004 and $p+p$ collisions taken in 2005. We show the results in the LMR and in the IMR as well as the result of direct photon measurement from the analysis of quasireal virtual photons. The main physics results in the LMR and IMR in Au+Au and $p+p$ have been reported in Refs. [37] and [38], respectively, and the results of the virtual photon analysis have been reported in Ref. [39]. New results on the centrality and p_T dependence of the e^+e^- pairs in the LMR are presented in this article.

This article is organized as follows. Section II describes the PHENIX detector system related to the analysis. Section III presents the analysis details including the systematic uncertainties. Section IV describes the methods used to calculate the pair yield expected from hadronic decays. Section V shows the e^+e^- results as a function of m_{ee} and p_T, which are then discussed in Sec. VI and compared to available theoretical predictions. Finally Sec. VII provides a conclusion.

II. PHENIX DETECTOR

A detailed description of the complete PHENIX detector system can be found elsewhere [40–46]. Here we describe the parts of the detector system that are used in this analysis, namely two global detectors and two central arm spectrometers. The global detectors are the beam-beam counters (BBC) and the zero-degree calorimeters (ZDC). Each central arm covers the pseudorapidity range $|\eta| < 0.35$ and an azimuthal angle of $\pi/2$ and includes a drift chamber (DC) and multiwire proportional pad chambers (PC) for the charged particle tracking, a ring-imaging Čerenkov counter (RICH) for electron identification, and an electromagnetic calorimeter (EMCal) for energy measurement and further electron identification. Figure 2 shows a beam view of the PHENIX detector.

A. Global detectors

The BBC and the ZDC measure the start time and the collision vertex position z vertex along the beam axis and are used to determine the centrality of the collision [46]. They also provide first level trigger information.

The BBC consists of two sets of 64 Čerenkov counter modules, located ± 1.44 m from the nominal interaction point along the beam line and measure the number of charged particles in the pseudorapidity region $3.1 < |\eta| < 3.9$. They provide the start time of the collision with a resolution of 20 ps, which gives the z-vertex position with a resolution of $\sim$2 cm in $p+p$ collisions. For Au+Au central collisions we achieve a resolution of $\sim$0.6 cm.

The ZDC consists of two hadronic calorimeters, located $\sim$18 m from the interaction point, that measure the energy emitted within $\sim$2 mrad of the beam direction by neutrons produced either by Coulomb dissociation of the beam particle

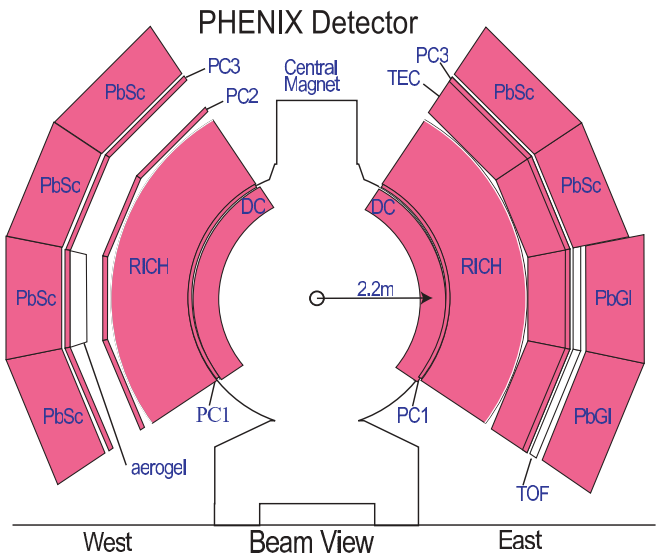

FIG. 2. (Color online) Beam view (at $z = 0$) of the PHENIX central arm detector in Run-4 Au+Au and Run-5 p+p. The detectors used in the present analysis are the drift chamber (DC) and the multiwire proportional pad chamber (PC) for charged particle tracking, the ring-imaging Čerenkov counter (RICH) for electron identification, and the electromagnetic calorimeter [lead-scintillator (PbSc) and lead-glass (PbGl)] for energy measurement.

or by evaporation from beam spectators. The energy resolution of the ZDC is $\delta E/E \sim 218\%/\sqrt{E\ (\mathrm{GeV})}$ [41].

The centrality of Au+Au collisions is determined by the correlation between the BBC charge sum and the ZDC total energy [47].

B. Central magnet

The central magnet (CM) is an axial field magnet energized by two pairs of concentric coils, roughly in a Helmholtz configuration, which can be run separately, together, or in opposition so the momentum and the charge of a particle can be determined by its bending curvature [42]. In the mode in which both coils are running in the same direction, the single-particle momentum resolution is better than 1% between 0.2 and 1 GeV/c. During the Au+Au measurement in Run-4 and the p+p measurement in Run-5, the field component parallel to the beam axis had an approximately Gaussian dependence on the radial distance from the beam axis, dropping from 0.9 T at the center to 0.096 T (0.048 T) at the inner (outer) radius of the DCs. The total field integral is $\int B \times dl = 1.15$ Tm.

C. Tracking detectors

The drift chambers (DCs) and the pad chambers (PCs) [43] in the central arms measure charged particle trajectories in the azimuthal direction to determine the transverse momentum (p_T) of each particle. The DC provides the most precise measurement of particle trajectories in the plane perpendicular to the collision axis. The first layer of PC provides the most precise measurement of the track space point along the collision axis. Additional layers principally supply pattern recognition support.

The DCs are located in the radial region $2.02 < r < 2.46$ m. Each DC volume consists of 20 sectors, each of which covers 4.5° in azimuth and $|\eta| < 0.35$. Each sector has six types of wire modules stacked radially: X1, U1, V1, X2, U2, and V2. Each module is further divided into four drift cells in the ϕ direction. A plane of sense wires is at the center of each drift cell, with 2 to 2.5 cm of drift space on either side. The X wires run parallel to the beam axis and measure the particle trajectory in the r-ϕ plane. The U and V wires have a stereo angle of about 6.0° relative to the X wires in order to measure the z coordinate of the track. Each X- and U, V-stereo cell contains 12 and 4 sense wires, respectively. The single X wire position resolution is ∼150 μm. The intrinsic tracking efficiency of the X modules is greater than 99%.

The pad chambers (PC) are multiwire proportional chambers that form three separate layers. They determine space points along the straight-line particle trajectories outside the magnetic field. The first PC layer (PC1) is located between the DC and the RICH, the second layer (PC2) is placed behind RICH (west arm only), and the third layer (PC3) is located in front of the EMCal. PC1 and the DC, along with the z-vertex position measured by the BBC, are used in the global track reconstruction to determine the polar angle of each charged track. The position resolution is ±1.7 mm for PC1 along the wire (z direction).

Helium bags were installed between the beam pipe and the DCs to reduce the conversion material prior to the first tracking layer to ∼0.4% of a radiation length. The material budget is known with an uncertainty of ∼5%.

D. Ring-imaging Čerenkov counter

The RICH is a threshold gas Čerenkov detector and is the primary detector to identify electrons in PHENIX [44]. It is located in the radial region $2.5 < r < 4.1$ m, just outside PC1. Each arm contains spherical mirror panels (0.53% of a radiation length) which focus Čerenkov light onto two arrays of $80(\phi) \times 16(z) = 1280$ PMTs. The PMTs are located outside the acceptance, on either side of the RICH entrance window, and are shielded to allow operation in a magnetic field up to 100 g. The Čerenkov radiator gas, CO_2 at atmospheric pressure, has $n = 1.000410$ ($\gamma = 35$) that corresponds to a momentum threshold of 20 MeV/c for an electron and 4.65 GeV/c for a pion.

The average number of hit PMTs per electron track is about 5, and the average number of photo-electrons detected is about 10. Simulation studies show that pion rejection by the RICH alone, for isolated tracks, is limited by the production rate of "collinear" delta electrons to one part in 10^4. However in high-multiplicity collisions pion tracks may be mistaken for electrons via overlap of their trajectory with a true electron's ring. This effect worsens the RICH-alone pion rejection to roughly one part in 10^3 for central Au+Au collisions and requires additional cuts in the offline analysis as described below.

E. Electromagnetic calorimeter

The EMCal [45] provides a measurement of the energies and the spatial positions of photons and electrons. Each arm consists of four rectangular sectors in ϕ: the two bottom sectors of the east arm are lead-glass (PbGl) calorimeters, whereas the remaining sectors are lead-scintillator (PbSc) calorimeters. The radial distance from the z axis is 510 cm for the PbSc and 550 cm for the PbGl.

The PbSc is a Shashlik-type sampling calorimeter made of alternating tiles of lead and scintillator. It consists of $10.5 \times 10.5 \times 37$ cm^3 ($18.2X_0$) modules, constructed of alternating layers of 1.5-mm-thick lead, reflecting paper, and 4-mm-thick polystyrene-based scintillator. Each module is divided into four equal towers, from which the light is collected separately by scintillating fibers. Each PbSc sector consists of $36(\phi) \times 72(z) = 2592$ towers. The nominal energy resolution is $\delta E/E \sim 4.5\% \oplus 8.3\%/\sqrt{E\ (\mathrm{GeV})}$.

The PbGl is a Čerenkov counter that measures the light emitted by the particles in an electromagnetic shower and collected by one PMT at the back end. Each PbGl sector consists of 4608 $4.0 \times 4.0 \times 40.0$ cm^3 ($16X_0$) modules made of lead-glass crystals. The PbGl has a nominal energy resolution of $\delta E/E \sim 4.3\% \oplus 7.7\%/\sqrt{E\ (\mathrm{GeV})}$.

III. ANALYSIS

In this section we present all steps of the data analysis. We start by introducing the data set, the event selection for $p+p$ and Au+Au, and the centrality definition for Au+Au collisions (subsection III A). We present the single-electron analysis, including track reconstruction (subsection III B) and electron identification (subsection III C). We present the details of the pair analysis (subsection III D), including pair cuts and photon rejection (III D1) and combinatorial and correlated (subsection III D2) background subtraction. An alternative method to subtract combinatorial and correlated background together is described in subsection III D. Subsection III E presents the final raw mass spectrum. In subsection III F we present the mass spectrum obtained from the analysis of runs with increased conversion material, a technique employed to estimate the systematic uncertainty on the background subtraction. Next we describe the efficiency (subsection III G) and acceptance (subsection III H) corrections, trigger efficiency (subsection III I) (for $p+p$ collisions), and occupancy correction (for Au+Au collisions) (subsection III J). Finally we describe the calculation of the associated systematic uncertainties involved in the analysis (subsection III K).

A. Data sets and event selection

The data for $p+p$ collisions at $\sqrt{s} = 200$ GeV were collected during the polarized $p+p$ run in 2005. The proton beams had approximately 50% longitudinal polarization with alternating spin orientations in successive bunches. The polarization of the protons has negligible effect on the e^+e^- cross section. For this analysis two data sets were used: a reference sample of events selected with a minimum bias interaction trigger (Min.Bias) and a data set selected with a single-electron trigger (ERT: EMCal and RICH trigger). The Min.Bias trigger for $p+p$ requires at least one hit in both the north and south BBC detectors in coincidence with the beam bunch crossing and a z-vertex position (determined online by the BBCs) within 38 cm:

$$\text{Min.Bias} \equiv (\text{BBCN} \geqslant 1) \times (\text{BBCS} \geqslant 1) \times (|z| < 38\ \text{cm}). \tag{1}$$

The Min.Bias trigger cross section is measured to be $\sigma_{\text{BBC}} = 23.0 \pm 2.2$ mb or $54.5 \pm 5\%$ of the total inelastic $p+p$ cross section at this center-of-mass energy $\sigma_{\text{inel}}^{p+p} = 42 \pm 3$ mb [48]. From the ratio of data collected with and without requiring the BBC trigger we determine the fraction of events with particles in the central arm acceptance to be $\epsilon_{\text{bias}} = 79 \pm 2\%$, momentum and process independent [49]. Therefore, in the $p+p$ data the yield is divided by 0.79/0.545 to account for the fraction of tracks (0.79) and inelastic $p+p$ collisions (0.545) missed by the Min.Bias trigger.

The ERT trigger requires a minimum energy deposit of 0.4 GeV in a tile of 2×2 EMCal towers matched to a hit in the RICH, in coincidence with the Min.Bias trigger. In the active area the ERT trigger has a very high efficiency for electrons; it reaches approximately 50% at ~ 0.5 GeV/c and saturates at $\sim$1 GeV/c close to 100% (for the EMCal) and close to 90% (for the RICH).

After applying a z-vertex cut $|z| < 25$ cm, and discarding any run with unusual beam or detector conditions, the total integrated luminosities were 65.6 nb^{-1} and 2.49 pb^{-1} for the Min. Bias and ERT data sets, respectively.

The data for Au+Au collisions at $\sqrt{s_{NN}} = 200$ GeV were collected during the run in 2004. Collisions were triggered using BBCs. The Min.Bias trigger requires at least two hits in each of the BBCs and $|z| < 38$ cm:

$$\text{Min.Bias} \equiv (\text{BBCN} \geqslant 2) \times (\text{BBCS} \geqslant 2) \times (|z| < 38\ \text{cm}). \tag{2}$$

The offline Min.Bias trigger also requires one hit in one of the ZDCs. The same z-vertex cut $|z| < 25$ cm as in the $p+p$ data is applied offline. This corresponds to $92^{+2.5}_{-3.0}\%$ of the Au+Au inelastic cross section.

The centrality is determined for each Au+Au collision by the correlation in the measurement of the BBC charge and ZDC energy [47]. Using simulations based on a Glauber model calculation [2] the average number of participants N_{part} and the average number of binary collisions N_{coll} associated with each centrality bin are determined. Table I summarizes the average N_{part} and N_{coll} and the corresponding systematic uncertainties in each centrality class used in the analysis.

We analyzed a sample of 8×10^8 minimum bias events, divided into five centrality classes (0–10%, 10–20%, 20–40%, 40–60%, and 60–92%) for which the number of events is summarized in Table I.

B. Track reconstruction

The PHENIX tracking system reconstructs charged particles with momentum above 0.2 GeV/c with a momentum

TABLE I. $N_{\rm part}$, $N_{\rm coll}$, for Au+Au collisions at $\sqrt{s_{NN}} = 200$ GeV with the corresponding uncertainties derived from a Glauber calculation [2] and the number of events and pairs for each centrality class. Note that the uncertainties are correlated [50].

Centrality class	$\langle N_{\rm part}\rangle$(syst)	$\langle N_{\rm coll}\rangle$(syst)	$N_{\rm events}$	Signal pairs
0–10%	325.2 (3.3)	955.4 (93.6)	8.6×10^7	9.2×10^4
10–20%	234.6 (4.7)	602.6 (59.3)	8.6×10^7	6.6×10^4
20–40%	140.4 (4.9)	296.8 (31.1)	1.7×10^8	8.1×10^4
40–60%	59.95 (3.6)	90.70 (11.8)	1.7×10^8	3.3×10^4
60–92%	14.50 (2.5)	14.50 (4.00)	2.9×10^8	1.1×10^4
0–92%	109.1 (4.1)	257.8 (25.4)	8.1×10^8	28.3×10^4
$p+p$ (Min.Bias)	2	1	1.5×10^9	1.4×10^4
$p+p$ (ERT)	2	1	2.7×10^8	22.8×10^4

resolution of $\sigma_{p_T}/p_T = 0.7\% \oplus 1\% \times p_T$ for p_T in GeV/c. A track is reconstructed by two sets of at least four hits in the X1 and X2 plane separated by 20 cm in radial direction, i.e., in the main bend plane of the central magnet, using a Hough transform performed over all possible hit combinations. The UV1 and UV2 wires provide up to six measurements in the z direction, which are associated with the three-dimensional space point provided by PC1. After the pattern recognition and track reconstruction by the Hough transform technique, the initial momentum vector of the track at the z vertex is calculated. Each reconstructed track is then associated with hit information from the outer detectors (PC2, PC3, RICH, and EMCal).

The transverse momentum (p_T) is determined by measuring the angle α between the reconstructed particle trajectory and a line that connects the z-vertex point to the particle trajectory at a reference radius $R = 220$ cm. The angle α is approximately proportional to charge/p_T. Note that this procedure assumes tracks originate from the vertex. As a result, tracks that originate off vertex are reconstructed with an incorrect momentum. Conversion pairs are reconstructed with invariant mass $m_{ee} > 0$ and contaminate the spectrum up to $m_{ee} \sim 0.3$ GeV/c^2 (see subsection III D1).

Because charged particles are deflected in the azimuthal direction by the magnetic field, the single-track acceptance depends on the momentum and charge of the particle and on the radial location of the detector component (DC and RICH). The acceptance for a track with charge q, transverse momentum p_T, and azimuthal emission angle ϕ can be described by the logical AND of these conditions:

$$\begin{aligned} \phi_{\rm min} &\leqslant \phi + q\frac{k_{\rm DC}}{p_T} \leqslant \phi_{\rm max} \\ \phi_{\rm min} &\leqslant \phi + q\frac{k_{\rm RICH}}{p_T} \leqslant \phi_{\rm max}, \end{aligned} \tag{3}$$

where $k_{\rm DC}$ and $k_{\rm RICH}$ represent the effective azimuthal bend to DC and RICH ($k_{\rm DC} = 0.206$ rad GeV/c and $k_{\rm RICH} = 0.309$ rad GeV/c). One arm covers the region from $\phi_{\rm min} = \frac{-3}{16}\pi$ to $\phi_{\rm max} = \frac{5}{16}\pi$, the other arm from $\phi_{\rm min} = \frac{11}{16}\pi$ to $\phi_{\rm max} = \frac{19}{16}\pi$.

Results in Sec. V will show the dilepton invariant mass spectrum "in the PHENIX acceptance," where the data will be compared to the expectations filtered according to this simple parametrization of the acceptance.

C. Electron identification

Electrons in the range $0.2 < p_T < 20$ GeV/c are identified by hits in the RICH and by matching the momentum with the energy measured in the EMCal [6]. Specifically, we consider the following variables for electron identification (eID), as summarized in Table II.

Track quality: A bit pattern representing the reconstruction quality of the track. If the track is reconstructed by both of the X1 and X2 sections of the DC and is uniquely associated with hits in U or V stereo wires, the value of `quality` is 63 (in case a unique PC1 hit is found too) or 31 (in case the PC1 hit is found but ambiguous). If there are no UV hits found, but a PC1 hit is, `quality` is 51.

EMCal match ($\sigma_{\Delta\phi}$): Displacement in ϕ between the position of the associated EMCal cluster and the projection of the track onto the EMCal. The quantity is measured in units of momentum-dependent resolution. For example, $\Delta\phi < 2$ means that the position of the associated EMCal cluster in ϕ is within 2σ of the projected track position. The particle hit position of an EMCal cluster is particle-species dependent due to different shower shapes. Here the parameterization has been optimized for electrons.

TABLE II. Electron ID cuts used in the Au+Au and $p+p$ analyses.

eID cuts	Au+Au	$p+p$
Track quality =	63 || 31 || 51	63 || 31 || 51
$\sqrt{\sigma^2_{\Delta\phi} + \sigma^2_{\Delta z}}$ <	3.0	5.0
n0 $\geqslant$	2	1
chi2/npe0 <	10.0	15.0
RICH match <	5.0	10
dep >	−2.0	–
$\frac{E}{p}$ >	–	0.5

EMCal match ($\sigma_{\Delta z}$): Analogous to the previous variable for the z coordinate.

n0: Number of hit RICH PMTs in an annular region with an inner radius of 3.4 cm and outer radius of 8.4 cm around the track projection on the RICH. The expected radius of a Čerenkov ring emitted by an electron is 5.9 cm.

χ^2/npe0: A χ^2-like shape variable of the RICH ring associated with the track divided by the number of photoelectrons measured in a given ring (npe0).

RICH match: The displacement of the RICH ring center from the projected track position. Units are cm.

***E*/*p* or dep:** A variable quantifying energy-momentum matching. This variable is calculated as dep $= (E/p - 1)/\sigma_{E/p}$, where E is the energy measured by EMCal, p is the momentum of the track, and $\sigma_{E/p}$ is the standard deviation of the Gaussian-like E/p distribution calculated for electrons. $\sigma_{E/p}$ depends on the momentum of the electron.

Figure 3 shows[1] the E/p distribution for all charged tracks and for electron candidates, i.e., tracks which fulfill all the RICH eID cuts except the E/p or dep. While the distribution of all charged tracks shows no clear electron peak, requiring the eID cuts greatly improves the signal-to-background ratio. However, there still remains some background underneath the peak even below $p_T < 4.9$ GeV/c, the Čerenkov threshold for pions. This background, due to random coincidences between hadron tracks and hits in the RICH, is estimated by swapping the north and south sides of the RICH in software and reconstructing the track matching to the RICH once again.

[1]Data tables for this and other data plots are available at https://www.phenix.bnl.gov/WWW/p/info/ppg/088/datatables.

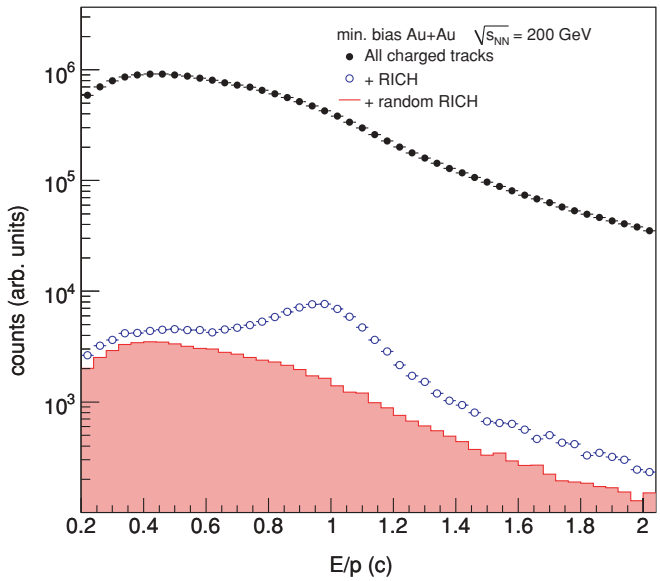

FIG. 3. (Color online) E/p distribution in minimum bias Au+Au for all charged tracks and for tracks after applying all the RICH cuts in Table II except the E/p or dep. The contribution from randomly associated hadrons is shown by the filled histogram.

This contamination ranges from 2% in $p+p$ to 30% in the most central Au+Au collisions. It is ∼24% for Min.Bias Au+Au collisions. This pion contamination in Au+Au contributes to the large combinatorial background (see subsection III D2).

D. Backgrounds

The source of any particular electron or positron in an event is unknown; therefore, all electrons and positrons are combined into a foreground of pairs, like-sign N_{++}, N_{--}, and unlike-sign N_{+-}. This results in a large combinatorial background that must be removed. In the following we will use the notation for the foreground $N_{\pm\pm} = N_{++} + N_{--}$ and for the background $B_{\pm\pm} = B_{++} + B_{--}$. The analysis steps to achieve this are outlined here and presented in detail in the subsections below. We can distinguish our background sources in two types:

Type I background (III D1) consists of two classes of fake combinations that can be identified on a pair-by-pair basis:

(i) Overlapping pairs are fake electron pairs that arise from overlapping hits in the detectors, mostly in the RICH.
(ii) Photon conversions are fully reconstructed pairs originating from photon conversions in the detector material are removed by a cut on the orientation of the pairs in the magnetic field.

Type II background (III D2) consists of all those pairs that cannot be identified on a pair-by-pair basis and are therefore removed statistically:

(i) Combinatorial background B^{comb} arises from all the combinations where the origin of the two electrons is totally uncorrelated.
(ii) Correlated background B^{corr} occurs if there are two e^+e^- pairs in the final state of a meson or when two hadrons, either within the same jet or in back-to-back jets, decay into electron pairs.

Since accurate background subtraction is essential for this analysis, we have developed two independent methods to subtract the type II background. In the first method we calculate the shapes of combinatorial and correlated background with event mixing or simulations and use the yield of the like-sign spectra for the normalization. In the second method (subsection III D3) we use the measured like-sign distributions, corrected for the acceptance difference, without making any assumption about the mass dependence nor about the decomposition of the background into correlated and uncorrelated component.

1. *Type I background*

a. Overlapping pairs. Fake electron pairs can be created if two particles are in close proximity in any of the detectors. These correlations within an event are particularly noticeable when two tracks share the same RICH ring. This issue can be illustrated with a simplified model of the RICH based on spherical mirror optics. In this case, tracks that are parallel to each other while passing through the RICH radiator, i.e., after they have been bent in the magnetic field, share the same search

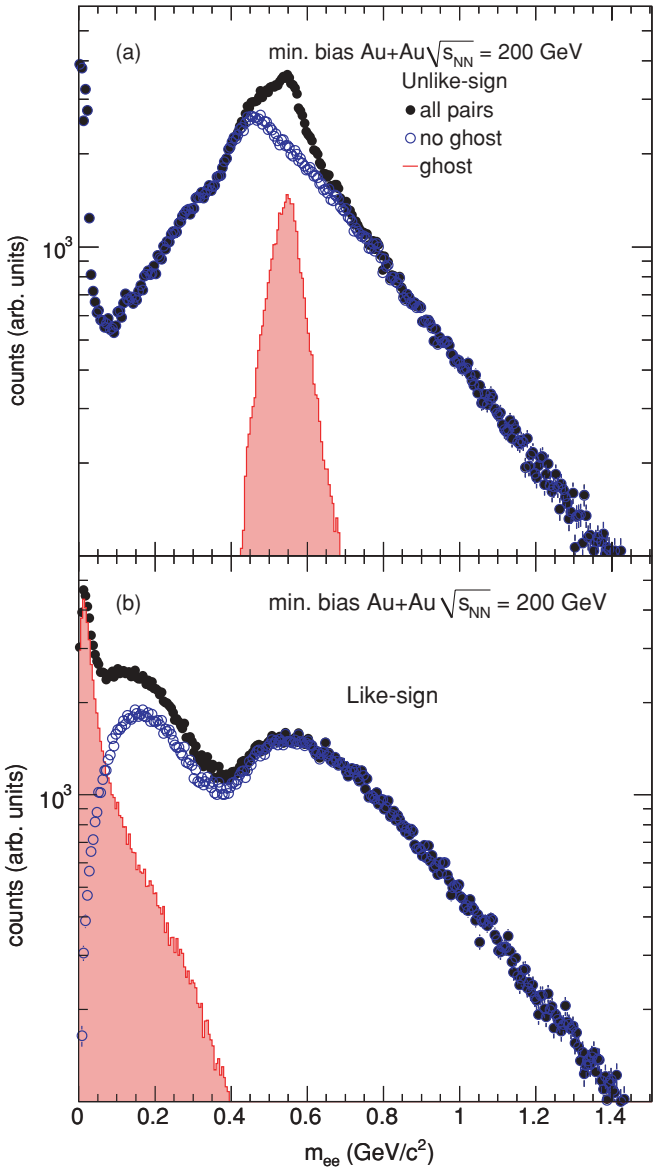

FIG. 4. (Color online) Invariant mass distribution for all like- and unlike-sign pairs. Overlapping pairs are shown separately. Also shown are the distributions after the overlapping pairs are removed.

region for Čerenkov light in the RICH PMT plane. Therefore an overlapping pair is created whenever a track after the field is parallel to a true electron. These overlapping pairs typically have a small opening angle and are therefore reconstructed with small invariant mass. Because like-sign pairs are bent in the same direction, in contrast to unlike-sign pairs that are bent in opposite directions, like-sign overlapping pairs have smaller mass than unlike-sign overlapping pairs. Figure 4 shows the invariant mass distribution for all like- and unlike-sign pairs, the distributions for overlapping pairs, and the distributions after removing overlapping pairs.

Overlapping pairs are eliminated by applying a cut on the physical proximity of every pair projected to every detector. The cut value on every detector is determined by the corresponding double hit resolution. In the RICH the cut is applied at 36 cm, which is roughly twice the predicted maximum diameter (∼16.8 cm) of a RICH ring. In the pad chambers the cut is applied at $\Delta z \leqslant 0.5$ cm and $\Delta\phi \leqslant 20$ mrad. In the EMCal the cut is applied to a 3×3 tower region around the hit. These cuts remove a fraction of real pairs that varies from 4% in the most central to 2% in the most peripheral collisions, estimated using mixed events. These cuts remove 10% more real like-sign than unlike-sign pairs. The ratio of like- to unlike-sign pairs lost was determined with an uncertainty of 50% by varying the cut values chosen. While the efficiency of the pair cut depends on the centrality, the ratio of like- to unlike-sign pairs lost was found to be independent of centrality.

Because these overlapping pairs are rare, whenever we encounter one, we remove the entire event. This results in a loss of ∼0.08% of all events. In mixed events the same cuts are applied and whenever an event is discarded due a pair cut, another event is generated with the same electron multiplicity and in the same centrality, z vertex, and reaction plane class.

b. Photon conversions. Since the tracking algorithm assumes that all tracks originate from the collision vertex, pairs from photons that convert off-vertex are reconstructed with an artificial opening angle, which leads to an invariant mass that increases with the radius at which the conversion occurs.

Conversion pairs have no intrinsic opening angle (i.e., their opening angle is exactly zero at the point of creation); they are bent only in the azimuthal direction by the magnetic field, which is parallel to the beam axis $\vec{z}$. We can define unit vectors $\hat{u}$ in the direction of the pair momentum and $\hat{v}$ perpendicular to the plane defined by the pair

$$\hat{u} = \frac{\vec{p}_+ + \vec{p}_-}{|\vec{p}_+ + \vec{p}_-|} \tag{4}$$

$$\hat{v} = \hat{p}_+ \times \hat{p}_-, \tag{5}$$

where $\hat{p}_\pm = \vec{p}_\pm/|\vec{p}_\pm|$ is the three-momentum vector of the $e_\pm$. We can define the orientation of the actual opening angle as

$$\hat{w} = \hat{u} \times \hat{v}. \tag{6}$$

We can also define the expected orientation of the opening angle for conversion pairs

$$\hat{w}_c = \hat{u} \times \hat{z}. \tag{7}$$

Finally, we can define ϕ_V as the angle between these two vectors

$$\cos\phi_V = \hat{w} \cdot \hat{w}_c. \tag{8}$$

For pairs originating from photon conversions ϕ_V is zero. (By consistently ordering positive and negative tracks within the pair we avoid $\phi_V = \pi$ as a solution for photon conversions.) In contrast, e^+e^- pairs from hadron decays, as well as combinatorial pairs, have no preferred orientation. Figure 5 presents a comparison of the ϕ_V angle distributions of real data and Monte Carlo simulated data in a mass bin, $10 < m_{ee} < 30$ MeV/c^2, dominated by photon conversion in the beam pipe. In the simulations we can distinguish which e^+e^- pairs originate from a π^0 Dalitz decay (dotted-dashed line) and which originate from photon conversion (dotted line).

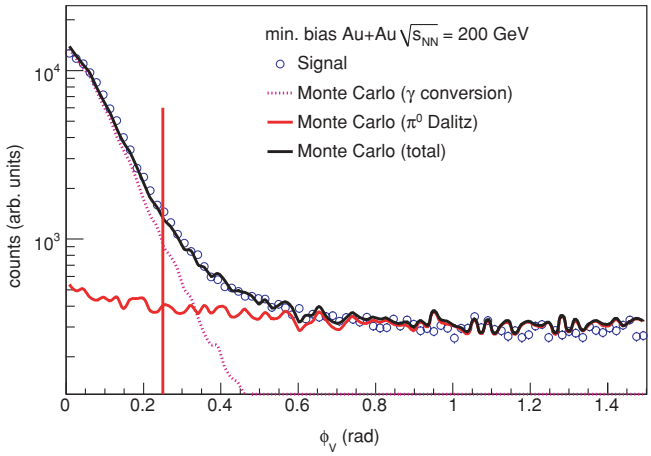

FIG. 5. (Color online) Comparison of the ϕ_V angle distributions in Monte Carlo and data in the mass range $10 < m_{ee} < 30$ MeV/c^2. The vertical red line indicates the cut value used to eliminate photon conversions in this mass bin.

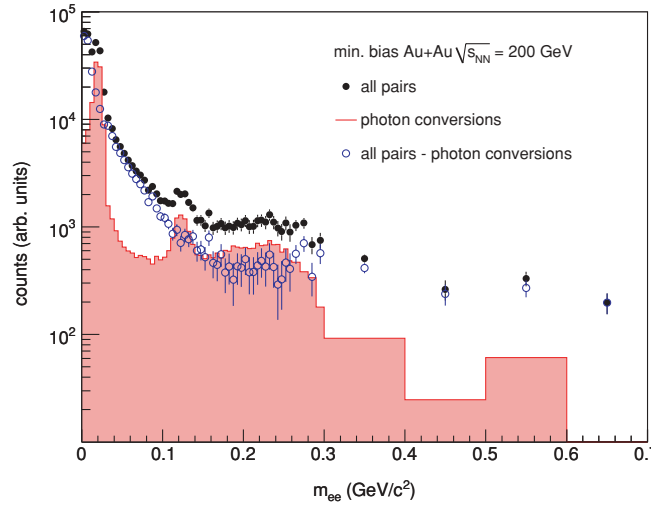

FIG. 6. (Color online) Invariant mass spectrum of all the unlike-sign pairs after subtraction of combinatorial pairs in Min.Bias Au+Au collisions at $\sqrt{s_{NN}} = 200$ GeV. The filled histogram shows the pairs removed by the ϕ_V angle cut.

The simulations show that the distribution for all unlike-sign pairs originating from photon conversion is strongly peaked at $\phi_V = 0$. In contrast, simulated pairs originating from π^0 Dalitz decays have no strongly preferred orientation. The sum of the Monte Carlo data can be compared to the signal, which in this mass region contains conversion photons, as well as π^0's. Figure 5 shows that the agreement between the signal and the simulation is good. The width of the ϕ_V peak for photon conversions increases with the path length of the e^+e^- pair in the magnetic field, where residual field in the polar direction as well as multiple scattering cause the pair to lose its perfect alignment perpendicular to the $\vec{z}$ axis.

The contribution from conversion pairs as a function of the (mis-reconstructed) invariant mass is shown in Fig. 6 (filled histogram). As the (mis-reconstructed) mass is essentially proportional to the radius where the conversion happens, the mass spectrum of those pairs allows a "tomography" of the material in the spectrometer. The peaks correspond to the conversions in the beam-pipe material ($r = 4$ cm or $m_{ee} = 20\,\text{MeV}/c^2$) and detector support structures ($r = 25$ cm or $m_{ee} = 125$ MeV/c^2). Conversions in the He bag generates pairs with $m_{ee} \lesssim 0.3$ GeV/c^2. For this value of mass the corresponding radius would be the entrance window of the DC. At this point though the electrons do not bend anymore because the region is field-free and are therefore removed with a p_T cut ($p_T < 20$ GeV/c) on the single electrons. The ϕ_V resolution improves for increasing conversion radius because electrons are less modified from their original direction by multiple scattering or the residual polar field. The cut on ϕ_V (indicated in Fig. 5 by the line at $\phi_V > 0.25$ for $m_{ee} < 30$ MeV/c^2) is reduced for larger masses due to the improved resolution of ϕ_V at larger radii. By varying the cut values on real pairs we estimate that our ϕ_V cut removes more than 98% of the conversion pairs with a mass-dependent efficiency of more than 90%. The uncertainty of on the final e^+e^- pair signal is 6%.

2. *Type II background*

After removing type I background, the unlike-sign foreground spectrum N_{+-} measures the physical signal plus background, while the like-sign spectra N_{++}, N_{--} measure only background. We have developed two methods to measure and subtract the unlike-sign background

(i) One solution is to use a mixed-event technique, which combines tracks from different events. With this method the background has much larger statistics than the foreground. The accuracy in the determination of the shape of the background is tested by comparing the like-sign distribution in real and mixed events. We find good agreement between real and mixed-events like-sign spectra in some regions of the (m_{ee}, p_T) plane, while in others they clearly deviate. This indicates that not all the type II background is of uncorrelated origin, but there are also some correlated pairs in the background (subsection III D2) that one needs to separately account for.

(ii) Another solution is to still use the measured like-sign spectra and correct them for the different acceptance (subsection III D3). This solution does not require any assumption on the decomposition of combinatorial and correlated since the like-sign spectra measures all the backgrounds simultaneously. In experiments with equal acceptance for electrons and positrons, the background can be measured directly through the geometric mean of the like-sign pair distributions $2\sqrt{N_{++}N_{--}}$. With this method the background has similar statistics as the foreground. In PHENIX, however, the mass and p_T dependence of the background is different for the two charge combinations [see Eq. (3) and Fig. 4].

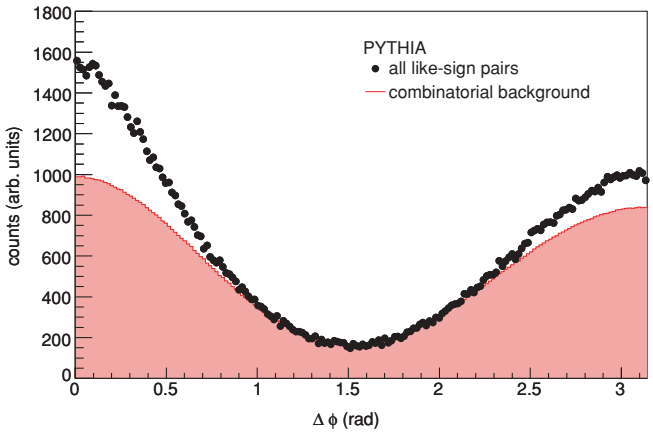

FIG. 7. (Color online) $\Delta\phi$ distribution of like-sign pairs for real and mixed events calculated by PYTHIA [51].

We have used both these methods, which are compared in subsection III D4, to assign a systematic uncertainty to the background subtraction. The first method is used for the final analysis.

The structure of the type II background was studied using minimum bias events generated with PYTHIA [51] with the branching ratio of the π^0 Dalitz decay set to 100% to enhance the sample of e^+e^- pairs per event. All the electrons are filtered through the PHENIX acceptance. From PYTHIA events we make real and mixed-event like- and unlike-sign distributions as in the real data. Now we analyze like-sign pairs that contain only background. The $\Delta\phi$ distribution shown in Fig. 7 compares the difference of azimuthal emission angle of the two electrons (or positrons) in real and mixed PYTHIA events. If the two shapes were identical, we would conclude that all the background come from uncorrelated sources. However, the shapes clearly deviate at $\Delta\phi \sim 0$ and $\Delta\phi \sim \pi$. This indicates the presence of combinations that arise from the *same* jet ($\Delta\phi \sim 0$) or *back-to-back* ($\Delta\phi \sim \pi$) jets (see subsection III D2). In addition, correlations can occur if there are two e^+e^- pairs in the final state of a meson, e.g., double Dalitz decays, Dalitz decays followed by a conversion of the decay photon, or two-photon decays followed by conversion of both photons.

Therefore, we decompose the type II background into two components: a combinatorial background made of uncorrelated pairs and a background of correlated pairs. The distributions for combinatorial and correlated background are determined with methods that are explained below (III D2) for like and unlike-sign spectra. The like-sign background distributions are fit to the measured like-sign spectra (that contain only background). The same fit parameters are then applied to the unlike-sign background. The normalized unlike-sign background is finally subtracted from the foreground of all pairs N_{+-} to obtain the signal.

a. Combinatorial background. The *combinatorial background* $B^{\rm comb}$ is determined with a mixed-event technique, which combines tracks from different events with similar centrality, z vertex, and reaction plane. In the $p+p$ data, where we use a triggered data set, the mixed-event pairs are constructed from the Min.Bias data set requiring that at least one of the two partners has fulfilled the ERT trigger condition. Since the tracks are from different events, this technique reproduces the uncorrelated background by definition. This technique also allows computation of background spectra with negligible statistical errors.

We compare like-sign spectra in real and mixed-event data to locate a region in the (m_{ee}, p_T) plane where their shapes agree. In this region we normalize the combinatorial background spectra $B^{\rm comb}_{\pm\pm}$ to the measured like-sign pairs $N_{\pm\pm}$. We define:

$$\begin{aligned} A_+ &= \frac{\int_{\rm N.R.} N_{++}(m_{ee}, p_T)}{\int_{\rm N.R.} B_{++}(m_{ee}, p_T)} dm_{ee} dp_T \\ A_- &= \frac{\int_{\rm N.R.} N_{--}(m_{ee}, p_T)}{\int_{\rm N.R.} B_{--}(m_{ee}, p_T)} dm_{ee} dp_T, \end{aligned} \tag{9}$$

where N.R. is the chosen normalization region. Then we calculate the integral of the normalized like-sign background over the full phase space:

$$\begin{aligned} \mathcal{B}_{++} &= \int_0^\infty A_+ \times B_{++}(m_{ee}, p_T) dm_{ee} dp_T \\ \mathcal{B}_{--} &= \int_0^\infty A_- \times B_{--}(m_{ee}, p_T) dm_{ee} dp_T. \end{aligned} \tag{10}$$

The unlike-sign background is then normalized such that its yield equals the geometric mean of the like-sign pairs $2\sqrt{\mathcal{B}_{++}\mathcal{B}_{--}}$:

$$B_{+-}(m_{ee}, p_T) = \frac{2\sqrt{\mathcal{B}_{++}\mathcal{B}_{--}}}{\int_0^\infty B_{+-}(m_{ee}, p_T) dm_{ee} dp_T} B_{+-}(m_{ee}, p_T). \tag{11}$$

Appendix A shows that as long as electrons and positrons are produced in pairs the absolute normalization of the unlike-sign background is given by the geometric mean of the observed positive and negative like-sign pairs $2\sqrt{N_{++}N_{--}}$, with no further assumption about efficiencies, acceptances, or probability distribution functions for the pair. Using $\mathcal{B}_{++}$ and $\mathcal{B}_{--}$ instead of directly taking N_{++} and N_{--} simply avoids counting correlated pairs, which will be measured and normalized separately (subsection III D2).

The systematic uncertainty of the normalization is therefore determined by the statistical accuracy of the measured like-sign yield in the region chosen for the normalization.

b. Combinatorial background in $p+p$ data. In our PYTHIA [51] studies we found (Fig. 7) that at $\Delta\phi \sim 0$ and $\Delta\phi \sim \pi$ the real events background deviates from the shape of uncorrelated sources, while at $\Delta\phi \sim \pi/2$ it looks consistent with the shape from mixed events. Considering that $m_{ee}^2 = 2p_1p_2(1 - \cos\Delta\omega)$, with $\Delta\omega$ being the opening angle, this condition corresponds to a region in the (m_{ee}, p_T) plane where $m_{ee} \sim p_T$.

We define this region empirically by a set of equations:

$$\begin{aligned} m_{ee} &> 0.3\ {\rm GeV}/c^2 \\ m_T &< 1.2\ {\rm GeV}/c^2 \\ p_T/c - 1.5m_{ee} &\leqslant 0.2\ {\rm GeV}/c^2 \\ p_T/c - 0.75m_{ee} &\geqslant 0\ {\rm GeV}/c^2, \end{aligned} \tag{12}$$

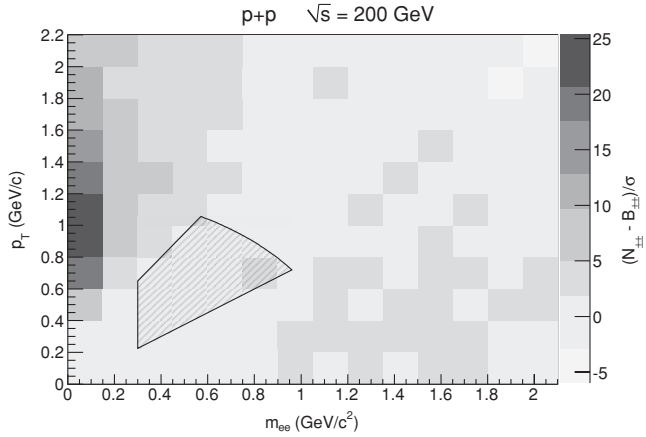

FIG. 8. Difference between real and mixed-events like-sign distributions divided by its standard deviation $(N_{\pm\pm} - B^{\rm comb}_{\pm\pm})/\sigma_{(N_{\pm\pm}-B^{\rm comb}_{\pm\pm})}$. The background $B^{\rm comb}_{\pm\pm}$ is normalized to the foreground $N_{\pm\pm}$ in the normalization region shown by the dashed area.

where $m_T = \sqrt{p_T^2 + m_{ee}^2}$ is the transverse mass of the pair. This region is shown in Fig. 8 by the dashed area.

Figure 8 shows the difference between the like-sign distributions in real and mixed events as a function of m_{ee} and p_T. The background $B^{\rm comb}_{\pm\pm}$ is normalized to the foreground $N_{\pm\pm}$ in the normalization region [from Eq. (12)]. The absolute normalization of the unlike-sign combinatorial background is determined with an uncertainty given by the statistical error of the measured like-sign spectra in this region of 3%. The difference between real and mixed $N_{\pm\pm} - B^{\rm comb}_{\pm\pm}$ is divided by its standard deviation. Figure 8 shows that in this region the background does not deviate from the foreground by more than $2 \times \sigma$. The stability of the results has been checked by varying the normalization region, and the difference is included in the systematic uncertainty.

c. Combinatorial background in Au+Au data. Figure 9 shows a comparison between the like-sign distribution from real and mixed events. The comparison shows that the mixing technique reproduces the mass dependence within the statistical accuracy of the data not only in the normalization region for the $p+p$ data but also for all masses above 0.55 GeV/c^2. In general the larger combinatorial background produced in the Au+Au environment reduces the capability to distinguish between different background shapes. Also the agreement at high mass, which was not observed in $p+p$ (see Fig. 8), can be qualitatively explained by the suppression of away-side jets observed in Au+Au [52].

A small signal from correlated background remains at low masses (see subsection III D2). To quantitatively compare the mass dependence of the data to the mixed events we calculate the ratio $(N_{\pm\pm} - B^{\rm comb}_{\pm\pm})/B^{\rm comb}_{\pm\pm}$ shown in the bottom

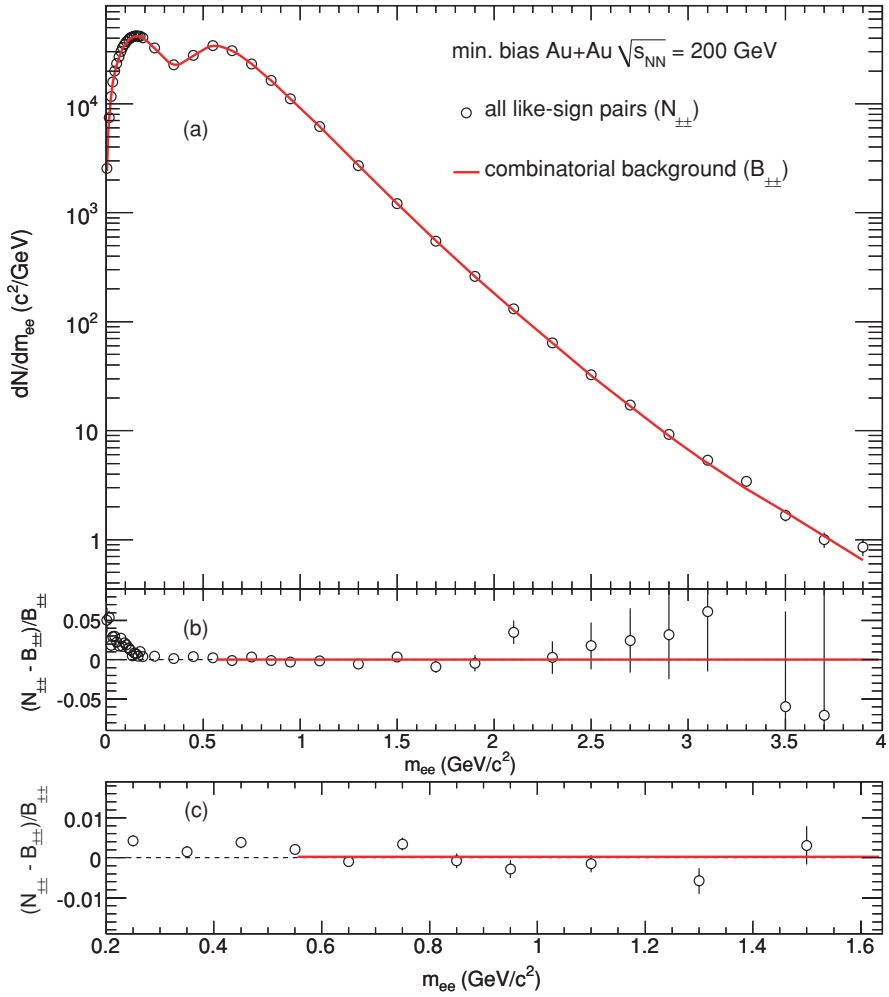

FIG. 9. (Color online) (a) Like-sign distribution for real $N_{\pm\pm}$ and mixed events $B^{\rm comb}_{\pm\pm}$. [(b) and (c)] Ratio of $(N_{\pm\pm} - B^{\rm comb}_{\pm\pm})/B^{\rm comb}_{\pm\pm}$ with two different scales.

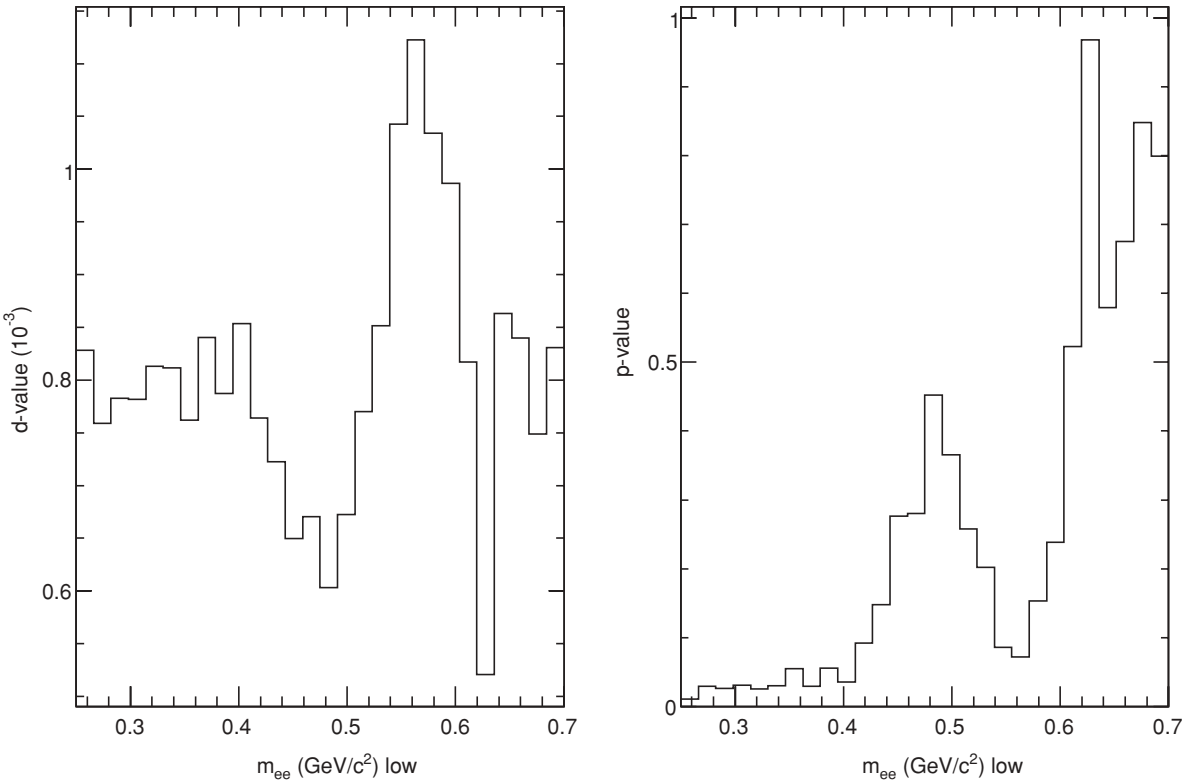

FIG. 10. (Left) Maximum cumulative fractional distance d of the two like-sign distributions. The distance is calculated from a lower end point m_{low} to infinity. The test gives a maximum deviation of 0.1%. (Right) Corresponding Kolmogorov-Smirnov p value as a function of the lower end point m_{low}, i.e., for $m_{ee} > m_{\text{low}}$. The p value increases for $m_{\text{low}} > 0.55$ GeV/c^2, reaching values of ~90%, confirming the hypothesis of compatibility of the two distributions in the region chosen for the normalization.

panels of Fig. 9 and fit it with a constant above the η mass (0.55 GeV/c^2). The result is $(-2.59 \pm 6.33) \times 10^{-4}$ with $\chi^2/\text{NDF} = 27.6/19$. Figure 9(b) shows the entire mass range and allows us to distinguish the signal from correlated background at very low mass. Figure 9(c) shows a zoom in the region where we fit.

Two statistical tests are performed to test the hypothesis that the two distributions ($N_{\pm\pm}$ and $B^{\text{comb}}_{\pm\pm}$) represent identical distributions: the Pearson χ^2 test and the Kolmogorov-Smirnov test. The Pearson test statistic χ^2 resulting from the comparison of real and mixed events for $m_{ee} > 0.55$ GeV/c^2 returns a p value greater than 0.83. The Kolmogorov-Smirnov test is used to decide if a sample comes from a population with a specific distribution, either comparing one fluctuating distribution (the test) to a truth hypothesis (reference), or querying two fluctuating distributions as to whether they have a common truth origin. This latter one was done in our case since we do not have a truth reference distribution without fluctuations. The test is based on the maximum cumulative difference between the distribution under test and a specified reference distribution. The left panel of Fig. 10 shows the maximum cumulative difference d of the two like-sign distributions $N_{\pm\pm}$ and $B^{\text{comb}}_{\pm\pm}$ for $m_{ee} > m_{\text{low}}$, where m_{low} is the lower end point chosen between 0.25 and 0.7 GeV/c^2. The Kolmogorov-Smirnov test gives a maximum deviation of 0.1% which is small compared to the uncertainty of the absolute normalization of the mixed-event background. The corresponding Kolmogorov-Smirnov p value is also shown in the right panel of Fig. 10 as a function of mass. It is small below 0.55 GeV/c^2, where there is some contribution of the correlated background. However, for $m_{\text{low}} > 0.55$ GeV/c^2, the p value is ~90%, therefore confirming that the hypothesis of compatibility of the two distributions for $m_{\text{low}} > 0.55$ GeV/c^2 is valid for any commonly used significance level.

Figure 11 shows the like-sign mass distribution for real and mixed events in the different centrality bins used in the analysis. The bottom panels show the ratio $(N_{\pm\pm} - B^{\text{comb}}_{\pm\pm})/B^{\text{comb}}_{\pm\pm}$ which are fit to a constant for $m_{ee} > 0.55$ GeV/c^2. The fit results for all centralities are reported in Table III together with the results of the statistical tests described above. The results reported in Table III demonstrate that the agreement between real and mixed-event like-sign mass spectra demonstrated for minimum bias collisions also holds for all centrality classes.

Figure 12 shows the like-sign mass distribution for real and mixed events in different p_T bins. The ratio $(N_{\pm\pm} - B^{\text{comb}}_{\pm\pm})/B^{\text{comb}}_{\pm\pm}$ shows a good agreement between real and mixed-event distribution for all bins. This demonstrates that, within the statistical error of the foreground, there is no deviation from uncorrelated combinatorial behavior for masses above 0.55 GeV/c^2 in any p_T range.

The absolute normalization of the unlike-sign combinatorial background is determined with an uncertainty given by the statistical error of the measured like-sign spectra for $m_{ee} >$ 0.7 GeV/c^2 of 0.12%. The mass interval ($m_{ee} > 0.7$ GeV/c^2)

TABLE III. Fit parameters for the mass dependence comparison of real and mixed-events like-sign pairs for different centrality and p_T bins. The second column reports the results of $(N_{\pm\pm} - B^{\rm comb}_{\pm\pm})/B^{\rm comb}_{\pm\pm}$ distributions to a constant and the third is χ^2 value divided by the number of degrees of freedom. The fourth and fifth columns report the result of a χ^2 statistical test and the corresponding p value for $m_{ee} > 0.55$ GeV/c^2. The last one gives the maximum deviation of the $N_{\pm\pm}$ and $B^{\rm comb}_{\pm\pm}$ distribution in a Kolmogorov-Smirnov test.

Centrality	p_0	χ^2/NDF	χ^2 test	p value	Max dev.
0–10%	$6.3 \pm 8.8 \times 10^{-4}$	30.2/19	1.05	0.25	0.0014
10–20%	$-9.4 \pm 1.4 \times 10^{-4}$	18.6/19	0.97	0.61	0.0018
20–40%	$-2.4 \pm 1.8 \times 10^{-3}$	18.7/19	1.02	0.40	0.0034
40–60%	$-8.5 \pm 4.9 \times 10^{-3}$	21.9/19	1.65	0.02	0.0071
60–92%	$-1.8 \pm 1.6 \times 10^{-2}$	21.5/14	1.51	0.04	0.0321
00–92%	$2.6 \pm 6.3 \times 10^{-4}$	27.6/19	0.92	0.83	0.0010
$p_T < 1$ GeV/c	$9.2 \pm 5.1 \times 10^{-4}$	18.9/18	0.95	0.73	0.0011
$1 < p_T < 2$ GeV/c	$-3.4 \pm 1.6 \times 10^{-3}$	27.9/18	0.91	0.84	0.0029
$p_T > 2$ GeV/c	$-9.6 \pm 5.4 \times 10^{-3}$	15.2/18	0.97	0.63	0.0038

is sufficiently large to achieve the desired statistical accuracy and is conservatively chosen to exclude any possible region which may be contaminated by the correlated background. The results are stable when varying the lower end of the normalization region between 0.55 and 0.7 GeV/c^2 and the difference is included in the systematic uncertainty. Because the pair cuts remove more like-sign than unlike-sign pairs (see subsection III D1), the normalization factor is corrected by this asymmetry, which is estimated with mixed events to be 1.004 ± 0.002, independent of centrality.

For the various centrality bins and minimum bias collisions, the 0.2% uncertainty on the event rejection is added in quadrature to the uncertainty on the normalization, which is determined by the statistics of the like-sign pairs. Since the ratios shown in Figs. 9, 11, and 12 show no systematic deviation in shape between the like-sign real- and mixed-event distribution for $m_{ee} > 0.55$ GeV/c^2, the uncertainty due to the shape is negligible compared to the uncertainty on the normalization. The total uncertainty on the combinatorial background is given in Table IV.

This translates into a systematic uncertainty δS on the signal S of $\delta S/S = (\delta B^{\rm comb}/B^{\rm comb})/(S/B^{\rm comb})$. $\delta B^{\rm comb}/B^{\rm comb}$ for minimum bias collisions and all centrality bins are listed in Table IV. Figure 13 shows $S/B^{\rm comb}$ for different ranges of pair-p_T and centrality.

TABLE IV. Systematic uncertainty on the combinatorial background for $p+p$ and various centrality classes of Au+Au collisions.

Centrality	$\delta B^{\rm comb}/B^{\rm comb}$ (%)
0–92%	0.25
0–10%	0.25
10–20%	0.30
20–40%	0.35
40–60%	0.85
60–92%	2.50
$p+p$	3.00

d. Correlated background. After subtracting the combinatorial background, the remaining pair distributions, like- and unlike-sign, are considered correlated pairs, where the like-sign distribution only contains correlated background pairs while the unlike-sign also contains the signal.

$$N_{\pm\pm} - B^{\rm comb}_{\pm\pm} = B^{\rm corr}_{\pm\pm} \tag{13}$$

$$N_{+-} - B^{\rm comb}_{+-} = B^{\rm corr}_{+-} + S_{+-} \tag{14}$$

The *correlated background* $B^{\rm corr}$ arises from two sources.

The first source is "cross pairs." They occur if there are two e^+e^- pairs in the final state of a meson, e.g., double Dalitz decays, Dalitz decays followed by a conversion of the decay photon or two-photon decays followed by conversion of both photons. Besides the real unlike-sign signal, this leads to like- and unlike-sign cross pairs. While all mesons in principle produce cross pairs, all contributions above the η mass (0.55 GeV/c^2) can be safely neglected. Like- and unlike-sign cross pairs were simulated using our hadron decay generator, including the PHENIX acceptance [Eq. (3)]. Because their rate is proportional to the Dalitz decay probability only, the ratio of cross pairs to pions is independent of centrality.

The second source is "jet pairs." They are produced by two independent hadron decays yielding electron pairs, either within the same jet or in back-to-back jets. Jet pairs were simulated using the minimum bias events generated with PYTHIA [51] as described above. As noted previously, correlated pairs from the same jet typically have small mass and large p_T while those from back-to-back jets have large mass and smaller p_T.

Correlated background pairs equally populate like- and unlike-sign combinations. Since the like-sign spectrum measures only the background, we can determine the cross and jet pair yields by simultaneously fitting simulated cross and jet pair distributions to the measured correlated like-sign pairs, after subtraction of combinatorial background. The resulting normalization factors, one for cross and one for jet pairs, are then applied to the unlike-sign correlated background.

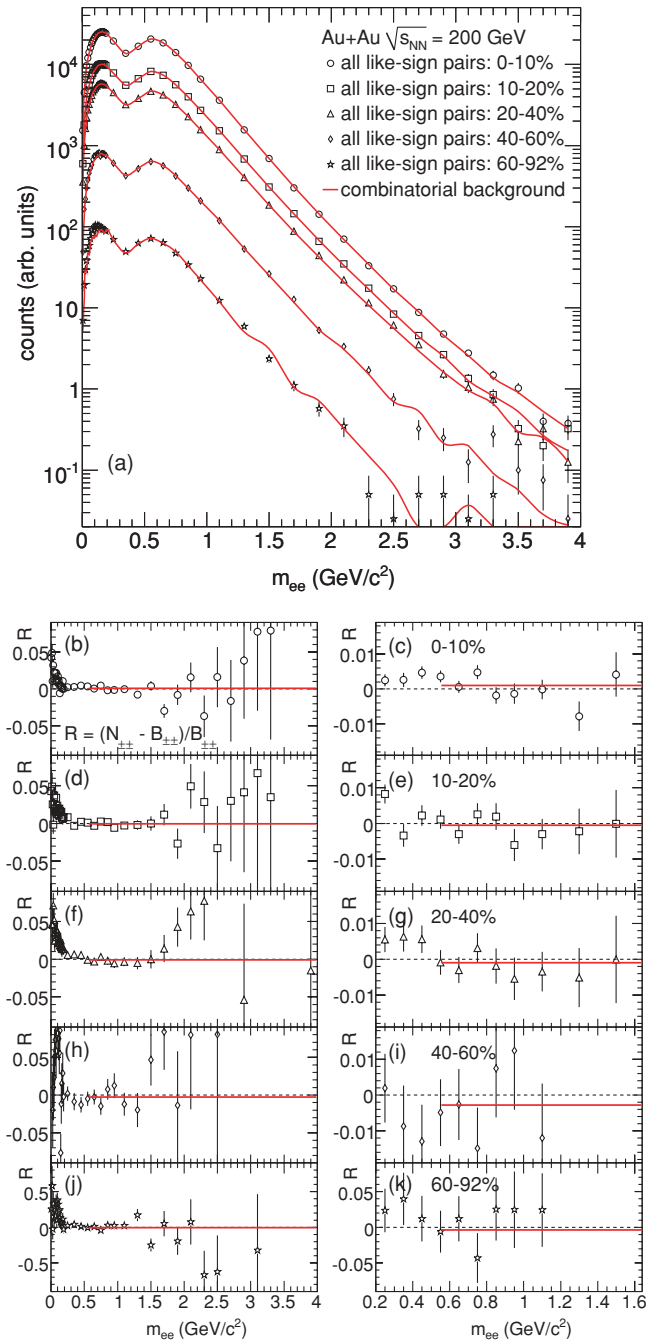

FIG. 11. (Color online) Like-sign distribution for real $N_{\pm\pm}$ and mixed events $B_{\pm\pm}^{\rm comb}$ for different centrality data sets. The bottom panels show the ratios $(N_{\pm\pm} - B_{\pm\pm}^{\rm comb})/B_{\pm\pm}^{\rm comb}$ with different scales. The left ones show all the mass range and allow to identify the correlated background at low masses. The right ones focus on mass region where we fit.

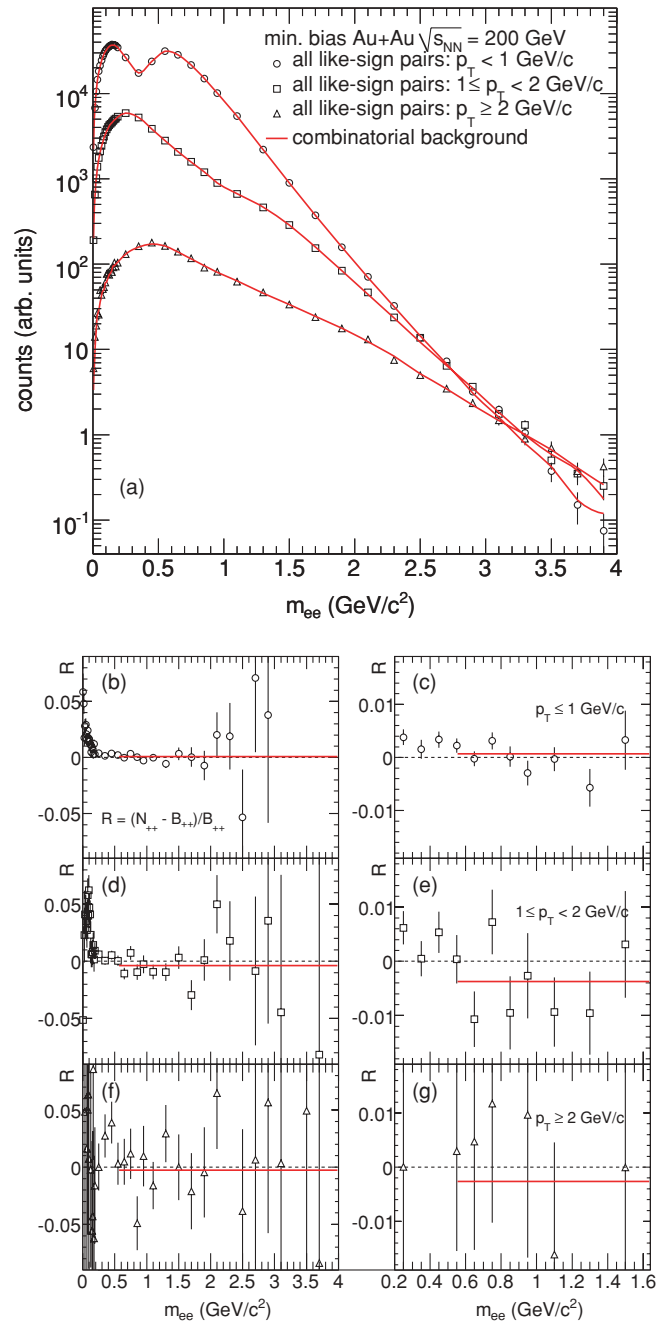

FIG. 12. (Color online) Like-sign distribution for real and mixed events for different p_T bins. The bottom panels show the ratio of $(N_{\pm\pm} - B_{\pm\pm}^{\rm comb})/B_{\pm\pm}^{\rm comb}$ with different scales. The left ones show all the mass range and allow to identify the correlated background at low masses. The right ones focus on mass region where we fit.

e. Correlated background in p+p data. Figure 14(a) shows like-sign pair distributions: $N_{\pm\pm}$, $B_{\pm\pm}^{\rm comb}$, and $B_{\pm\pm}^{\rm corr} = N_{\pm\pm} - B\pm\pm$. Figure 14(b) shows analogous distributions for unlike-sign pairs: N_{+-}, B_{+-}, and $B_{+-}^{\rm corr} = N_{+-} - B_{+-}$.

The like-sign correlated background distribution is fit to

$$B_{\pm\pm}^{\rm corr} = A \times \text{cross} + B \times \text{jet}. \qquad (15)$$

The resulting normalization factors, A and B, are then applied to the unlike-sign correlated background. The unlike-sign signal results from subtracting the correlated background from all correlated unlike-sign pairs.

f. Correlated background in Au+Au data. In Au+Au data the like-sign mixed-event distribution reproduces the mass dependence of the real-event distribution not only in region of Eq. (12), but for all masses above 0.55 GeV/c^2 for every centrality, as shown in Fig. 11, and at every p_T, as shown

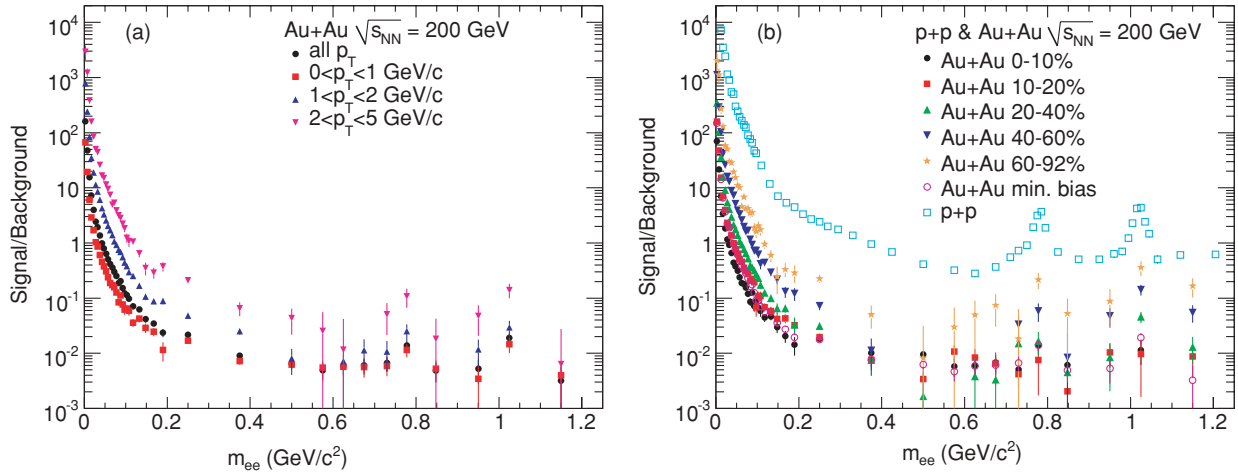

FIG. 13. (Color online) Ratio of signal to background for different ranges of pair-p_T (left) and centrality classes (right).

in Fig. 12. This means that there is no room for correlated background for $m_{ee} > 0.55$ GeV/c^2. Here the contribution that typically arises from back-to-back jets in the Au+Au data is indeed expected to differ from $p+p$ because of the observed jet modifications [52].

We therefore separate the jet distribution into "near-side" (jet$_{\text{near}}$: $\Delta\phi < \pi/2$) and "away-side" contributions (jet$_{\text{away}}$: $\Delta\phi > \pi/2$) and we fit the like-sign correlated background distribution to the sum of

$$B^{\text{corr}}_{\pm\pm} = A \times \text{cross} + B \times \text{jet}_{\text{near}} + C \times \text{jet}_{\text{away}}. \qquad (16)$$

Figures 14(c) and 14(d) show the like- and unlike-sign pair distributions, the normalized mixed-event background, and the distributions after subtraction. We note that the like-sign yield is well described by the sum of combinatorial and correlated background and that the contribution from "away-side-jet pairs" is consistent with zero, i.e., $C = 0$, as the mixed-event distribution was normalized to the real data in the IMR: the "away-side-jet pairs" are therefore not shown. The unlike-sign signal (S_{+-}) is obtained by subtracting from the distribution of all pairs the mixed-event combinatorial background (B^{comb}_{+-}) and the correlated background (B^{corr}_{+-}) normalized

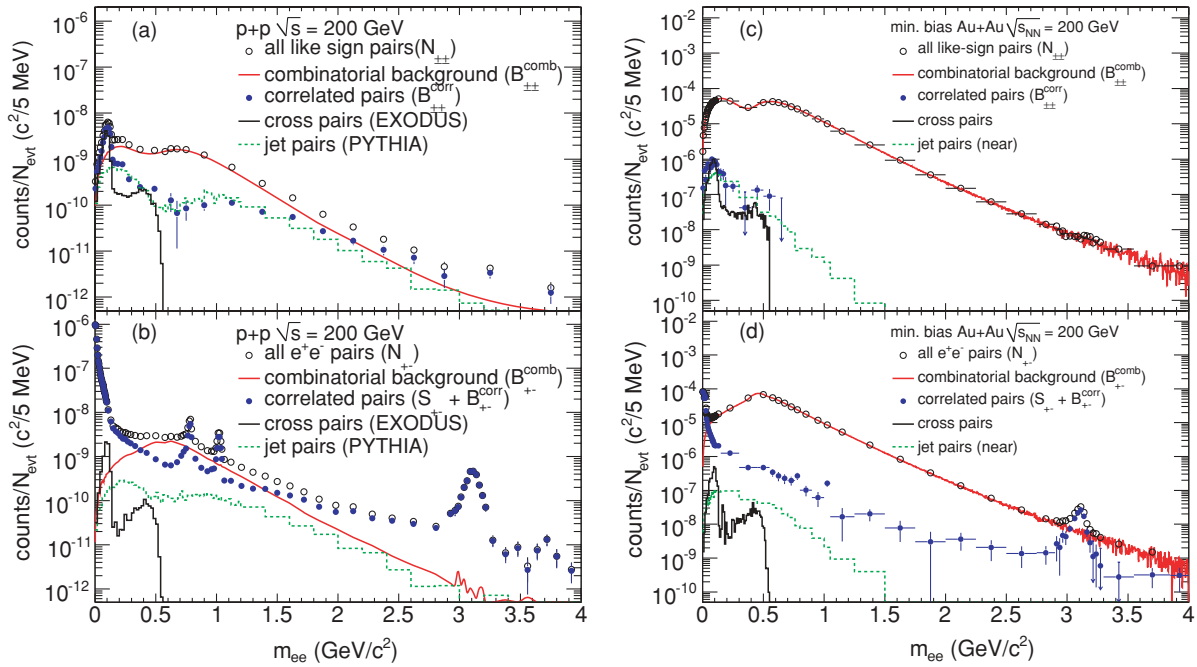

FIG. 14. (Color online) Raw dielectron spectra in $p+p$ (left) and Au+Au (right) collisions. The top panels show like-sign pairs $N_{\pm\pm}$ as measured in the experiment, the combinatorial background from mixed-events $B^{\text{comb}}_{\pm\pm}$, the correlated pair background $B^{\text{corr}}_{\pm\pm}$ obtained by subtracting the combinatorial background, and the individual contributions from cross and jet pairs to the correlated background (see text). The bottom panels show the same distributions for unlike-sign pairs. The correlated like-sign background $B^{\text{corr}}_{\pm\pm}$ is normalized to the measured like-sign pairs remaining after subtracting the combinatorial background $N_{\pm\pm} - B^{\text{comb}}_{\pm\pm}$ and the same factors are applied to the unlike-sign distribution B^{corr}_{+-}.

with the factors A, B, and C measured in the like-sign spectrum.

3. Like-sign subtraction method

The event-mixing technique, along with the determination of correlated backgrounds, used to estimate the background contribution to the measured dilepton mass spectra, was developed in order to get around the problems introduced in a traditional like-sign background calculation by the asymmetric PHENIX acceptance. With a like-sign calculation we need to make only the assumption that the mass dependence of the correlated background is symmetric for like- and unlike-sign pairs. We do not need to make any assumption about the decomposition of the background into "cross," "jet-near-side," and "jet-away-side" pairs. The like-sign distribution measures only the background. Correlated and uncorrelated backgrounds are charge symmetric, i.e., they yield the same number of like- and unlike-sign pairs, with the same distribution. The *measured* distributions, however, differ because of the acceptance.

The acceptance difference between like- and unlike-sign pairs can be measured with the ratio of mixed-event distributions, i.e., $\frac{B^{\rm comb}_{+-}}{2\sqrt{B^{\rm comb}_{++}\cdot B^{\rm comb}_{--}}}$ where $B^{\rm comb}_{+-}$, $B^{\rm comb}_{++}$, $B^{\rm comb}_{--}$ are the number of e^+e^-, e^+e^+, e^-e^- pairs in a given mass and p_T bin. The like-sign distribution can therefore be acceptance-corrected and then subtracted from the unlike-sign pairs.

$$S_{+-} = N_{+-} - 2\sqrt{N_{++}N_{--}}\cdot\frac{B^{\rm comb}_{+-}}{2\sqrt{B^{\rm comb}_{++}\cdot B^{\rm comb}_{--}}}. \quad (17)$$

This technique, however, measures the background distribution with similar statistical error as the foreground, therefore the resulting error on the signal is much larger than when using the mixed-events technique.

One can also use a "hybrid" method where first the mixed events are normalized in the region where real and mixed-event distributions agree [region in Eq. (12) for $p+p$ and $m_{ee} > 0.7$ GeV/c^2 for Au+Au]. Then the correlated background is obtained by correcting the subtracted like-sign distribution by the acceptance difference $\frac{B^{\rm comb}_{+-}}{2\sqrt{B^{\rm comb}_{++}\cdot B^{\rm comb}_{--}}}$.

4. Systematic uncertainty of the background subtraction

The background subtraction is the most critical aspect of this analysis, therefore it is crucial to assign a proper systematic uncertainty to it. In subsection III D2 we reported the systematic uncertainty on the normalization of the combinatorial background determined by the statistical accuracy of the measured like-sign yield (see Table IV). The uncertainty on the shape of combinatorial background is everywhere negligible compared to the uncertainty on the normalization.

To evaluate the systematic uncertainty due to the correlated pairs we compare the results obtained with the two subtraction methods. It is important to note that the contribution of the correlated background is everywhere small compared to the signal. Therefore any uncertainty in its estimate would result in a small uncertainty on the signal.

In the first subtraction method the correlated background $B^{\rm corr}_{+-}$ was calculated using Monte Carlo simulations. We have estimated potential spectral shape modifications of $B^{\rm corr}_{+-}$ in several ways, shown in Fig. 15. In Au+Au

(i) we have not subtracted any jet background (this would clearly result in an upper limit);
(ii) we have subtracted the near side normalizing it for $m_{ee} > 0.55$ GeV/c^2;
(iii) we have subtracted both near and away-side using for the away-side the same normalization as for the near-side (this would clearly result in a lower limit);
(iv) we have subtracted the near side normalizing it for $70^\circ < \Delta\phi < 110^\circ$;
(v) we have subtracted the near side normalizing it for $70^\circ < \Delta\phi < 110^\circ$ and we have corrected the shape for the eID efficiency.

In the second subtraction method, both in $p+p$ and Au+Au, we use the like-sign corrected for the different acceptance or a hybrid method which uses the mixed-event distribution for the combinatorial background and the like-sign distribution corrected for the different acceptance for the correlated background only.

Since the acceptance for pairs is a function of mass and p_T, we have checked that for different e^+e^- pair sources, which span reasonable variations in mass and p_T shapes of the e^+e^- pairs, the relative acceptance is unchanged. For this purpose in $p+p$ we have calculated the relative acceptance:

(i) using data from $p+p$ run only;
(ii) using data from Au+Au run only;
(iii) using data from PYTHIA real events;
(iv) using data from PYTHIA mixed events.

We added the results from these two methods in Fig. 15 as well. The agreement within the different methods (see rms/mean in the bottom panel) allows to assign a systematic uncertainty on the signal.

E. Raw mass spectrum

Figure 16 shows the mass distribution of e^+e^- pairs, the normalized mixed-event background (B), and the signal yield (S) obtained by subtracting the mixed-event background and the correlated background (cross and jet pairs) for Min.Bias Au+Au collisions. The right panel shows the signal-to-background ratio ($S/B^{\rm comb}$). The systematic uncertainties (boxes) reflect the uncertainty from the background subtraction, which is given by $\delta_S/S = 0.25\% \times B^{\rm comb}/S$, added in quadrature to the uncertainty due to the correlated background subtraction, conservatively assumed to be around 10%S below 0.55 GeV/c^2. Despite the small $S/B^{\rm comb}$ ratio, an e^+e^- pair continuum is visible up to 4.5 GeV/c^2. Due to the limited statistical precision in Au+Au binning was chosen such that the bins near the ϕ and ω meson are centered at the nominal meson mass. The bin width was chosen to correspond approximately to twice the mass resolution observed in $p+p$ collisions. In this way the ϕ and ω mesons can be resolved from the continuum.

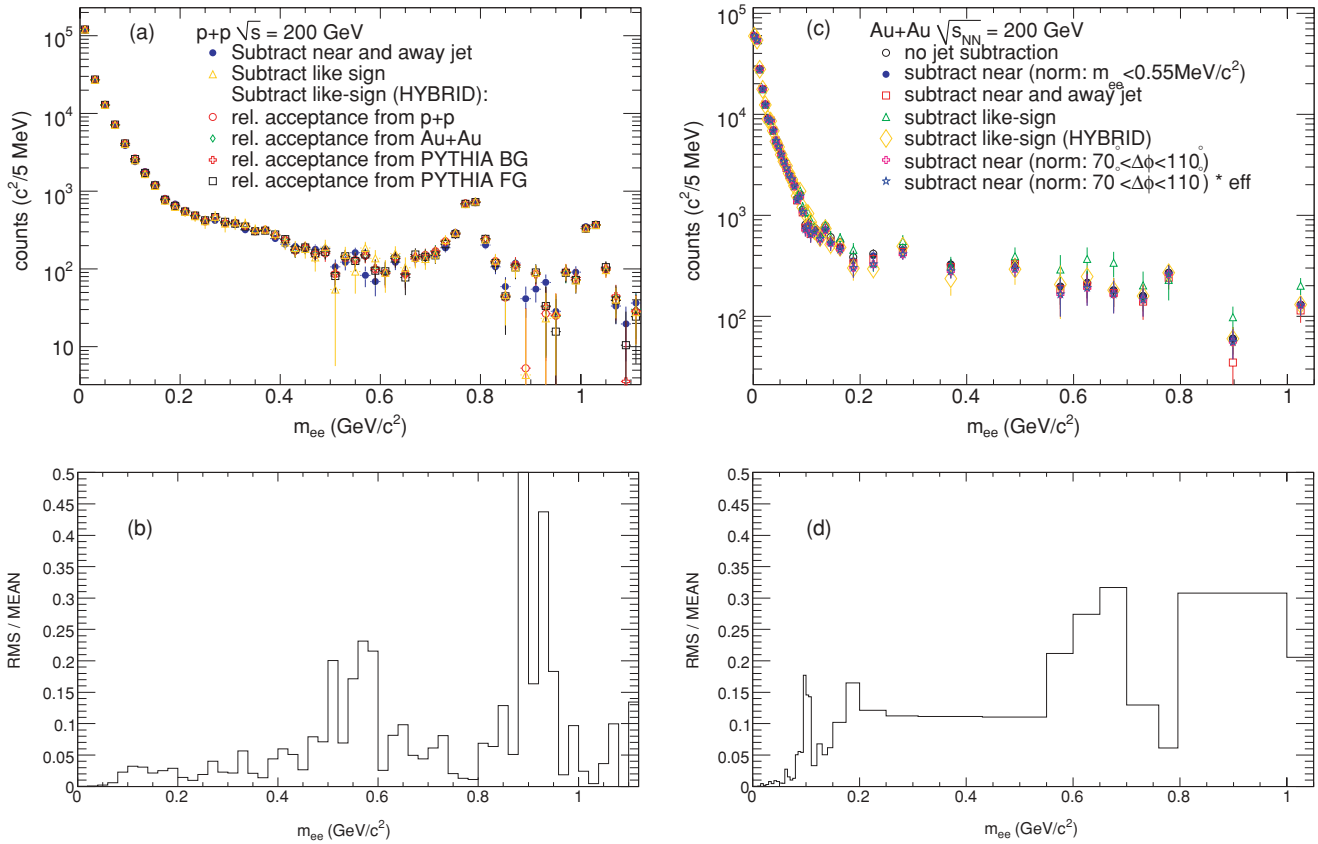

FIG. 15. (Color online) Unlike-sign dielectron spectra obtained by subtracting the background (combinatorial and correlated) with the methods explained in the text for $p+p$ (left) and Au+Au (right). The rms/mean of all the spectra shown in the bottom panels allows to assign a systematic uncertainty on the signal due to correlated background subtraction.

F. Runs with increased conversion material

In order to check the background subtraction, a subset of data (5×10^7 events) was collected with a brass sheet of 1.68% radiation length (X_0) wrapped around the beam pipe to increase the number of photon conversions. We make an estimate on the uncertainty in the radiation length (5%) by comparing photon conversions in data and simulation [6]. Because the additional conversion leads to an increased

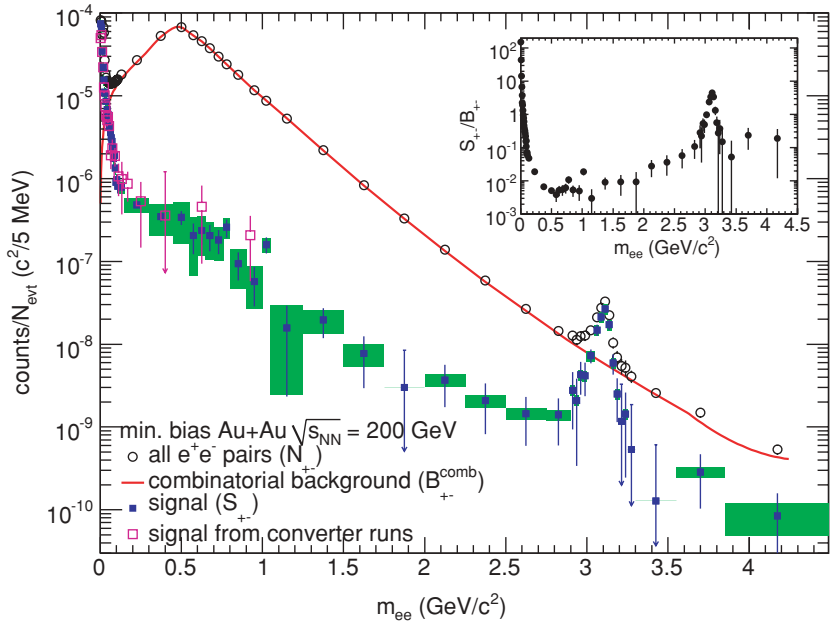

FIG. 16. (Color online) Uncorrected mass spectra of all e^+e^- pairs, mixed-event background (B^{comb}) and signal (S) in minimum bias Au+Au collisions. Statistical (bars) and systematic (boxes) uncertainties are shown separately. The signal from the runs with additional converter material is shown with statistical errors only. The two spectra are normalized by the number of events. The insert shows the S/B^{comb} ratio. The mass range covered by each data point is given by horizontal bars.

electron multiplicity, in this data set the combinatorial and correlated background (B) contribution is larger by a factor of ~2.5.

If there is a systematic bias in background normalization, and the yield of background is off by a small fraction f, it can lead to significant difference between the "apparent" signal and the "true" signal S^{true}. The difference should be larger in the converter run since signal-to-background is smaller. Thus the "apparent" signal S_{C} in the converter run should become larger than the "apparent" signal S_{NC} in normal run without the converter. The relation between S^{true}, S_{C}, S_{NC} can be written as:

$$\begin{aligned} S_{\text{NC}} &= N_{\text{NC}} - (1-f)\times B \\ &= S^{\text{true}} + fB \end{aligned} \tag{18}$$

$$\begin{aligned} S_{\text{C}} &= N_{\text{C}} - 2.5\times(1-f)\times B \\ &= S^{\text{true}} + 2.5fB, \end{aligned} \tag{19}$$

where N_{C} (N_{NC}) is the foreground of all e^+e^- pairs in converter (nonconverter) runs. If we divide Eq. (18) by B, we obtain:

$$\begin{aligned} \frac{S}{B} = \frac{S_{\text{NC}}}{B} &= \frac{S^{\text{true}}+fB}{B} \\ S^{\text{true}} + fB &= (S/B)B. \end{aligned} \tag{20}$$

Then the ratio between the apparent signal in converter and nonconverter runs is given by:

$$\begin{aligned} \frac{S_{\text{C}}}{S_{\text{NC}}} &= \frac{S^{\text{true}}+2.5fB}{S^{\text{true}}+fB} \\ &= \frac{S^{\text{true}}+fB+1.5fB}{S^{\text{true}}+fB} \\ &= \frac{(S/B)B+1.5fB}{(S/B)B} \\ &= \frac{S/B+1.5f}{S/B} \\ &= 1+1.5f\frac{B}{S}. \end{aligned} \tag{21}$$

Therefore

$$f = \left(\frac{S_{\text{C}}}{S_{\text{NC}}}-1\right)\frac{S}{B}\frac{1}{1.5}. \tag{22}$$

This means we can use the agreement between converter and nonconverter runs $S_{\text{C}}/S_{\text{NC}}$, shown in Fig. 16, and the signal-to-background ratio S/B also shown in the insert of Fig. 16 to constrain a potential bias f in the background normalization.

In $0.3 < m_{ee} < 0.75$ MeV/c^2

$$\frac{S_{\text{C}}}{S_{\text{NC}}} = 1.29 \pm 0.92$$

and

$$\frac{S}{B} = (7.47 \pm 0.55)10^{-3}$$

constrain $f = (0.14 \pm 0.46)10^{-2}$. If we extend the mass range to lower values $0.04 < m_{ee} < 0.75$ MeV/c^2,

$$\frac{S_{\text{C}}}{S_{\text{NC}}} = 1.08 \pm 0.28$$

and

$$\frac{S}{B} = (2.75 \pm 0.05)10^{-2},$$

the constraint becomes $f = (0.15 \pm 0.51)10^{-2}$.

The agreement between the converter run and the normal run confirms that the systematic bias in the background normalization is small ($0.15 \pm 0.51\%$). The result is consistent with our estimate of the systematic uncertainty in the background normalization (0.25%). It should be noted that the converter run provides an independent test on the background normalization.

G. Efficiency correction

The e^+e^- mass spectra are corrected for the total pair reconstruction efficiency $\epsilon_{\text{pair}}^{\text{total}}$ to give the e^+e^- pair yield inside the PHENIX aperture as defined by Eq. (3):

$$\frac{dN}{dm_{ee}} = \frac{1}{N_{\text{evt}}}\frac{N_{ee}}{\Delta m_{ee}}\frac{1}{\epsilon_{\text{pair}}^{\text{total}}}. \tag{23}$$

The p_T spectra are further corrected for the pair geometric acceptance ($\epsilon_{\text{pair}}^{\text{geo}}$) to give the e^+e^-–pair yield in one unit of rapidity:

$$\frac{1}{2\pi p_T^{ee}}\frac{d^2N}{dp_T^{ee}dy^{ee}} = \frac{1}{2\pi p_T^{ee}}\frac{1}{N_{\text{evt}}}\frac{N_{ee}}{\Delta p_T^{ee}\Delta y}\frac{1}{\epsilon_{\text{pair}}^{\text{total}}}\frac{1}{\epsilon_{\text{pair}}^{\text{geo}}}. \tag{24}$$

The $p+p$ data are further corrected by the factor $\frac{\epsilon_{\text{BBC}}}{\epsilon_{\text{bias}}}$, where $\epsilon_{\text{BBC}} = 54.5 \pm 5\%$ is the BBC efficiency and $\epsilon_{\text{bias}} = 79 \pm 2\%$ is the BBC trigger bias, described above (subsection III A).

The total pair reconstruction efficiency $\epsilon_{\text{pair}}^{\text{total}}$ depends on the single-electron efficiency for reconstruction and eID ($\epsilon_{\text{single}}^{\text{eID}}$), the efficiency from the detector live area ($\epsilon_{\text{single}}^{\text{live}}$), the occupancy efficiency ($\epsilon_{\text{single}}^{\text{occ}}$) (for Au+Au). The occupancy efficiency ($\epsilon_{\text{single}}^{\text{occ}}$) differs for each Au+Au centrality class and is described in subsection III J. The $p+p$ data are also corrected for the ERT trigger efficiency, described in subsection III I. In addition, the effect of the pair cuts ($\epsilon_{\text{pair}}^{\phi_V}$ and $\epsilon_{\text{pair}}^{\text{ghost}}$) is taken into account:

$$\begin{aligned} \epsilon_{\text{pair}}^{\text{total}} = \epsilon_{\text{pair}}^{\text{eID}} \cdot \epsilon_{\text{pair}}^{\text{live}} \cdot \epsilon_{\text{pair}}^{\phi_V} \cdot \epsilon_{\text{pair}}^{\text{ghost}} \cdot \epsilon_{\text{pair}}^{\text{occ}} \quad &\text{(for Au+Au)} \\ \cdot \epsilon_{\text{pair}}^{\text{ERT}} \quad &\text{(for } p+p\text{)}. \end{aligned} \tag{25}$$

These efficiencies depend on the eID cuts used to determine the electron sample, therefore they do factorize only on the condition that the electron sample used to calculate them is the same for all of them.

The pair-eID and reconstruction efficiency $\epsilon_{\text{pair}}^{\text{eID}}$ and pair-live efficiency $\epsilon_{\text{pair}}^{\text{live}}$, as well as the ERT efficiency $\epsilon_{\text{pair}}^{\text{ERT}}$ for $p+p$ data are derived, as a function of mass and pair-p_T, from the corresponding single-electron efficiency ($\epsilon_{\text{single}}^{\text{eID}}$, $\epsilon_{\text{single}}^{\text{live}}$, and $\epsilon_{\text{single}}^{\text{ERT}}$, respectively) using the pair kinematic properties implemented in our hadron decay generator, as explained below.

The $\epsilon_{\text{single}}^{\text{eID}}$ is the fraction of signal loss due to track reconstruction and eID cuts within the detector active area.

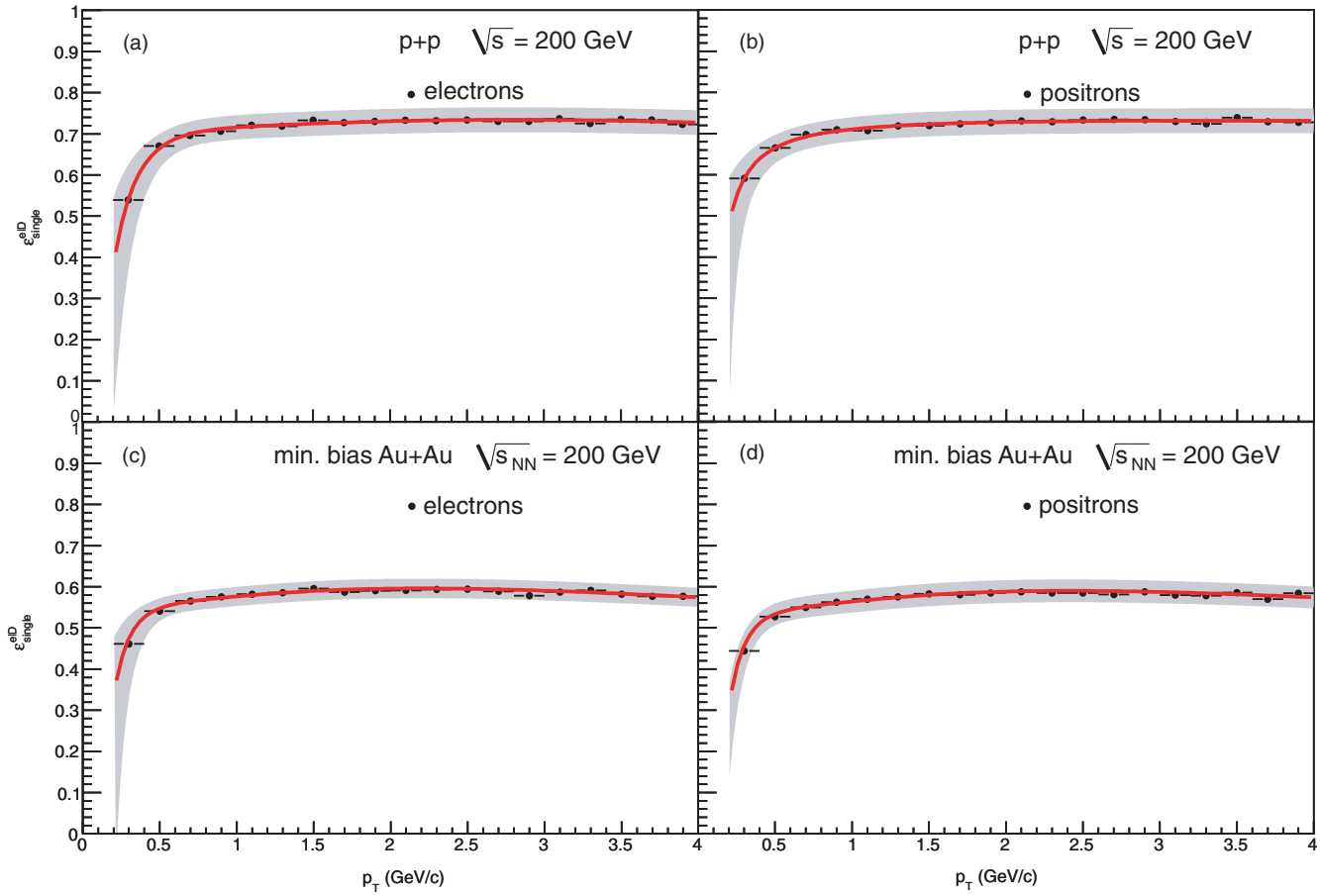

FIG. 17. (Color online) Single-electron (positron) efficiency as a function of p_T^e for electrons (left) and positrons (right) in $p+p$ (top) and Au+Au (bottom) collisions.

It depends only on the momentum of the track. The shape is very similar in $p+p$ and Au+Au, but the scale differs since different cut values are used. It is calculated as follows:

$$\epsilon^{\rm eID}_{\rm single}\left(p_T^e\right) = \frac{dN_e^{\rm out}/dp_T^e}{dN_e^{\rm in}/dp_T^e}. \tag{26}$$

The $dN_e^{\rm in}/dp_T^e$ is the p_T^e distribution of the input electron yield that falls into the *real* PHENIX acceptance, which includes the boundary described by Eq. (3) and the active areas of the detector. $dN_e^{\rm out}/dp_T^e$ is the p_T^e distribution of the output electron yield in the same acceptance after passing all the eID cuts.

The input distribution comes from a simulation of 450M π^0's flat in phase space ($0 < p_T < 25$ GeV/c, $|y| < 0.5$, and $0 < \phi < 2\pi$) with the branching ratio of the π^0 Dalitz decay set to 100% to enhance the sample of e^+e^- pairs per event. These events were processed by the full GEANT simulation program of the PHENIX detector [53] that includes the details of the detector response. The output simulation data files were processed by the event reconstruction chain of PHENIX. The Monte Carlo was tuned such that all the variables used for the electron identification described in subsection III C match the experimental ones for each data set ($p+p$ and Au+Au). Standard eID cuts are applied to the output. The reconstructed p_T^e of each output electron is weighted according to $p_T^{\rm in}$ with a realistic exponential p_T weight.

Figure 17 shows the single-electron (positron) efficiency as a function of p_T^e for $p+p$ and Au+Au. The different scales corresponding to the two data sets are due to more stringent cuts applied in the Au+Au data set. The band around the curve shows only the p_T^e dependence of the systematic uncertainty corresponding to a shift of ± 0.1 GeV/c of the efficiency curve. This in turns leads to a distortion of the e^+e^- mass shape shown by the band in Fig. 18. The total uncertainties on the pair reconstruction, including the range of applicability, are reported in subsection III K.

The $\epsilon^{\rm live}_{\rm single}$ is the fraction of signal loss due to inactive areas of the detector. The active areas of the detector are parameterized as a function of the particle momenta and azimuth using real data. There are small differences between $p+p$ and Au+Au.

In the EXODUS cocktail of hadron decays we have implemented the parametrization of the single-electron (positron) efficiency (shown as a curve in Fig. 17). The single-electron (positron) efficiency was applied as a weight to each track. The pair will therefore get a weight given by the product of the electron and the positron weight. This weight, a function of mass and pair-p_T, represents $\epsilon^{\rm eID}_{\rm pair}$. To calculate $\epsilon^{\rm live}_{\rm pair}$, a fiducial cut corresponding to the detector active areas is also

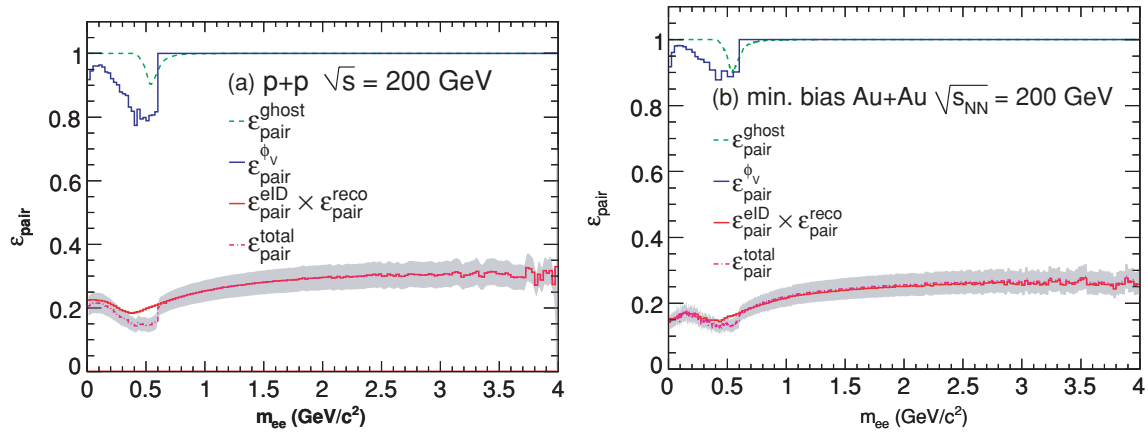

FIG. 18. (Color online) Different components of the total pair efficiency as a function of pair mass, obtained with the procedure described in the text for the $p+p$ and the Au+Au collisions.

implemented in EXODUS and a pair is rejected if at least one track falls out of the active areas. We therefore determine the product $\epsilon^{eID}_{pair} \times \epsilon^{live}_{pair}$ double differentially as a function of mass and pair-p_T.

Figure 18 shows $\epsilon^{eID}_{pair} \times \epsilon^{live}_{pair}$ as a function of mass. At high masses the efficiency is constant with a value nearly equal to the square of the single-electron efficiency. At low mass the pair efficiency results from the convolution of the single-electron reconstruction efficiency, which drops toward low momentum, and the geometric acceptance, which effectively truncates the single-electron p_T distribution ($p^e_T > 0.2$ GeV/c). For pairs with $0.4 \leqslant m_{ee} \leqslant 0.8$ GeV/c^2 the efficiency drops as a consequence of the drop at low p_T of the single-electron efficiency. However, for $m_{ee} \leqslant 0.4$ GeV/c^2, the lower limit on single-electron p_T results in a larger average momentum and the pair-efficiency consequently increases. The band around the $\epsilon^{eID}_{pair} \times \epsilon^{live}_{pair}$ curve in Fig. 18 again shows only the possible distortion of the mass distribution, due to the uncertainty shown in Fig. 17. It reaches a maximum of 8% around $m_{ee} = 0.4$ GeV/c^2.

The ϵ^{ghost}_{pair} represents the loss of real pairs which accidentally fulfill the detector overlap criteria. It is determined by the corresponding loss in mixed events as:

$$\epsilon^{ghost}_{pair} = \frac{dB1^2_{ee}/(dm_{ee}dp_T)}{dB2^2_{ee}/(dm_{ee}dp_T)}, \tag{27}$$

where $dB1$ ($dB2$) are the mixed-event unlike-sign pair (mass, p_T) distribution with (without) applying the overlap pair cuts.

The $\epsilon^{\phi_V}_{pair}$ represents the loss of real pairs that are accidentally oriented like conversion pairs in the magnetic field. At low masses it is calculated using the π^0 GEANT simulations described above. Above the pion mass, we use our hadron decay generator EXODUS where we have implemented an empirical smearing for the detector resolution in the determination of the magnitude and direction of the momentum vector.

Figure 19 shows the total pair efficiency as a function of invariant mass for different ranges of pair-p_T for Au+Au collisions.

The systematic uncertainty on $\epsilon^{eID}_{pair} \times \epsilon^{live}_{pair}$ is given by twice the uncertainty on the single-particle efficiency, determined by varying the cut values. In addition, uncertainties in the active areas have been determined by varying the active areas in the simulations.

The systematic uncertainties depend somewhat on p_T and mass; they are largest at low p_T and low mass where they reach 14.4% for $p+p$ and 13.4% for Au+Au. We use these errors as an estimate for all momenta and masses. Since the pair efficiency was derived using realistic kinematics, the uncertainty arises mostly from low-p_T tracks and neglecting the mass and pair-p_T dependence is a conservative approach.

The ϵ^{ghost}_{pair} and $\epsilon^{\phi_V}_{pair}$ affect only the LMR. Therefore, the corresponding systematic uncertainties have been independently evaluated by varying the cut values. We estimate an uncertainty of 5% due to the ghost cut and 6% due to the photon conversion cut on the final e^+e^- yield and we apply it to the LMR by varying the cut value in a suitable range.

The (mass, p_T) distributions from every individual centrality bin has been corrected using the same 2D efficiency correction function calculated for Min.Bias. This procedure

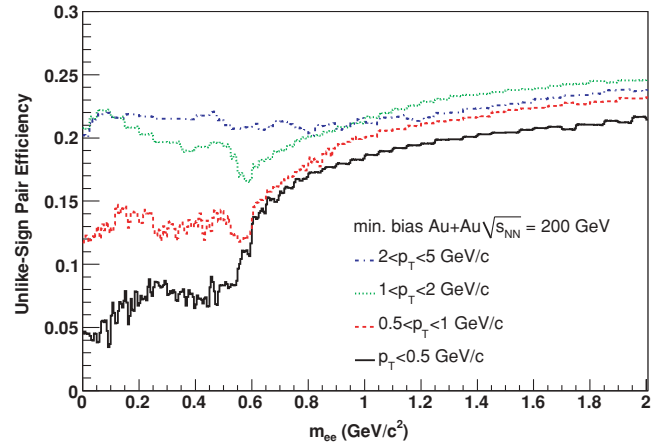

FIG. 19. (Color online) $\epsilon^{eID}_{pair} \times \epsilon^{live}_{pair}$ as a function of invariant mass for different ranges of pair-p_T for Au+Au data set.

avoids an assumption for the input kinematic distribution. However, since the individual centrality bins have limited statistics compared to the Min.Bias sample, this procedure may suffer statistical fluctuations. Alternatively we use an effective efficiency correction, as a function of mass only, obtained by weighting the two-dimensional (mass, p_T) corrections with a realistic p_T distribution provided by the minimum bias data set. This curve is given by the product of all the curves shown in Fig. 18. We take the difference of 10% between the 1D and the 2D corrected result as an additional systematic uncertainty for the efficiency correction of the different centrality data sets (see subsection V C).

We verified this efficiency using a GEANT simulation of 1 million e^+e^- pairs. Roughly half were generated flat in mass (0–4 GeV/c^2), p_T (0–4 GeV/c), azimuthal angle (0–2π), and rapidity ($|y| < 0.5$). The other half were generated with a probability inversely proportional to p_T in order to enhance the statistics in the low-mass and low-p_T region, where the efficiency varies most. Only pairs with both an electron and a positron in the ideal acceptance [given by Eq. (3)] are processed by GEANT and reconstructed with the same analysis chain. The efficiency is determined double differentially in p_T and mass of the e^+e^- pair. This second method gives consistent results but is limited by MC statistics. It was used as a cross-check in the final analysis.

H. Acceptance correction

In addition to the efficiency corrections, the p_T spectra are also corrected for the detector geometric acceptance $\epsilon_{\rm pair}^{\rm geo}$ to give the e^+e^-–pair yield over the full azimuth in one unit of rapidity. $\epsilon_{\rm pair}^{\rm geo}$ accounts for the fraction of pairs produced in one unit of rapidity over the full azimuthal range that are lost because either one or both particles from the pair miss the PHENIX detector

$$\epsilon_{\rm pair}^{\rm geo} = \frac{\frac{d^2N_{ee}}{dp_T^{ee}dm_{ee}}(\text{in PHENIX acceptance})}{\frac{d^2N_{ee}}{dp_T^{ee}dm_{ee}}(|y_{ee}| < 0.5)} \tag{28}$$

$\epsilon_{\rm pair}^{\rm geo}$ has been calculated using a Monte Carlo simulation of Dalitz decays of pseudoscalar mesons (π^0, η, η') and direct decays of vector mesons (ρ, ω, ϕ, J/ψ, ψ'). For all mesons the rapidity distribution is assumed to be flat around midrapidity. This assumption is well justified as PHENIX measures in $|y_{ee}| < 0.35$, where the natural distribution is flat. The acceptance is therefore uniform in $|y_{ee}| < 0.35$ and we do not assign a systematic uncertainty to it. The p_T distributions are taken from PHENIX measurements (see Sec. IV), and meson polarizations are taken from Ref. [54]. The acceptance correction is performed double differentially in pair-mass and p_T with 0.005 GeV/c^2 bins in mass and 0.1 GeV/c bins in p_T.

The systematic uncertainty due to the p_T parametrization and the polarization of the Dalitz pairs is studied with a simulation of unpolarized pairs with a flat distribution in mass and pair-p_T. In Fig. 20 we compare the acceptance for the full hadronic cocktail and the simulation of unpolarized pairs as a function of pair-p_T in 0.1 GeV/c^2 wide mass bins. The cocktail consists of the sum of polarized Dalitz decays and unpolarized vector mesons, while the flat simulations are always unpolarized. The shape of the acceptance is very similar, and the relative normalization agrees within 5% in the lowest mass bins and better for higher bins. Based on this comparison, illustrated by the ratio in the bottom figure, we assign an upper limit of 10% (marked by the lines in the figure) for the systematic uncertainty of $\epsilon_{\rm pair}^{\rm geo}$.

Since it arises from the independent fragmentation of two charm quarks, the contribution of charmed meson decays has a different acceptance. This component has been simulated with PYTHIA [55] and normalized according to the cross section measured in Ref. [48] scaled by $N_{\rm coll}$. However, due to the observed modifications of charm quarks in the medium [6], the acceptance could potentially differ from what is simulated by PYTHIA. For $m_{ee} < 0.5$ GeV/c^2 the charm contribution is negligible. For $0.5 < m_{ee} < 1$ GeV/c^2 a systematic uncertainty of 5% due to the uncertainty of the charm cross section ($\sigma_{c\bar{c}} = N_{\rm coll} \times 567 \pm 57^{\rm stat} \pm 224^{\rm syst}$ μb [6,48]) has been added in quadrature to the other systematic uncertainties on $\epsilon_{\rm pair}^{\rm geo}$.

I. Trigger efficiency ($p+p$)

The efficiency of the ERT trigger ($\epsilon_{\rm pair}^{\rm ERT}$) in $p+p$ collisions, as a function of pair mass and p_T, is determined with a fast Monte Carlo simulation of pairs which uses a parametrization of the single-electron ERT efficiency $\epsilon_{\rm single}^{\rm ERT}$. The single-electron ERT efficiency is determined using the Min.Bias data set. The online level-1 trigger decision is recorded in the Min.Bias data set even though it is not used to select the event. We require that the trigger tile that fires the ERT trigger is used by the electron candidate selected by the offline analysis. The ratio of triggered electrons relative to all electrons candidates gives the trigger efficiency as function of the single-electron p_T and is shown in Fig. 21. The trigger efficiency at the plateau is ≈60%, consistent with the fraction of the active trigger tiles. The trigger part and the offline part of the RICH and EMCal read-out are handled in separate electronics chains, and the trigger part has more noisy tiles that are masked out. This results in less active areas in the trigger. The efficiency is fit to the sum of two Fermi functions

$$f(p_T) = \frac{\epsilon_0 \cdot \theta(p_T - 0.5)}{e^{-(p_T - p_0)/k} + 1} + \frac{\epsilon_0' \cdot \theta(p_T + 0.5)}{e^{-(p_T - p_0')/k'} + 1}, \tag{29}$$

where ϵ_0 (ϵ_0'), p_0 (p_0'), and k (k') are free fit parameters and θ is the usual Heaviside θ function.

This parametrization of the single-electron trigger efficiency is implemented in a fast Monte Carlo simulation of hadron decays into e^+e^-. Each electron fires the trigger with a probability given by the trigger efficiency. We require that both electrons are within the PHENIX acceptance and at least one of them fires the trigger. The mass and p_T distribution of those pairs is compared to the one obtained with no trigger requirement. The ratio is the pair trigger efficiency and is shown in Fig. 22 as a function of e^+e^- invariant mass. The structures in Fig. 22 result from the turn-on curve of

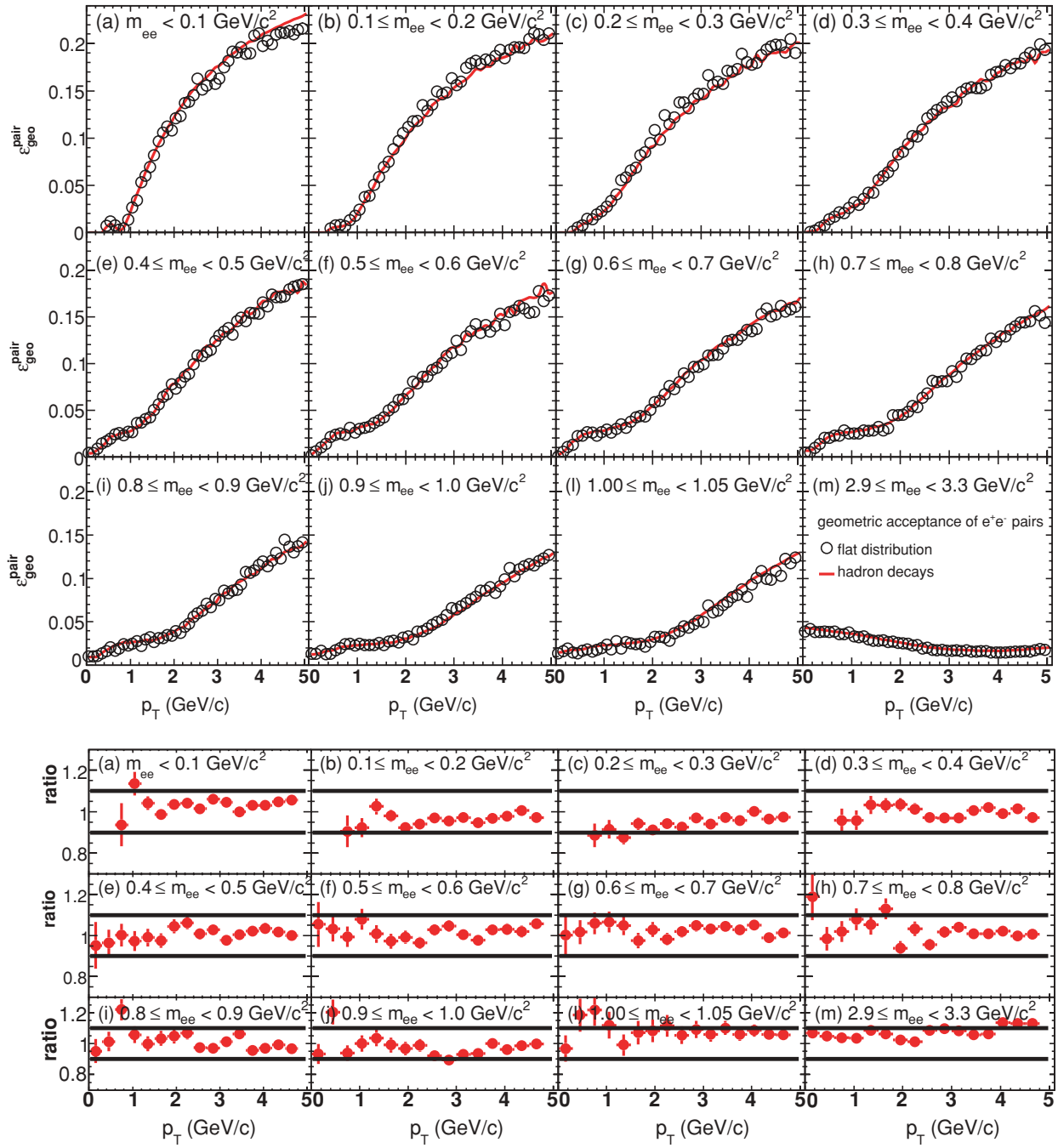

FIG. 20. (Color online) e^+e^--pair acceptance as a function of pair-p_T for different mass ranges for the hadronic cocktail (line) and a flat distribution of e^+e^- pairs (empty circles) and ratio of the two (bottom figure). The lines mark the limits of the systematic uncertainty.

the trigger threshold convoluted with the acceptance of the detector.

The systematic uncertainty has been studied by varying the parametrization of the single-electron ERT efficiency, as well as varying the eID cuts that define the reference sample. The effect of changing the eID cuts leads to a larger uncertainty at low p_T and low masses. We therefore assign a systematic uncertainty of 20% for $m_T < 1$ GeV$/c^2$ and 5% elsewhere. Finally, the systematic uncertainty includes potential shape distortion to the efficiency correction due to the variation of active trigger tiles during the data collection.

Figure 23 compares the invariant mass spectra for the $p+p$ data obtained with the Min.Bias and the ERT data sets. The ERT data set has been corrected by ERT trigger efficiency $\epsilon_{\text{pair}}^{\text{ERT}}$ and the total pair reconstruction efficiency $\epsilon_{\text{pair}}^{\text{total}}$, while the Min.Bias is corrected only for the $\epsilon_{\text{pair}}^{\text{total}}$. This comparison of the two data sets confirms that the Min.Bias and the ERT agree within their respective statistical errors.

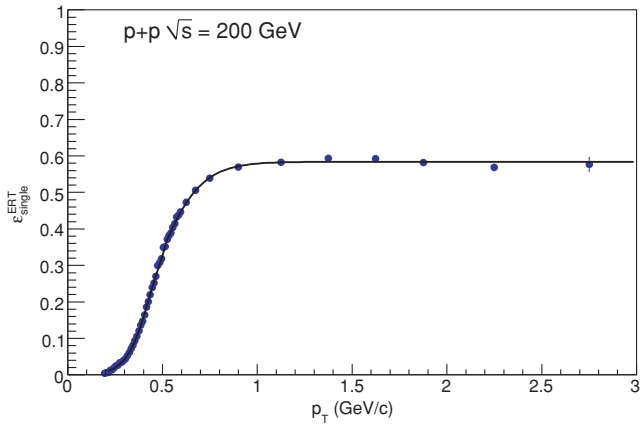

FIG. 21. (Color online) Trigger efficiency for single electrons ϵ^{ERT}_{single} as a function of p_T of the ERT trigger in $p+p$ collisions determined from the Min.Bias data set.

J. Occupancy correction (Au+Au)

In Au+Au collisions there is an additional efficiency loss of particle detection due to the presence of other particles nearby. To study this effect single electrons and positrons are simulated through the GEANT simulator of PHENIX and then embedded into data files containing detector hits from real Au+Au events. Next, these new files containing the embedded $e^{\pm}$ are run through the entire reconstruction software. As the particle density reduces the efficiency but does not introduce additional p_T dependence, the occupancy correction can be factored out. Since all the detectors used in the analysis are located after the pair has been opened by the magnetic field, the pair embedding efficiency in each centrality bin is defined as the square of the single-electron embedding efficiency

$$\epsilon^{occ}_{pair} = \left(\epsilon^{occ}_{single}\right)^2 = \left(\frac{\#\text{ reconstructed } e^{\pm} \text{ from embedded data}}{\#\text{ reconstructed } e^{\pm} \text{ from single track data}}\right)^2,$$

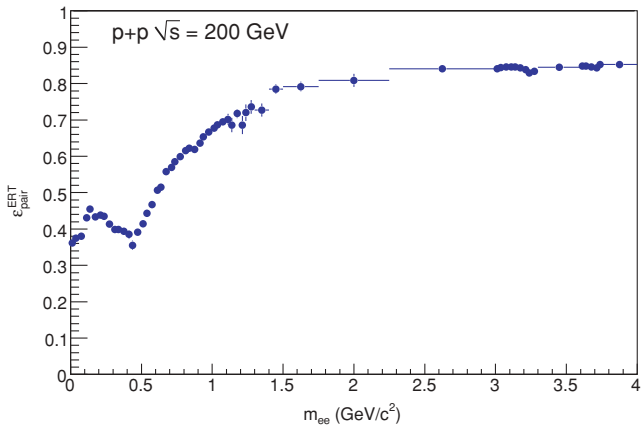

FIG. 22. (Color online) Trigger efficiency ϵ^{ERT}_{pair} for e^+e^- pairs as a function of e^+e^--pair invariant mass.

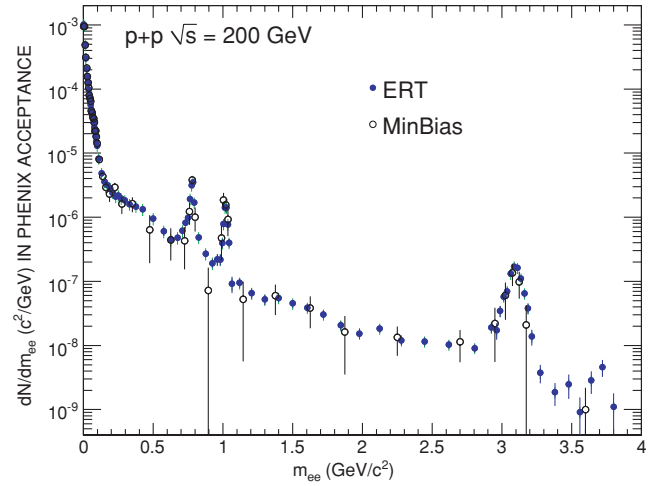

FIG. 23. (Color online) Invariant mass spectra for $p+p$ data with the Min.Bias (hollow) and ERT (solid) data sets. The agreement between the two data sets is excellent.

where a reconstructed particle from embedded data is required to have most of its detector hits associated with hits from the simulated particle.

Table V displays the embedding efficiencies for the centrality classes used in the analysis. For the minimum bias results we have weighted the occupancy correction by the fraction of pairs in each centrality class. Since most of the yield is concentrated in the most central classes, the resulting pair efficiency is 0.81 instead of the square of the minimum bias value $0.96^2 = 0.92$.

A second, data-driven method was developed to determine ϵ^{occ}_{pair}. This method uses the conversion pairs created at the beam pipe to select a track sample of pure e^+ or e^- from real data. The conversion pairs originating at the beam pipe result in a clear invariant mass peak around $m_{ee} \sim 20\,\text{MeV}/c^2$ (see Fig. 6). We assign tight eID cuts to only one track of a pair and measure the efficiency of the other track of the same pair without any eID cut applied. Differences between the two methods are accounted for in a 3% systematic uncertainty [56].

K. Systematic uncertainty

The systematic uncertainties are summarized in Table VI. The uncertainties in Table VI are categorized by type:

(i) A: point-to-point uncertainty uncorrelated between mass or p_T bins;

TABLE V. Embedding efficiency for different centrality classes of Au+Au collisions.

Centrality	ϵ^{occ}_{single}	ϵ^{occ}_{pair}
0–10%	0.86	0.74
10–20%	0.91	0.83
20–40%	0.93	0.87
40–60%	0.97	0.95
60–92%	0.99	0.98

TABLE VI. Systematic uncertainties on the dilepton yield and mass range of applicability.

Syst. err. component	$p+p$	Au+Au	Mass range	Type
Pair reconstruction	14.4%	13.4%	0–4 GeV/c^2	B
Conversion rejection	6%	6%	0–0.6 GeV/c^2	B
Pair cuts	5%	5%	0.4–0.6 GeV/c^2	B
Occupancy efficiency	–	3%	0–4 GeV/c^2	C
BBC and trigger bias	11.3%	–	0–4 GeV/c^2	C
ERT efficiency	5% (20% for $m_T < 1$ GeV/c^2)	–	0–4 GeV/c^2	B
Combinatorial background	$3\% \times B/S$	$0.25\% \cdot B/S$	0–4 GeV/c^2	B
Correlated background	Mass-dependent (Fig. 15)	Mass-dependent (Fig. 15)	0–4 GeV/c^2	B
Centrality	–	10%	0–4 GeV/c^2	B
Acceptance correction	10%	10%	0–4 GeV/c^2	B
Charm acceptance	5%	5%	>0.5 GeV/c^2	B

(ii) B: correlated uncertainty, all points move in the same direction but not by the same factor;
(iii) C: an overall normalization uncertainty in which all points move by the same factor independent of mass or p_T.

The uncertainty on pair reconstruction efficiency includes eID cuts, geometric acceptance, and run-by-run fluctuations. The uncertainty due to the conversion rejection cut and the overlap cuts as well as the uncertainty due to the ERT and minimum bias trigger efficiency (for $p+p$) and occupancy (for Au+Au) are also listed. These uncertainties are included in the final systematic uncertainty on the invariant e^+e^- pair yield. The uncertainties deriving from reconstruction and occupancy do not have a strong p_T dependence, so we keep the assigned values for every p_T bin. The pair cuts and the conversion rejection are localized in mass ($m < 0.6$ GeV/c^2) and are rather p_T independent. The uncertainty on the combinatorial background is the largest contribution to the systematic uncertainty in Au+Au and the value is estimated to be $0.25\% \times B/S$. S/B rises with p_T, therefore the uncertainty on the combinatorial background has been propagated separately for each p_T bin. The uncertainty on the correlated background is approximately 2–3% in $p+p$ and 10% in Au+Au for $m_{ee} < 0.6$ GeV/c^2 and p_T independent. However it increases in $p+p$ toward high masses. In the $p+p$ data the uncertainty on the ERT trigger efficiency, as well as on the BBC and trigger bias is included. For individual centrality bins, we add 10% uncertainty arising from the p_T dependence of the efficiency correction: this was obtained from the difference between the 1D-corrected mass spectra and the 2D-corrected mass spectra. For the p_T spectra, which are further corrected by the geometric acceptance, we added 10% uncertainty from the acceptance correction and 5% for $m_{ee} > 0.5$ GeV/c^2 due to the charm contribution. Most of these uncertainties are mass-p_T correlated, i.e., all points move in the same direction but not by the same factor. Only the BBC and trigger bias (in $p+p$) and the occupancy (in Au+Au) are normalization uncertainties in which all points move by the same factor independent of mass and p_T. Since those uncertainties are small compared to the total uncertainty, they are included in the total uncertainty, without plotting it separately.

IV. COCKTAIL OF HADRONIC SOURCES

In this section we describe the methods used to calculate the pair yield expected from hadronic decays which will be compared to the experimental data. We model the e^+e^- pair contributions from hadron decays using the decay generator EXODUS. EXODUS is a phenomenological event generator that allows us to simulate the phase-space distribution of all relevant sources of electrons and electron pairs and the decay of these sources. Moreover, it allows us to include the filtering for the geometrical acceptance and the detector resolution. The relevant primary mesons that involve electrons in the final state are π^0, η, η', ρ, ω, ϕ, J/ψ, and ψ'.

We assume that all hadrons have a constant rapidity density in the range $|\Delta\eta| \leqslant 0.35$ and a uniform distribution in azimuthal angle. Transverse-momentum distributions are largely based on measurements in PHENIX. The key input is the rapidity density dN/dy of neutral pions, which we determine from a fit to PHENIX data on charged and neutral pions [57–60] with a modified Hagedorn function, given by:

$$E\frac{d^3\sigma}{dp^3} = A\left(e^{-(ap_T+bp_T^2)} + p_T/p_0\right)^{-n}. \quad (30)$$

Fit parameters and dN/dy for $p+p$ and Au+Au are given in Table VII.

For all other mesons we assume m_T scaling, replacing p_T by $\sqrt{m^2 - m_\pi^2 + (p_T/c)^2}$, where m is the mass of the meson and we fit a normalization factor to PHENIX data [57–68], where available. Figure 24 shows the excellent agreement

TABLE VII. Fit parameters from the modified Hagedorn function [Eq. (30)] for $p+p$ and Au+Au pion spectra (π^0 and $\pi^\pm$) and the corresponding rapidity density dN/dy.

Parameter	$p+p$	Au+Au
dN/dy	1.06 ± 0.11	95.7 ± 6.9
A (mb GeV$^{-2}c^3$)	377 ± 60	504.5 ± 10
a [(GeV/c)$^{-1}$]	0.356 ± 0.014	0.52 ± 0.007
b [(GeV/c)$^{-2}$]	0.068 ± 0.019	0.16 ± 0.010
p_0(GeV/c)	0.7 ± 0.02	0.7 ± 0.005
n	8.25 ± 0.04	8.27 ± 0.02

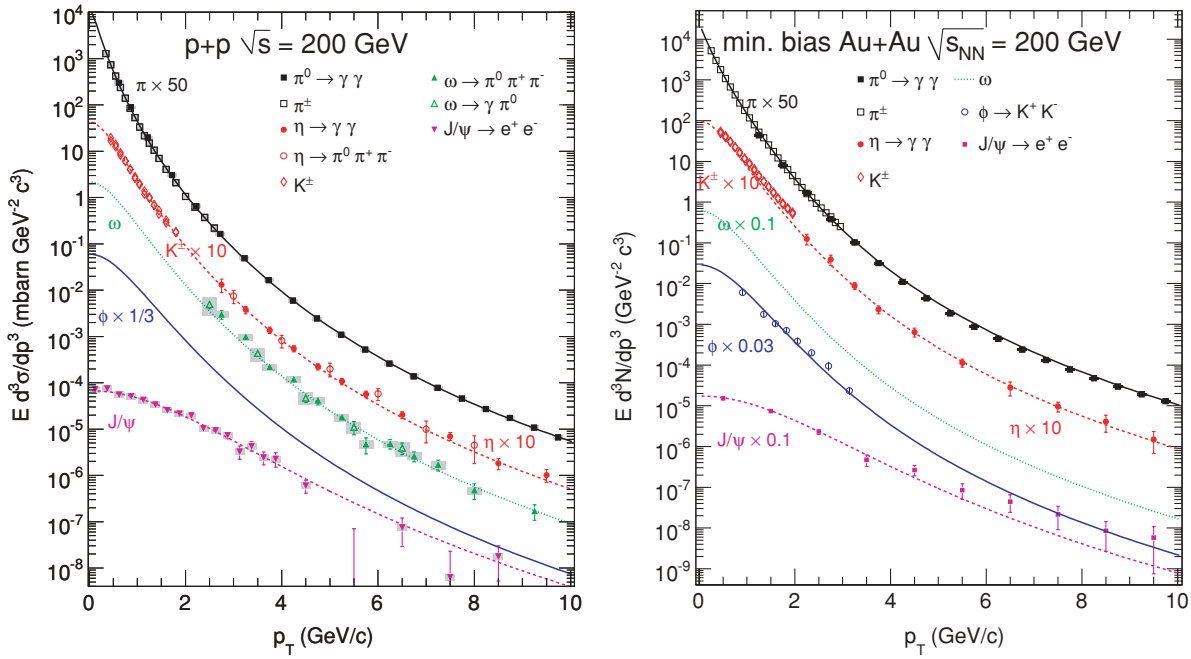

FIG. 24. (Color online) Compilation of meson production cross sections in $p+p$ (left) and Au+Au (right) collisions at $\sqrt{s_{NN}} = 200$ GeV. Shown for $p+p$ are data for neutral [57] and charged pions [58], η [61], kaons [58], ω [62], ϕ [63], and J/ψ [64]. Shown for Au+Au are data for neutral [59] and charged pions [60], η [61], kaons [60], ω, ϕ [65], and J/ψ [66]. The data are compared to the parametrization based on m_T scaling used in our hadron decay generator.

with published PHENIX data. The η meson is measured only at higher p_T; however, in the $p+p$ collisions the fit is in good agreement with the p_T distribution of kaons, which have similar mass (see discussion below).

In order to extract the meson yield we integrate the fits over all p_T. Results, systematic uncertainties, and references to data are given in Table VIII and the ratio of the integrated yields meson/π^0 are compared for $p+p$ and Au+Au data. For the ρ meson we assume $\sigma_\rho/\sigma_\omega = 1.15 \pm 0.15$, consistent with values found in jet fragmentation [54]. The η' yield is scaled to be consistent with jet fragmentation $\sigma_{\eta'}/\sigma_\eta = 0.15 \pm 0.15$ [54]. The ψ' is adjusted to be $\sigma_{\psi'}/\sigma_{J/\psi} = 0.14 \pm 0.03$ [69] in agreement with PHENIX measurements [70].

TABLE VIII. Hadron rapidity densities used in our hadron decay generator. For the ω and ϕ, data from this analysis were used together with data from the quoted references.

	$\frac{dN}{dy}\|_{y=0}$	Relative uncertainty	Meson/π^0	Data used
		$p+p$		
π^0	1.065 ± 0.11	10%	1.0	PHENIX [57], [58]
η	$(1.1 \pm 0.3) \times 10^{-1}$	30%	1.032×10^{-1}	PHENIX [61]
ρ	$(8.9 \pm 2.5) \times 10^{-2}$	28%	8.34×10^{-2}	Jet fragmentation [54]
ω	$(7.8 \pm 1.8) \times 10^{-2}$	23%	7.32×10^{-2}	PHENIX [62]
ϕ	$(9.0 \pm 2.0) \times 10^{-3}$	24%	8.4×10^{-3}	PHENIX [63]
η'	$(1.3 \pm 0.5) \times 10^{-2}$	40%	1.27×10^{-2}	PHENIX [67]
J/ψ	$(1.77 \pm 0.27) \times 10^{-5}$	15%	1.66×10^{-5}	PHENIX [64]
ψ'	$(2.5 \pm 0.7) \times 10^{-6}$	27%	2.3×10^{-6}	PHENIX [69], [70]
		Au+Au		
π^0	$(9.572 \pm 0.95) \times 10$	10%	1.0	PHENIX [59], [60]
η	$(1.077 \pm 0.32) \times 10$	30%	1.12×10^{-1}	PHENIX [61]
ω	8.60 ± 2.8	33%	8.98×10^{-2}	PHENIX [68]
ρ	9.88 ± 3.0	30%	1.03×10^{-1}	Jet fragmentation [54]
ϕ	2.05 ± 0.6	30%	2.14×10^{-2}	PHENIX [65]
η'	2.05 ± 0.2	100%	2.15×10^{-2}	PHENIX [67] and [54]
J/ψ	$(1.79 \pm 0.26) \times 10^{-3}$	15%	1.82×10^{-5}	PHENIX [66]
ψ'	$(2.6 \pm 0.7) \times 10^{-4}$	27%	2.70×10^{-6}	PHENIX [69] and [70]

For the η, ω, ϕ, and J/ψ, and also η', and ψ' (in $p+p$) the quoted uncertainties include those on the data as well as those using different shapes of the p_T distributions to extrapolate to zero p_T. Specifically we have fit the functional form given in Eq. (30) with all parameters free and also with an exponential distribution in m_T. For the ρ, which is not measured in $p+p$ nor in Au+Au, and η' and ψ', which are not measured in Au+Au, the uncertainty in the table represent the quadrature sum of the uncertainty of the cross section and the uncertainty relative to other mesons.

All the mesons shown in Fig. 24 can be described by the m_T-scaling parametrization of the pion spectrum. The fact that the η's and the kaons follow the same m_T-scaling prediction over all p_T appears to be due to the fact that the masses of the particles are almost the same. In Au+Au, however, η and kaons do not follow the same m_T-scaling prediction. At high p_T, where we measure η's, we see that they are suppressed as much as pions and the trend of $R_{\rm AA}$ for these two mesons looks identical. However, we have observed a different trend (i.e., a smaller suppression) for strange particles and η has a strangeness content too [71,72]. Therefore, since the η cannot be measured at low p_T, we take as systematic uncertainty in the low-p_T region (and consequently on the extrapolated dN/dy), the difference of the two spectra ($\sim$30%) in the low-p_T range. We note that this is a conservative estimate of the systematic uncertainty. Statistical models that reproduce well the particle spectra and ratios measured at RHIC [13,73] calculate a dN/dy for the η which is well within the assigned systematic uncertainty. At high p_T we assign a smaller systematic uncertainty of 7% (17%) for $p+p$ (Au+Au) collisions arising from the asymptotic value of the η/π^0 ratio of 0.48 $\pm$ 0.03 (0.08) based on PHENIX measurement [61].

Once the meson yields and p_T spectra are known the dilepton spectrum is given by decay kinematics and branching ratios, which are implemented in our decay generator EXODUS following earlier work published in Ref. [48]. The branching ratios are taken from the compilation of particle properties in Ref. [54]. For the Dalitz decays π^0, η, $\eta' \to e^+e^-\gamma$ and the decay $\omega \to e^+e^-\pi^0$ we use the Kroll-Wada expression [74] with electromagnetic transition form factors measured by the Lepton-G Collaboration [75,76]. For the decays of the vector mesons ρ, ω, $\phi \to e^+e^-$ we use the expression derived by Gounaris and Sakurai [77], extending it to 2 GeV/c^2, slightly beyond its validity range. For the J/ψ and $\psi' \to e^+e^-$ we use the same expression discussed in Ref. [64] modified to include radiative corrections. All vector mesons are assumed to be unpolarized. For the Dalitz decays, where the third body is a photon, the angular distribution is sampled according to $1+\cos^2\theta_{\rm CS}$, where $\theta_{\rm CS}$ is the polar angle of the electrons in the Collins-Soper frame.

The resulting systematic uncertainties on the mass spectrum depend on mass and range from 10 to 30%. They result primarily from the uncertainty on the measured pion yield and on the meson-to-pion ratios. The uncertainty from the measured electromagnetic transition form factors, in particular for the $\omega \to e^+e^-\pi^0$ decay, is also included but contributes significantly only in the range around 0.5 to 0.6 GeV/c^2. The uncertainty from polarization is negligible but also included.

V. RESULTS

This section presents the results for the $p+p$ and the Au+Au analyses. The $p+p$ data provide a good baseline for understanding the results of the Au+Au analysis presented in this section. This section is organized as follows. Each subsection concentrates on a different region of the (m_{ee}, p_T) phase space. For each region we will present the results for the $p+p$ and for the Au+Au data. In subsection V A we will show the inclusive mass spectrum for $p+p$ and minimum bias Au+Au collisions and we will compare it with the cocktail. In subsection V B we discuss the results in the IMR by comparing the data with the charm expectations from ($N_{\rm coll}$-scaled) PYTHIA [55]. In subsection V C we present the yields in the LMR and discuss their centrality dependence. Subsection V D discusses the p_T dependence of the mass spectra. Part of the LMR, denoted with LMR I, where the p_T of the e^+e^- pair is much larger than its mass, is the region of quasireal virtual photons: we present the results in this region for $p+p$ and Au+Au data in subsection V E. Subsection V F discusses what we can learn from the measurement of direct photons (in LMR I) about the yields in the p_T-inclusive LMR. Finally subsection V G presents the p_T spectra for different mass bins for $p+p$ and Min.Bias Au+Au data and compares them with the expectations from cocktail plus charm plus direct photons.

A. p_T-inclusive mass spectra

Figure 25 compares the yield of e^+e^- pairs in the PHENIX acceptance in $p+p$ data to the expected yield from the contributions of the cocktail and shows the various sources of the cocktail (hadron decays, charm, bottom, and Drell-Yan pairs). The $p+p$ data are very well described by the expectation from the hadronic cocktail and heavy flavor decays for the entire mass range within the uncertainty of the data and the cocktail.

Figure 26 compares the e^+e^- yield in the PHENIX acceptance in minimum bias Au+Au collisions to the expected yield from the contributions of various sources. The cocktail sources are the same as in the $p+p$ data but tuned separately to the Au+Au measurements. The data below the pion mass, where π^0 Dalitz decays dominate, are well described by the cocktail. The vector-meson yields in the cocktail are partly based on the e^+e^- pair data (see Sec. IV) and consequently agree well with the data. In particular the J/ψ yield in the cocktail is exclusively based on the e^+e^- measurement [66] (shown in Fig. 24 and therefore the data in Fig. 26 are expected to agree with the cocktail at the J/ψ peak. J/ψ suppression would be observed if the cocktail would instead use the $N_{\rm coll}$-scaled $p+p$ measurement [64]. In the IMR, besides the charm, bottom and Drell Yan calculated with PYTHIA [55], which are the same as in the $p+p$ data, scaled by $N_{\rm coll}$, there is another curve drawn for the charm. This will be described in subsection V B.

Figure 27 shows the mass spectra for $p+p$ (bottom), for minimum bias Au+Au (top), and for five different centrality classes in Au+Au. The data are compared to the sum of hadronic cocktail and charmed meson decays. The

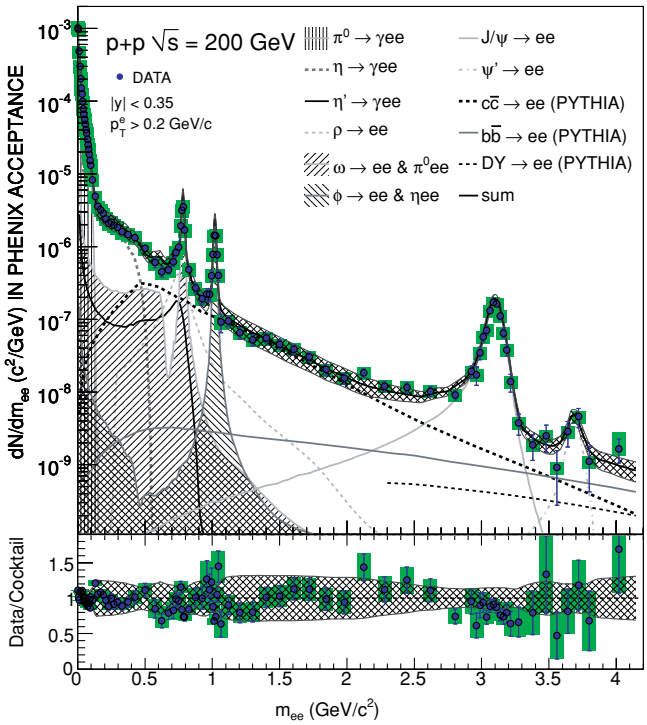

FIG. 25. (Color online) Inclusive mass spectrum of e^+e^- pairs in the PHENIX acceptance in $p+p$ collisions compared to the expectations from the decays of light hadrons and correlated decays of charm, bottom, and Drell-Yan. The contribution from hadron decays is independently normalized based on meson measurements in PHENIX. The bottom panel shows the ratio of data to the cocktail of known sources. The systematic uncertainties of the data are shown as boxes, while the uncertainty on the cocktail is shown as band around 1.

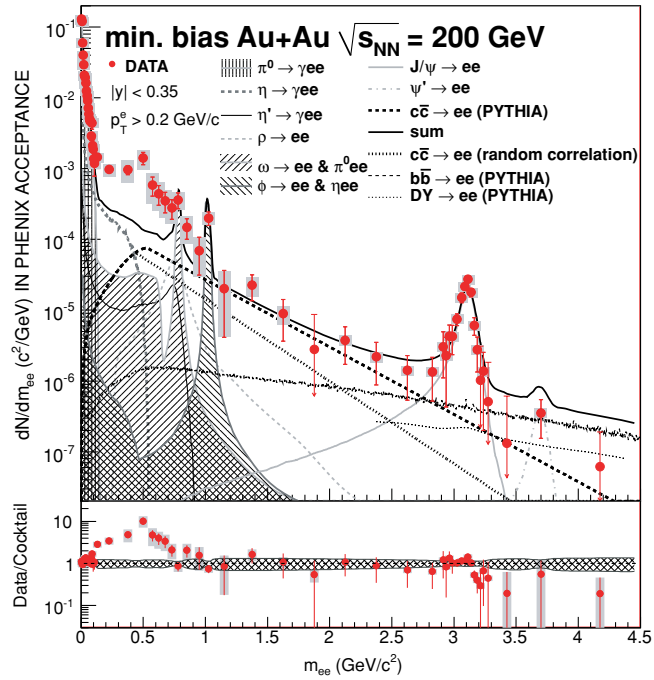

FIG. 26. (Color online) Inclusive mass spectrum of e^+e^- pairs in the PHENIX acceptance in minimum-bias Au+Au compared to expectations from the decays of light hadrons and correlated decays of charm, bottom, and Drell-Yan. The charm contribution expected if the dynamic correlation of c and $\bar{c}$ is removed is shown separately. Statistical (bars) and systematic (boxes) uncertainties are shown separately. The contribution from hadron decays is independently normalized based on meson measurements in PHENIX. The bottom panel shows the ratio of data to the cocktail of known sources. The systematic uncertainties of the data are shown as boxes, while the uncertainty on the cocktail is shown as band around 1.

charm cross section, measured in $p+p$, $\sigma_{c\bar{c}} = 567 \pm 57^{\text{stat}} \pm 224^{\text{syst}}$ μb [48], has been scaled by N_{coll} (given in Table I). For each centrality class, the data and the cocktail are absolutely normalized. Each data set is compared with two corresponding cocktail lines, shown in solid and dotted curves. The difference between the cocktails is due to uncertainty in the $c\bar{c}$ contribution (see discussion below).

Unlike the $p+p$ mass spectrum, the Au+Au mass spectra show enhancement above the cocktail, in particular for the LMR (0.15–0.75 GeV/c^2). There is little enhancement for peripheral (60–92%) data, but very strong enhancement for two most central classes (0–10% and 10–20%). The enhancement increases rapidly with increasing centrality.

In order to quantitatively describe this enhancement, more information is needed about other components that can potentially contribute to the LMR, namely the open heavy flavor and internal conversion of real direct photons. We discuss them in the next sections.

B. Open heavy flavor contribution

The dilepton yield in the IMR is dominated by semileptonic decays of charm hadrons correlated through flavor conservation. Small contributions also arise from bottom hadrons and Drell-Yan. For $p+p$ data we determine the heavy flavor contribution by subtracting the hadronic cocktail from the dilepton data. We integrate the subtracted yield in the IMR, extrapolate to zero e^+e^- pair mass to get the entire cross section, correct for geometric acceptance, and convert to a production cross section using known branching ratios of semileptonic decays [54]. Details of the analysis of the charm cross section are reported in [38].

We find a rapidity density of $c\bar{c}$ pairs at midrapidity:

$$\left.\frac{d\sigma_{c\bar{c}}}{dy}\right|_{y=0} = 118.1 \pm 8.4^{\text{stat}} \pm 30.7\text{syst} \pm 39.5^{\text{model}}\,\mu\text{b}.$$

This corresponds to a total charm cross section of $\sigma_{c\bar{c}} = 544 \pm 39^{\text{stat}} \pm 142^{\text{syst}} \pm 200^{\text{model}}\,\mu$b, consistent with previous measurement of single electrons by PHENIX ($\sigma_{c\bar{c}} = 567 \pm 57^{\text{stat}} \pm 224^{\text{syst}}$ μb) [48] and with a fixed-order-plus-next-to-leading-log (FONLL) pQCD calculation ($\sigma_{c\bar{c}} = 256^{+400}_{-146}\,\mu$b) [78].

In Au+Au the dynamic correlation of c and $\bar{c}$, which is essential to determine the mass spectral shape, could be modified compared to $p+p$ collisions. The observed suppression and the elliptic flow of nonphotonic electrons indicates that charm quarks interact with the medium [6], which should change the correlations between the produced $c\bar{c}$ pairs. We also note that the p_T distribution for electrons generated by PYTHIA [55] is softer than the spectrum measured

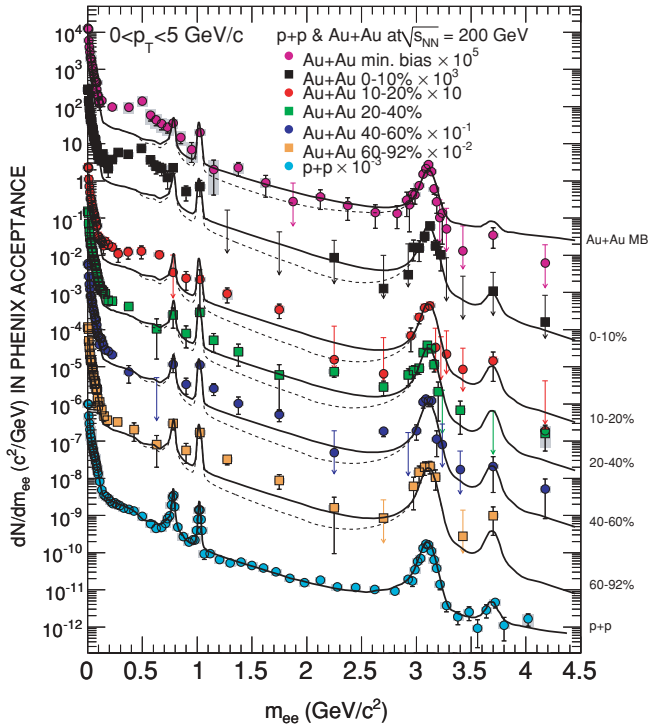

FIG. 27. (Color online) Invariant mass spectrum of e^+e^- pairs inclusive in p_T compared to expectations from the model of hadron decays for $p+p$ and for different Au+Au centrality classes. The charmed meson decay contribution based on PYTHIA [55] is included in the sum of sources (solid black line). The dotted line shows the contribution from charm calculated assuming an isotropic angular distribution. Statistical (bars) and systematic (boxes) uncertainties are shown separately. The systematic uncertainty on the expected hadronic sources is not shown: it ranges from ∼10% in the π^0 region to ∼30% in the region of the vector mesons. The uncertainty on the charm cross section, which dominates the IMR, is ∼30% in both $p+p$ and in Au+Au collisions.

in $p+p$ data but coincides with that observed in minimum bias Au+Au collisions. Thus we compare our Au+Au data to two extreme scenarios that bracket the charm contribution:

(i) The correlation is unchanged by the medium and equals what is known from $p+p$ collisions. In this case we can use the same PYTHIA calculation scaled to match the cross section measured in $p+p$ and scale it by the mean number of binary $N+N$ collisions (as given in Table I).

(ii) The $c\bar{c}$ dynamical correlation is washed out by medium interactions, i.e., the direction of c and $\bar{c}$ quarks are uncorrelated. We sample from the heavy flavor single-electron p_T spectra, choose the angle randomly and keep the overall cross section fixed to the experimental data [6]. Because the average opening angle of uncorrelated pairs is smaller than the one resulting from the back-to-back correlation predicted by PYTHIA, the mass spectral shape of uncorrelated pairs is much softer than the one calculated by PYTHIA.

The charm contribution determined by case (i) is shown as the upper dashed curve in Fig. 26 or the upper solid curves in Fig. 27. The charm contribution determined by case (ii) is shown as the dotted curve in Fig. 26 or the dashed curves in Fig. 27. In both cases the total yield of charm is normalized to the value measured by PHENIX.

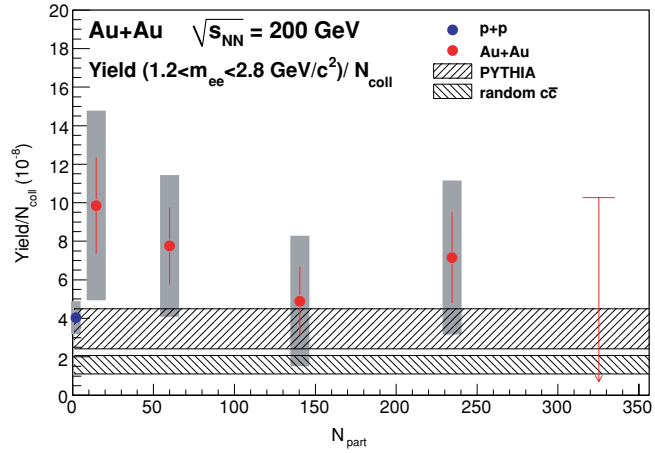

FIG. 28. (Color online) Dielectron yield per binary collision in the mass range 1.2 to 2.8 GeV/c^2 as a function of $N_{\rm part}$. Statistical and systematic uncertainties are shown separately. Also shown are two bands corresponding to different estimates of the contribution from charmed meson decays. The width of the bands reflects the uncertainty of the charm cross section only.

In the Min.Bias Au+Au data set, the IMR seems to be well described by the continuum calculation based on case (i). This is somewhat surprising, since single-electron distributions from charm show substantial medium modifications [6]. Thus, it is hard to understand how the dynamical correlation at production of the $c\bar{c}$ remains unaffected by the medium. Case (ii) leads to a much softer mass spectrum, as shown by the dotted curve in Fig. 26. This would leave significant room for other contributions, e.g., thermal radiation.

We have integrated the yield in the mass region 1.2 to 2.8 GeV/c^2 and normalized to the number of binary collisions $N_{\rm coll}$ (Fig. 28). The systematic uncertainty due to $N_{\rm coll}$ (as indicated in Table I) has been included in the overall systematic uncertainty. Within uncertainties $N_{\rm coll}$ scaling is observed for the production of nonphotonic electrons, i.e., for those electrons arising from decays of heavy-flavor hadrons [6]. The normalized yield shows no significant centrality dependence and is consistent within systematic uncertainties with the expectation based on $N_{\rm coll}$-scaled PYTHIA, with the cross-section measurement of Ref. [48] [case (i)]. However, the scaling with $N_{\rm coll}$ may be a mere coincidence resulting from two balancing effects: the energy loss of charm, which increases with $N_{\rm part}$, would lead to a softer mass distribution and therefore less yield in the IMR [case (ii)], while a thermal contribution could increase faster than linearly with $N_{\rm part}$, resulting in more yield in the IMR. Such a coincidence may have been observed at the SPS [35], where a prompt component has now been suggested by NA60 [36].

C. Low-mass excess in Au+Au data

Figure 27 shows that the low-mass enhancement is concentrated in the first two centrality classes, i.e., 0–10% and

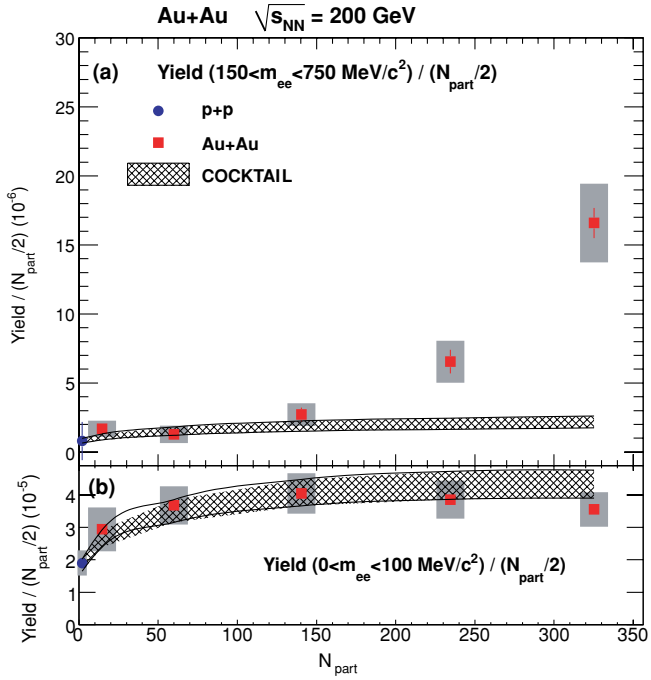

FIG. 29. (Color online) Dielectron yield per participating nucleon pair ($N_{\rm part}/2$) as function of $N_{\rm part}$ for two different mass ranges (a: $0.15 < m_{ee} < 0.75$ GeV/c^2, b: $0 < m_{ee} < 0.1$ GeV/c^2) compared to the expected yield from the hadron decay model. The two lines give the systematic uncertainty of the yield from cocktail and charmed hadron decays. For the data statistical and systematic uncertainties are shown separately.

10–20%. For more peripheral collisions the enhancement diminishes. Only some small excess is visible for 20–40% and 60–92% while no deviation is observed in 40–60% with respect to the cocktail beyond systematic uncertainties.

To quantify the centrality dependence of the enhancement, we have integrated the yield in two mass windows: below 0.1 GeV/c^2 and 0.15 to 0.75 GeV/c^2. Since the cocktail yield in these regions arises mostly from hadrons (more than 90% from π^0 below 0.1 GeV/c^2 and more than 99% from the sum of light hadrons in $0.15 < m_{ee} < 0.75$ GeV/c^2) we compare the measured yield to the rate of pion production. Pions were found to scale approximately with $N_{\rm part}$ [79], therefore we compare the measured yield in data to $N_{\rm part}$.

The top panel of Fig. 29 shows the centrality dependence of the yield in the mass region 0.15–0.75 GeV/c^2 divided by the number of participating nucleon pairs ($N_{\rm part}/2$). The systematic uncertainty due to $N_{\rm part}$ (as indicated in Table I) has been included in the overall systematic uncertainty. For comparison the yield below 0.1 GeV/c^2, which is dominated by low-p_T pion decays, is shown in the lower panel.

For both mass intervals the yield is compared to the yield calculated from the hadron cocktail. Two solid curves on each panel show the upper and lower limit of the expected yield from the cocktail. The cocktail uncertainty includes the uncertainty in the charm contribution discussed in the previous section. In the lower mass range the yield agrees with expectations and is proportional to the pion yield (bottom panel of Fig. 29). In contrast, in the range from 0.15 to 0.75 GeV/c^2 the observed yield rises significantly above expectations.

TABLE IX. The enhancement factor, defined as the ratio between the measured yield and the expected yield for $0.15 < m_{ee} < 0.75$ GeV/c^2, for different centrality bins. The meaning of the errors is defined in the text.

Centrality	Enhancement ($\pm$stat $\pm$syst $\pm$model)
00–10%	$7.6 \pm 0.5 \pm 1.3 \pm 1.5$
10–20%	$3.2 \pm 0.4 \pm 0.7 \pm 0.6$
20–40%	$1.4 \pm 0.3 \pm 0.4 \pm 0.3$
40–60%	$0.8 \pm 0.3 \pm 0.4 \pm 0.2$
60–92%	$1.5 \pm 0.3 \pm 0.5 \pm 0.3$
Min.Bias	$4.7 \pm 0.4 \pm 1.5 \pm 0.9$

The enhancement factor, defined as the ratio between the measured yield and the expected yield for $0.15 < m_{ee} < 0.75$ GeV/c^2, is $4.7 \pm 0.4^{\rm stat} \pm 1.5^{\rm syst} \pm 0.9^{\rm model}$ for Min.Bias data. The first error is the statistical error, the second the systematic uncertainty of the data, and the last error is an estimate of the uncertainty in the cocktail, i.e., the expected yield from hadronic sources. For the various centrality bins the enhancement factor is reported in Table IX.

The increase is qualitatively consistent with the conjecture that an in-medium enhancement of the dielectron continuum yield arises from scattering processes like $\pi\pi$ or $q\bar{q}$ annihilation. In this case the enhancement would scale proportional to $N_{\rm part}^2$, differing from the hadronic cocktail that scales proportional to $N_{\rm part}$.

D. p_T dependence of the mass spectra

Figure 30 compares e^+e^- invariant mass spectra measured in $p+p$ and in Min.Bias Au+Au collisions to the corresponding expectations from the cocktail of hadron decays and open charm, in different ranges of p_T. Data and cocktail are absolutely normalized.

The solid curves show the cocktail calculations. In the low mass, the π^0 Dalitz is the dominant source of the electron pairs. The mass spectrum falls rapidly like $1/m_{ee}$ and then bends downward at $m \approx 0.1$ GeV/c^2 due to the cutoff of the π^0 Dalitz decays, followed by an upward bend at $m_{ee} \approx m_{\pi^0} = 0.135$ GeV/c^2, where π^0 contribution cease to exist. For $m_{ee} > m_\pi$, the η Dalitz decay ($\eta \to e^+e^-\gamma$) is the dominant hadronic source of e^+e^- pairs, followed by the ω Dalitz decay ($\omega \to e^+e^-\pi^0$), with small contributions from other sources such as η' and ϕ. The peaks approximately at 0.8 GeV/c^2 and 1.0 GeV/c^2 are due to dielectron decays of the ω and the ϕ mesons, respectively. The detector acceptance and resolution effects broaden and smear the mass spectrum. These detector effects are included in the cocktail calculation.

The $p+p$ data are consistent with expectations from the cocktail over the full mass range in the low-p_T bin. In the highest-p_T bins, however, the data are enhanced with respect to the cocktail. The deviations are, however, small in contrast to the Au+Au data that show a large enhancement in the LMR above m_π^0, which is concentrated at low p_T.

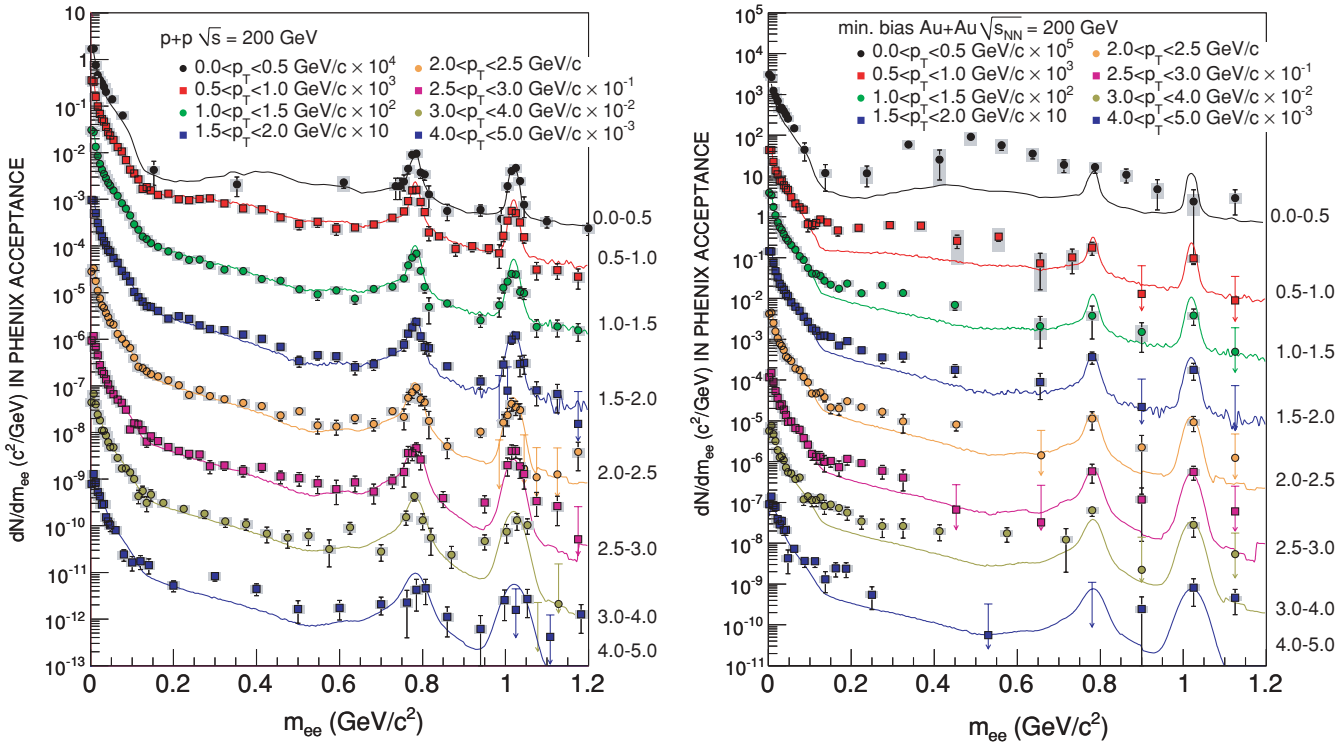

FIG. 30. (Color online) e^+e^- pair invariant mass distributions in $p+p$ (left) and minimum bias Au+Au collisions (right). The p_T ranges are shown in the legend. The solid curves represent the cocktail of hadronic sources (see Sec. IV) and include contribution from charm calculated by PYTHIA using the cross section from Ref. [48] scaled by $N_{\rm coll}$.

For $p_T > 1.0$ GeV/c the enhancement becomes smaller than at lower p_T but it is still larger than the one observed in the $p+p$ data.

In the Introduction, we classified the low-mass region into LMR I (low mass, high p_T) and LMR II (low mass, low p_T) (see Fig. 1). The behavior of the low-mass excess in Au+Au shown in Fig. 30 is different for LMR I and LMR II. In LMR I, the excess has a similar shape to the cocktail and the level of the excess with respect to the cocktail is approximately constant. In this region, a contribution from internal conversion of virtual direct photons is expected. In LMR II, the excess increases with increasing mass and decreasing p_T.

In the following we first analyze the data in the low-mass high-p_T region (LMR I), which allows the measurement of direct photons; then we study how much they contribute to the inclusive enhancement, dominated by the yield in the LMR II.

E. Measurement of direct photons

In general, any source of high-energy real photons can also emit virtual photons that materialize into e^+e^- pairs. The yield of virtual photon is a continuous function of the mass, and the yield of virtual photons gradually approach to that of real photons as $m \to 0$. In LMR I (Fig. 1), where the p_T of the e^+e^- pair is much greater than its mass ($m_{ee} \ll p_T$), the yield of the virtual photons is approximately the same as that of real photons. Therefore, in this quasireal virtual photon region, the production of real direct photons can be deduced from measurements of e^+e^- pairs. Theoretical details are given in Appendix B. In this section, we determine the real direct photon cross section for $1 < p_T < 5$ GeV/c from the data shown in Fig. 30. We use the mass range $0.1 < m_{ee} < 0.3$ GeV/c^2.

The relation between real photon production and the associated e^+e^- production can be written as [Eq. (B3)]

$$\frac{d^2N_{ee}}{dm_{ee}dp_T} = \frac{2\alpha}{3\pi}\frac{1}{m_{ee}}L(m_{ee})S(m_{ee}, p_T)\frac{dN_\gamma}{dp_T}, \tag{31}$$

$$L(m_{ee}) = \sqrt{1-\frac{4m_e^2}{m_{ee}^2}}\left(1+\frac{2m_e^2}{m_{ee}^2}\right). \tag{32}$$

Here α is the fine structure constant, m_{ee} is the mass of e^+e^- pair, m_e is the electron mass, and $S(m_{ee}, p_T)$ is a process-dependent factor that accounts for differences between real and virtual photon production, such as form factors, phase space, and the spectral function. Equation (31) holds for any process emitting real photons, in particular direct or thermal emission. For high p_T ($p_T \gg m_{ee}$) the process dependence becomes negligible and the factor $S(m_{ee}, p_T)$ becomes 1 as $m_{ee} \to 0$ or $m_{ee}/p_T \to 0$. For $m_{ee} \gg m_e$, the factor $L(m_{ee})$ also becomes very close to unity. Thus the relation simplifies to

$$\frac{d^2N_{ee}}{dm_{ee}dp_T} \simeq \frac{2\alpha}{3\pi}\frac{1}{m_{ee}}\frac{dN_\gamma}{dp_T}. \tag{33}$$

Here the mass distribution of electron pairs for a given p_T bin takes on a very characteristic $1/m_{ee}$ shape. If there is real direct photon production in a given p_T bin, there should be

a corresponding electron pair contribution that behaves like $1/m_{ee}$ in the same p_T bin. Therefore, the real direct photon production can be determined from the yield of the excess electron pairs.

For Dalitz decays, the $1/m_{ee}$ behavior is truncated by the kinematic limit and $S(m_{ee})$ becomes zero for $m_{ee} > m_h$, where m_h is the mass of the hadron. The functional form of $S(m_{ee})$ for Dalitz decays is given by Eq. (B10) in Appendix B. In contrast, the factor $S(m_{ee}, q)$ for the direct photon process is unity for $p_T \gg m_{ee}$. We exploit this difference to separate the direct photon signal from the hadronic background. Since 80% of the hadronic photons are from π^0 Dalitz decays, the signal-to-background (S/B) ratio for the direct photon signal improves by a factor of five for $m_{ee} > m_{\pi^0} \approx 0.135$ GeV/c^2, thereby allowing a real direct photon signal that is 10% of the yield of hadronic decay photons to be observed as a 50% excess of e^+e^- pairs for this mass range.

Figure 30 shows a visible excess above the π^0 cutoff for all p_T bins of the Au+Au data. For $p_T > 1$ GeV/c, the excess is almost a constant factor above the cocktail. As we examine later the mass distribution for $p_T > 1$ GeV/c is consistent with the $1/m_{ee}$ shape expected for the electron pairs from internal conversion of virtual direct photons.

In the following we assume the excess for $p_T > 1$ GeV/c and $m_{ee} < 0.3$ GeV/c^2 is entirely due to internal conversion of virtual direct photons and deduce the real direct photon yield from the e^+e^- pair yield using Eq. (31). We demonstrate the validity of this assumption later. Although the data are consistent with $1/m_{ee}$ over a wider mass range ($m_{ee} \sim 0.7$ GeV/c^2), we limit our analysis for $0.1 < m_{ee} < 0.3$ GeV/c^2. We do so in order (i) to ensure the condition $m_{ee} \ll p_T$ for the lowest p_T bin ($1.0 < p_T < 1.5$ GeV/c), (ii) to keep the correction factor $S(M, q)$ close to unity, and (iii) to minimize uncertainty due to $c\bar{c}$. In this kinematic range, the contribution of $c\bar{c} \to e^+e^-$, estimated by PYTHIA, is less than 5% of the excess.

In order to quantify the excess, we fit a two-component function,

$$f(m_{ee}; r) = (1 - r) f_c(m_{ee}) + r f_{\rm dir}(m_{ee}) \qquad (34)$$

to the mass distribution. Here $f_c(m_{ee})$ is the shape of the cocktail mass distribution (shown in Fig. 30), $f_{\rm dir}(m_{ee})$ is the expected shape of the virtual direct photon internal conversion mass distribution, and r is the only fit parameter. In the low-mass region used for the fit, the functional form of $f_c(m_{ee})$ is the sum of Dalitz decay mass distributions of hadrons [Eq. (B8)–Eq. (B10)] filtered through the PHENIX acceptance and smeared by the detector effects. It is calculated by a Monte Carlo simulation that takes into account detector effects such as finite mass resolution. The functional form of $f_{\rm dir}(m_{ee})$ corresponds to Eq. (31) with $S(m_{ee}) = 1$. It is also filtered through the PHENIX acceptance and smeared by detector effects.

Both $f_c(m_{ee})$ and $f_{\rm dir}(m_{ee})$ are separately normalized to the data for $m_{ee} < 30$ MeV/c^2. In this mass region $S(m_{ee})$ of π^0 Dalitz decays is very close to unity. Thus the functional shapes of f_c and $f_{\rm dir}$ are essentially identical and equal to $L(m_{ee})/m_{ee}$ smeared by the detector effects. This means that the fit function $f(m_{ee}; r)$ in this mass range is independent of the fit parameter r as $(1 - r)L(m_{ee})/m_{ee} + rL(m_{ee})/m_{ee} = L(m_{ee})/m_{ee}$. Thus this normalization ensures that the yield of fit function $f(m_{ee}; r)$ is always normalized to that of the data for $m_{ee} < 30$ MeV/c^2. The parameter r can be interpreted as the direct photon fraction of the inclusive photon yield.

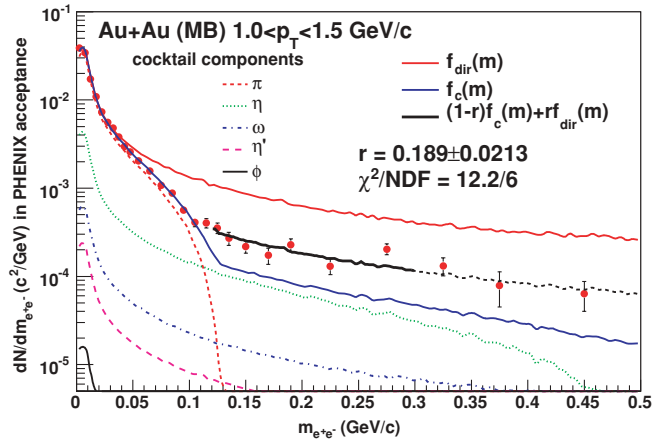

FIG. 31. (Color online) Electron pair mass distribution for Au+Au (Min.Bias) events for $1.0 < p_T < 1.5$ GeV/c. The two-component fit is explained in the text. The fit range is $0.12 < m_{ee} < 0.3$ GeV/c^2. The dashed (black) curve at greater m_{ee} shows $f(m_{ee})$ outside of the fit range.

This fitting method has the advantage of canceling most of the systematic uncertainties of the cocktail normalization relative to the data. The PHENIX acceptance for electron pairs with $m_{ee} < 0.3$ GeV/c^2 and $p_T > 1$ GeV/c is almost constant, and its shape can be calculated accurately as a function of mass. Many systematic effects, such as electron identification efficiency, detector dead area, etc., can influence the absolute value of the acceptance but not its shape.

For each p_T bin, $f(m_{ee})$ is fit to the data for several mass ranges with r the only fit parameter. Figure 31 shows $f_{\rm dir}(m_{ee})$ and $f_c(m_{ee})$ together with the fit result for Au+Au Min.Bias data for $1.0 < p_T < 1.5$ GeV/c and the cocktail components. The dashed curve shows $f(m_{ee})$ extended outside of the fit range. Although the mass region is not used in the fit, the fit function describes the data for $m_{ee} > 0.3$ GeV/c^2.

The fit shown in Fig. 31 has $\chi^2/{\rm NDF} = 12.2/6$. The somewhat large χ^2 values is due to the large contribution from the lowest mass bins, where statistical errors are small and systematic errors due to the detector resolution are significant. The χ^2 value is calculated from the statistical errors only. The results for the fit range $0.12 < m_{ee} < 0.3$ GeV/c^2 are summarized in Table X. For $p_T > 1.5$ GeV/c^2 the fit gives good χ^2/NDF, demonstrating that the shape of the excess is consistent with $1/m_{ee}$ as expected for internal conversion.

To evaluate the systematic uncertainty due to the mass range used for the fit, the fit was repeated for three mass ranges: $0.08 < m_{ee} < 0.3$ GeV/c^2, $0.1 < m_{ee} < 0.3$ GeV/c^2, and $0.12 < m_{ee} < 0.3$ GeV/c^2. The value of r is taken as the average of the results for these three fit ranges.

The sources of systematic uncertainty on the fit include (a) the fit range, (b) the mass spectrum of the data, and (c) the cocktail. The sources of the systematic uncertainty on the mass spectrum relative to the cocktail include (a) uncertainties

TABLE X. Summary of the fits to Eq. (34) in the range $0.12 < m_{ee} < 0.3$ GeV/c^2.

p_T (GeV/c)	r	χ^2/NDF
1.0–1.5	0.189 ± 0.021	12.2/6
1.5–2.0	0.165 ± 0.022	4.6/6
2.0–2.5	0.146 ± 0.029	6.6/6
2.5–3.0	0.165 ± 0.040	3.3/6
3.0–4.0	0.224 ± 0.048	3.7/6
4.0–5.0	0.206 ± 0.093	4.2/3

TABLE XI. Summary of a constant fit to the ratio data shown in Fig. 32. The fit range is $0.11 < m_{ee} < 0.7$ GeV/c^2.

p_T (GeV/c)	$\langle R \rangle$	χ^2/NDF
1.0–1.5	0.173 ± 0.015	16.9/12
1.5–2.0	0.149 ± 0.016	14.8/12
2.0–2.5	0.125 ± 0.020	14.7/12
2.5–3.0	0.115 ± 0.028	9.1/12
3.0–4.0	0.210 ± 0.033	4.4/12

on the correlated background due to jet pairs ($\simeq$2% for $p+p$), (b) uncertainties in the acceptance and efficiency in the mass range of the signal ($0.1 < m_{ee} < 0.3$ GeV/c^2) relative to the mass range ($m_{ee} < 30$ MeV/c^2) used for the normalization ($\simeq$1% for acceptance and $\simeq$1% for efficiency), and (c) uncertainty in the mixed-event normalization [0.25%/(S/B)], where S/B is the signal-to-background ratio in $0.1 < m_{ee} < 0.3$ GeV/c^2. The uncertainty (2) is small since uncertainties in the absolute normalization cancel when the cocktail is normalized to the data in the low-mass peak ($m_{ee} < 30$ MeV/c^2). The largest source of uncertainty is the particle composition in the hadronic cocktail, namely the η/π^0 ratio. This corresponds to a $\simeq$7% ($\simeq$17%) uncertainty in the $p+p$ (Au+Au) cocktail for $0.1 < m_{ee} < 0.3$ GeV/c^2. All systematic uncertainties are added in quadrature to obtain the total systematic uncertainty.

Since the η/π^0 ratio is the largest source of uncertainty, we also studied fits with a three component function, $f_3(m_{ee}) = (1 - r - r_\eta) f_c(m_{ee}) + r f_{\rm dir}(m_{ee}) + r_\eta f_\eta(m_{ee})$, with a constraint on r_η such that $\eta/\pi^0 = 0.48 \pm 0.03(0.08)$ for $p+p$ (Au+Au) [61]. These alternative fits give consistent results for r within statistical uncertainties.

So far we have assumed that the excess in $p_T > 1$ GeV/c and $0.1 < m_{ee} < 0.3$ GeV/c^2 is entirely due to internal conversion of virtual direct photons. This means that we assume $S(m_{ee}, q)$ for excess virtual photons to be unity. In the following, we examine the validity of the assumption from the data.

As shown in Appendix B, the shape of the virtual photon spectrum as a function of mass can be obtained from the electron pair yield as

$$q_0 \frac{dN^*_\gamma}{d^3q} = \frac{3\pi}{2\alpha} m_{ee} \times q_0 \frac{dn_{ll}}{d^3q dm_{ee}}. \quad (35)$$

Since the shape of $f_{\rm dir}(m_{ee})$ is $1/m_{ee}$ smeared by the detector effects, a fit of $R = (\text{data} - \text{cocktail})/f_{\rm dir}(m_{ee})$ to a constant can be used to test that the excess has the shape expected for internal conversion of direct photons. Note that the detector effects in the numerator and denominator cancel in the ratio. Furthermore, since $f_{\rm dir}(m_{ee})$ is normalized to the data for $m_{ee} < 30$ MeV/c^2, R can be interpreted as the ratio of the virtual photon yield to the inclusive real photon yield:

$$R(m, p_T) \simeq \frac{dN^{\rm excess}_{\gamma^*}(m, p_T)}{dp_T} \Big/ \frac{dN^{\rm incl}_\gamma(p_T)}{dp_T} \quad (36)$$

$$= S(m, p_T) dN^{\rm direct}_\gamma(p_T)/dN^{\rm incl}_\gamma(p_T). \quad (37)$$

Figure 32 shows R as a function of m_{ee} for $0.1 < m_{ee} < 0.7$ GeV/c^2. The ratio cannot be measured for $m_{ee} < 0.1$ GeV/c^2 because in this mass region the signal is masked by large background from π^0 Dalitz decays. The distributions are consistent with a constant for the five p_T bins. For the highest p_T bin ($p_T > 4$ GeV/c) the shape of the virtual photon mass spectrum is not well constrained due to limited statistics. However, it is reasonable to expect that the same constant behavior continues for higher p_T. The $\pm 1\sigma$ band of a constant value fit are shown in each panel. Table XI summarizes the results of the fits. For all p_T bins, the constant value fit gives a good χ^2/NDF value. This demonstrate that the data are consistent with a constant $S(m_{ee})$ for these p_T bins.

As discussed in Appendix B, the ratio is expected to be a smooth function of m_{ee}. Hadronic and partonic direct photon contributions to $S(m_{ee}, q)$ are expected to be nearly constant in this range. $q\bar{q}$ annihilation can make a contribution proportional to m^2_{ee} but should be much smaller than these two components for $0.1 < m_{ee} < 0.3$ GeV/c^2 [18–20]. There is no sign of a component that scales with m^2_{ee} for $m_{ee} < 0.3$ GeV/c^2, suggesting that the $q\bar{q}$ contribution is indeed small. Figure 32 illustrates that $S(M, q)$ is indeed constant and supports the use of r obtained from our fit as the direct photon fraction in the inclusive photon spectrum.

The absence of any increase in $R(m_{ee})$ for $m_{ee} > 0.5$ GeV/c^2 is somewhat surprising. A constant R as function of m_{ee} implies that the $S(m_{ee})$ is also a constant. If the excess electron pairs are thermal pairs from the medium, we expect an increasing contribution from $q\bar{q}$ annihilation or from the tail of the (possibly modified) ρ resonance, which leads to increase of $S(m_{ee})$ in higher mass. The data show no indication of such increase. For thermal radiation, $S(m_{ee})$ is the space time average of a product of electromagnetic spectral function and the Boltzmann factor, see Eq. (B24). We note that the Boltzmann factor $f^B = 1/(e^{E/T} - 1)$ can cause significant suppression of $S(m_{ee}, q)$ for $m_{ee} > 0.5$ GeV/c^2. Thus the nearly constant behavior of $R(m_{ee})$ for $m_{ee} > 0.3$ GeV/c should not be interpreted as absence of any contribution other than internal conversion of virtual direct photons at large m_{ee}.

Figures 33(a) and 33(b) show the fraction $r = \frac{\text{direct } \gamma}{\text{inclusive } \gamma}$ of the direct photon component determined by the two-component fit [see Eq. (34)] in $p+p$ and Au+Au collisions, respectively. The curves represent the expectations from a next-to-leading-order perturbative QCD (NLO pQCD) calculation [80]. For $p+p$, the curves show the ratio $d\sigma^{\rm NLO}_\gamma(p_T)/d\sigma^{\rm incl}_\gamma(p_T)$, and $d\sigma^{\rm incl}_\gamma(p_T)$ is the $p+p$ inclusive photon cross section (obtained from the data

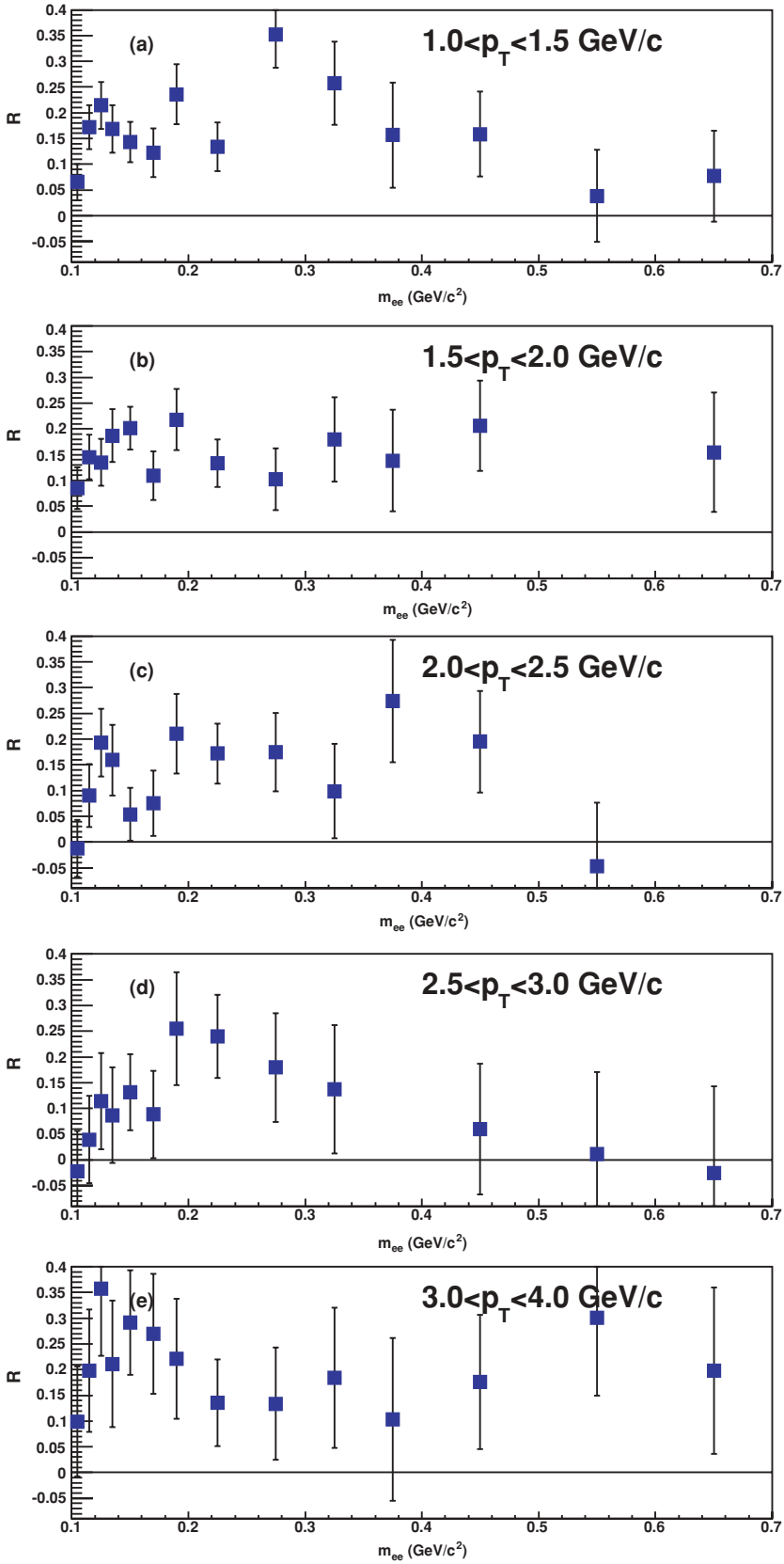

FIG. 32. (Color online) Ratio $R = (\text{data} - \text{cocktail})/f_{\text{dir}}(m_{ee})$ of electron pairs for different p_T bins in Min.Bias Au+Au collisions. The p_T range of each panel is indicated in the figure.

as described later). For Au+Au, the curves represent $T_{\text{AA}} d\sigma_{\gamma}^{\text{NLO}}(p_{\text{T}})/dN_{\gamma}^{\text{incl}}(p_T)$, where T_{AA} is the Glauber nuclear overlap function and $dN_{\gamma}^{\text{incl}}(p_T)$ is the Au+Au inclusive photon yield. The three curves corresponding (from top to bottom) to the theoretical scales set to $\mu = 0.5 p_T$, p_T, and 2 p_T, respectively, show the scale dependence of the

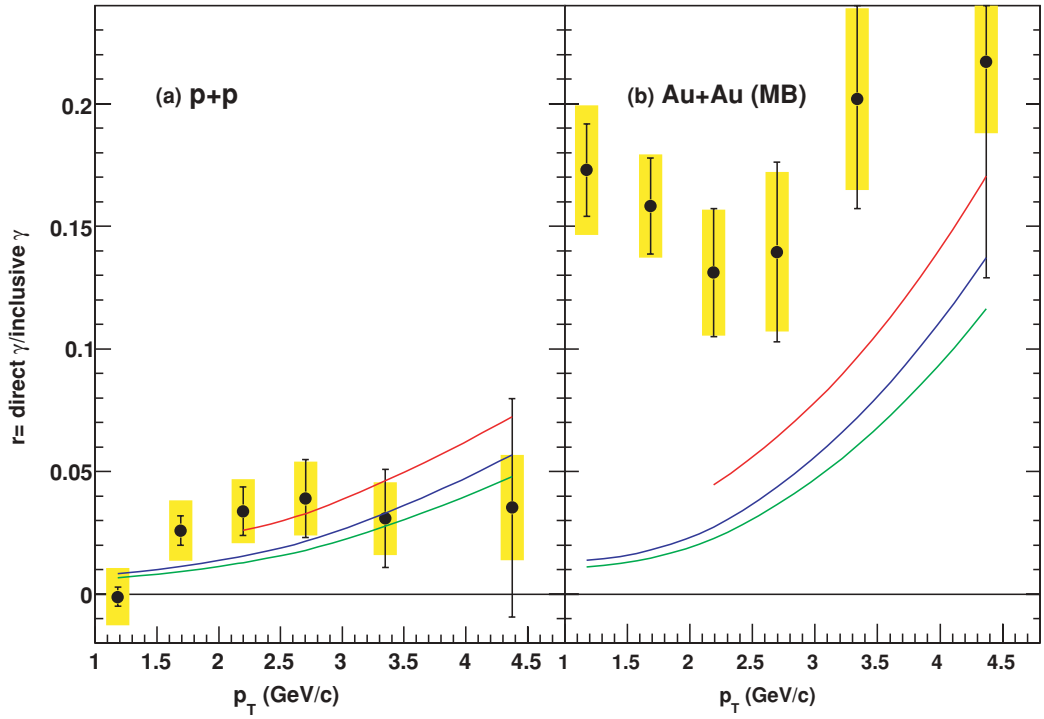

FIG. 33. (Color online) The fraction of the direct photon component as a function of p_T. The error bars and the error band represent the statistical and systematic uncertainties, respectively. The curves are from a NLO pQCD calculation (see text).

calculations. While the fraction r is consistent with the NLO pQCD calculation in $p+p$, it is larger than the calculation in Au+Au for $p_T < 4.5$ GeV/c.

The direct photon fraction r in Fig. 33 is converted to the direct photon yield using $dN_\gamma^{\rm dir}(p_{\rm T}) = r \times dN_\gamma^{\rm incl}(p_T)$. Here we determine the inclusive photon yield for each p_T bin from the yield of low mass e^+e^- pairs in the range $m_{ee} < 30$ MeV/c^2 using the following method. The differential yield of electron pairs is related to that of photons by Eq. (31). The process dependent factor $S(m_{ee}, q)$ is unity within a few percentages for any source of photon for $m_{ee} < 30$ MeV/c^2. Thus the measured yield of electron pairs ($N_{ee}^{\rm data}$) in $m_{ee} < 30$ MeV/c^2 for a given p_T bin is proportional to that of inclusive photons in the same p_T bin.

$$N_{ee}^{\rm data}(p_T) = \epsilon^{\rm acc} K \frac{dN_\gamma^{\rm incl}}{dp_T}, \tag{38}$$

$$K = \int_0^{30\ {\rm MeV}/c^2} \frac{2\alpha}{3\pi} \frac{L(m_{ee})}{m_{ee}} dm_{ee}. \tag{39}$$

Here $\epsilon^{\rm acc}$ represents the acceptance of PHENIX. The same relation holds for the cocktail calculation of photon and electron pairs.

$$N_{ee}^{\rm cocktail}(p_T) = \epsilon^{\rm acc} K \frac{dN_\gamma^{\rm cocktail}}{dp_T}. \tag{40}$$

Here $N_{ee}^{\rm cocktail}$ is the yield of electron pairs for $m_{ee} < 30$ MeV/c^2 in the hadronic cocktail calculation, and $dN_\gamma^{\rm cocktail}/dp_T$ is the yield of photons in the same calculation. Thus we have

$$\frac{dN_\gamma^{\rm incl}}{dp_T} = \frac{N_{ee}^{\rm data}}{N_{ee}^{\rm cocktail}} \times \frac{dN_\gamma^{\rm cocktail}}{dp_T}. \tag{41}$$

The systematic uncertainty in the inclusive photon spectra equals the systematic uncertainty in $N_{ee}^{\rm data}$, which is summarized in Table VI. The total systematic uncertainty in N_{ee} is approximately 20%.

In Fig. 34 the direct photon spectra thus obtained are compared with the direct photon data from Refs. [81,82] and NLO pQCD calculations. The systematic uncertainty of the inclusive photon yield is added in quadrature with the systematic uncertainties of the data. The $p+p$ data are shown as an invariant cross section using $d\sigma = \sigma_{pp}^{\rm inel} dN$ with $\sigma_{pp}^{\rm inel} = 42$ mb.

The direct photon data of this analysis are obtained from the yield of e^+e^- pairs using Eq. (31) under the assumption $S(m_{ee}, q) = 1$ for $0.1 < m_{ee} < 0.3$ GeV/c^2. Although we have shown that our data are consistent with this assumption, what we actually measure is the yield of e^+e^- pairs in this mass range. For completeness, we give the relation between the direct photon yield deduced by the analysis and the electron pair yield that is actually measured. The relation between the real photon yield and the e^+e^- pair yield in this mass range is given by Eq. (B7). Thus the yield of the excess e^+e^- pairs for $0.1 < m_{ee} < 0.3$ GeV/c^2 can be obtained by multiplying the photon yield by a factor of $\frac{2\alpha}{3\pi} \log \frac{300}{100} = 1.7 \times 10^{-3}$.

The pQCD calculation is consistent with the $p+p$ data within the theoretical uncertainties for $p_T > 2$ GeV/c. A similarly good agreement is observed for π^0 [83]. The $p+p$ data can be well described by a modified power-law function

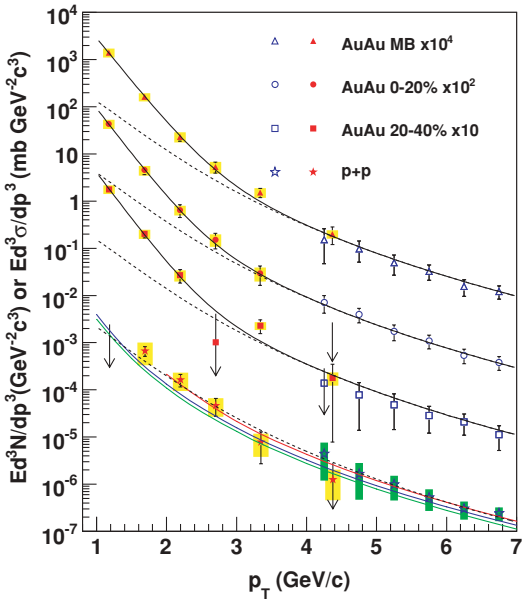

FIG. 34. (Color online) Invariant cross section ($p+p$) and invariant yield (Au+Au) of direct photons as a function of p_T. The filled points are from this analysis and open points are from [81,82]. The three curves on the $p+p$ data represent NLO pQCD calculations, and the dashed curves show a modified power-law fit to the $p+p$ data, scaled by $T_{\rm AA}$. The dashed (black) curves are exponential plus the $T_{\rm AA}$ scaled $p+p$ fit.

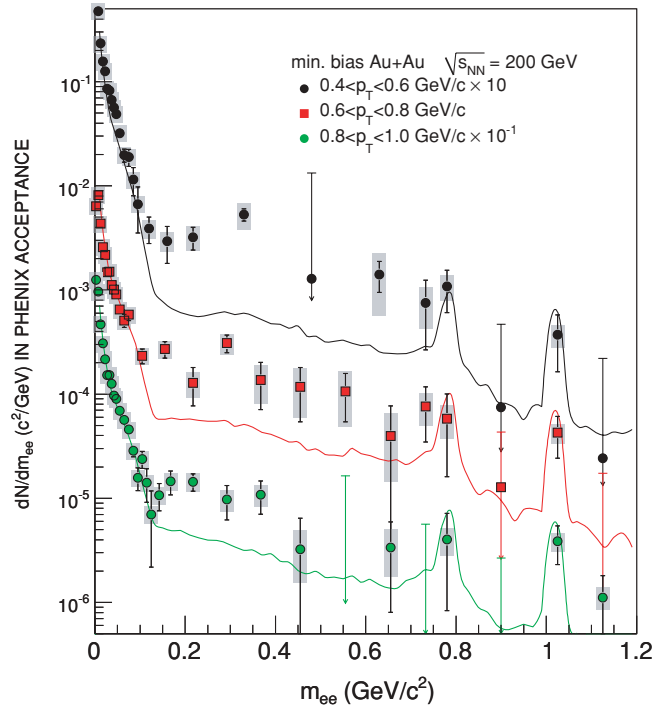

FIG. 35. (Color online) The e^+e^- pair invariant mass distributions in minimum bias Au+Au collisions for the low-p_T range. The solid curves represent the cocktail of hadronic sources (see Sec. IV) and include contribution from charm calculated by PYTHIA using the cross section from Ref. [48] scaled by $N_{\rm coll}$.

$[A_{pp}(1+p_T^2/b)^{-n}]$ as shown by the dashed curve in Fig. 34. The Au+Au data are above the $p+p$ fit curve scaled by $T_{\rm AA}$ for $p_T < 2.5$ GeV/c, indicating that the direct photon yield in the low-p_T range increases faster than the binary-scaled $p+p$ cross section.

We fit an exponential plus the $T_{\rm AA}$-scaled $p+p$ fit function $[Ae^{-p_T/T} + T_{\rm AA} \times A_{pp}(1+p_T^2/b)^{-n}]$ to the Au+Au data. The only free parameters in the fit are A and the inverse slope T of the exponential term. The systematic uncertainties in T are estimated by changing the $p+p$ fit component and the Au+Au data points within the systematic uncertainties. The results of the fits are summarized in Table XII, where A is converted to dN/dy for $p_T > 1$ GeV/c. For central collisions, $T = 221 \pm 19^{\rm stat} \pm 19^{\rm syst}$ MeV. If an unmodified power-law function ($\propto p_T^{-n}$) is used to fit the $p+p$ spectrum, we find $n = 5.40 \pm 0.15$ and $T = 240 \pm 21$ MeV.

TABLE XII. Summary of the fits to the Au+Au data with the exponential plus the modified power-law function $[Ae^{-p_T/T} + B(1+p_T^2/b)^{-n}]$ as explained in the text. The first and second errors are statistical and systematic, respectively.

Centrality	dN/dy ($p_T > 1$ GeV/c)	T (MeV)	χ^2/NDF
0–20%	$1.50 \pm 0.23 \pm 0.35$	$221 \pm 19 \pm 19$	4.7/4
20–40%	$0.65 \pm 0.08 \pm 0.15$	$217 \pm 18 \pm 16$	5.0/4
Min.Bias	$0.49 \pm 0.05 \pm 0.11$	$233 \pm 14 \pm 19$	3.2/4

F. Dependence of low-mass excess

The shape of the enhancement in Au+Au data in LMR II (low mass, low p_T) differs substantially from that in LMR I (low mass, high p_T), where it behaves like $1/m_{ee}$ and is consistent with internal conversion of direct photons. In LMR II, the enhancement is larger, as seen in the two lowest-p_T bins of Fig. 30. For these bins, no excess is observed in the $p+p$ data. In the lowest-p_T bin the enhancement in the Au+Au data is approximately a factor of five above the expectations from the cocktail. The data are significantly above the cocktail up to $m_{ee} = 1$ GeV/c^2, reaching their maximum around $m_{ee} \simeq 0.4$ GeV/c^2.

Figure 35 shows the mass distribution in three p_T bins (0.4–0.6, 0.6–0.8, and 0.8–1.0 GeV/c) in the LMR and a possible transition from $1/m_{ee}$ behavior at higher p_T (LMR I) to much larger enhancement at lower p_T (LMR II). For the highest p_T bin (0.8–1.0 GeV/c) the excess is approximately a constant factor above the cocktail. This means that the mass spectrum is still close to $1/m_{ee}$ expected for internal conversion. The large enhancement seems to appear for the next p_T (0.6–0.8 GeV/c) bin. For the lowest-p_T bin the shape appears to differ from the $1/m_{ee}$ behavior.

Figure 36 shows $R = (\text{data-cocktail})/f_{\rm dir}(m_{ee})$ for the three low-p_T bins. These ratios are proportional to the $S(m_{ee})$ factor, and a constant $S(m_{ee})$ leads to a constant ratio R as a function of mass. While in Fig. 36(a) R is still consistent with a constant as a function of mass, Figure 36(b) suggests that there is an enhancement for $0.1 < m_{ee} < 0.4$, although the statistical

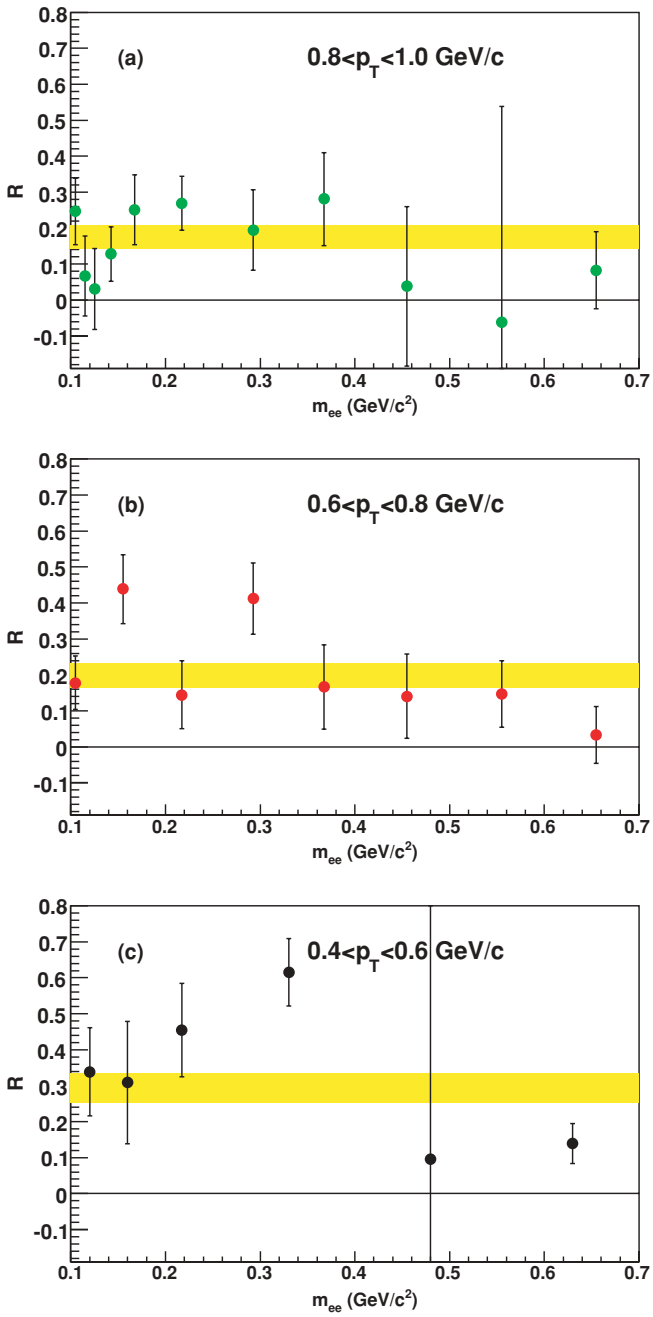

FIG. 36. (Color online) Ratio of $R = (\text{data} - \text{cocktail})/f_{\text{dir}}(m_{ee})$ for different p_T bins [(a): $0.8 < p_T < 1.0$ GeV/c, (b): $0.6 < p_T < 0.8$ GeV/c, (c): $0.4 < p_T < 0.6$ GeV/c] in minimum bias Au+Au collisions. The yellow band in each panel shows $\pm 1\sigma$ band of a constant fit value to the data points.

error is too large to be conclusive. Figure 36(c) suggests a large and broad enhancement around $m_{ee} \simeq 0.4$ GeV/c^2.

We test whether the R distributions in Fig. 36 are consistent with a constant. For each p_T bin, we fit a constant to the data. The results of the fits are shown as the horizontal band in each panel and are summarized in Table XIII. For $0.8 < p_T < 1.0$ GeV/c the fit gives good χ^2/NDF. Thus the data are consistent with the expected $1/m_{ee}$ behavior. The next p_T bin, $0.6 < p_T < 0.8$ GeV/c, gives marginally satisfactory

TABLE XIII. Summary of a constant fit to the ratio data shown in Fig. 36. The fit range is $0.1 < m_{ee} < 0.7$ GeV/c^2.

p_T (GeV/c)	$\langle R \rangle$	χ^2/NDF
0.8–1.0	0.177 ± 0.032	7.7/10
0.6–0.8	0.198 ± 0.033	16.3/7
0.4–0.6	0.293 ± 0.040	21.3/5

χ^2/NDF. For $0.4 < p_T < 0.6$ GeV/c the χ^2/NDF is large and the data are statistically inconsistent with a constant, suggesting that the electromagnetic spectral function is modified at low p_T. However, due to the large uncertainty of the point at $m_{ee} \simeq 0.4$ GeV/c^2 the shape cannot be well determined.

The value $\langle R \rangle$ obtained from the constant fit corresponds to the direct photon fraction r. The fit value for $0.8 < p_T < 1.0$ GeV/c, $\langle R \rangle = 0.177 \pm 0.032$, is consistent with the values of r for higher p_T shown in Fig. 33. If we extrapolate the p_T spectrum of direct photons deduced from the previous section to lower p_T, the expected direct photon fraction for $p_T < 1$ GeV/c is $\simeq$0.17 or less, since the spectrum of decay photons is steeper. The $R(m)$ values for $0.4 < p_T < 0.6$ GeV/c are larger than this expectation for $m_{ee} < 0.4$ GeV/c^2, suggesting that the enhancement in the low-p_T region is larger than that expected from internal conversion of direct photons.

In principle, the distribution of R shown in Fig. 36 can be extrapolated to $m_{ee} = 0$ to obtain the fraction of real direct photons, even if the distribution of R is not flat. However, due to large uncertainties in R for $p_T < 0.8$ GeV/c arising from the combination of multiple dilepton sources, we cannot reliably extrapolate the virtual photon yield to $m_{ee} = 0$ to determine the real direct photon yield for these two p_T bins.

G. Spectra for different mass bins

Figure 37 shows the transverse momentum spectra of dileptons in different mass windows for Au+Au and $p+p$ data:

$$\frac{1}{2\pi p_T}\frac{dN_{ee}}{dp_T dy} = \int_{m_1}^{m_2} \frac{1}{2\pi p_T}\frac{d^3N}{dp_T dy dm_{ee}} dm_{ee}, \qquad (42)$$

where m_1 and m_2 are the lower and upper limits of the different mass slices. In the low-mass slices ($m_{ee} < 0.4$ GeV/c^2) the spectra are truncated at low pair p_T due to the single-track acceptance $p_T > 0.2$ GeV/c. The pair-p_T cutoff is mass dependent. The Au+Au spectra have been divided by $N_{\text{part}}/2$ in order to ease the comparison with the corresponding spectra in $p+p$. The systematic uncertainty due to N_{part} ($\sim$10%) has not been included. In order to avoid the influence of e^+e^- decays of narrow vector mesons, the mass regions around the ω meson (0.78 ± 0.030 GeV/c^2) and the ϕ meson (0.1020 ± 0.030 GeV/c^2) are excluded. The solid curves in Fig. 37 represent the expectations from the hadronic cocktail, which includes also the charm decay contributions. The charm contribution is calculated with PYTHIA. Using the random $c\bar{c}$ correlation makes no difference for $m_{ee} < 0.3$ GeV/c^2 since the charm contribution is negligible at low masses. This

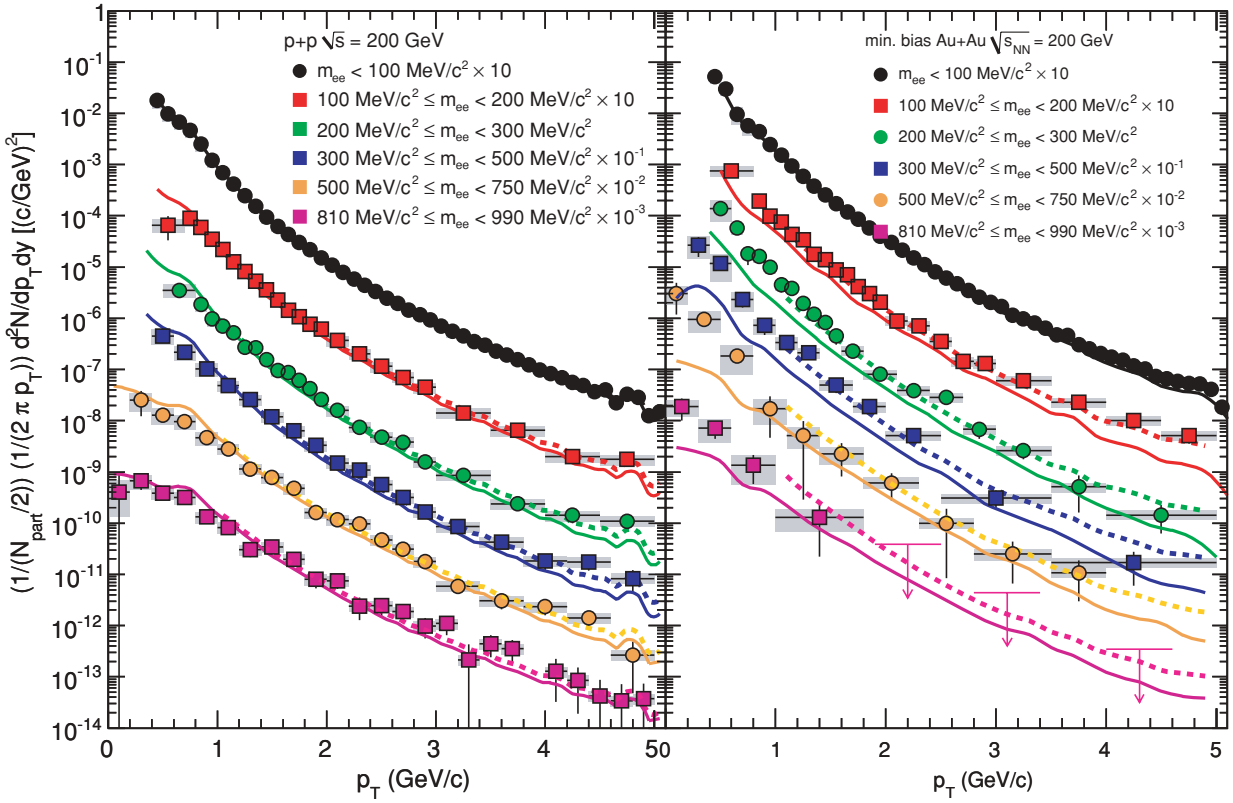

FIG. 37. (Color online) p_T spectra of e^+e^- pairs in $p+p$ (left) and Au+Au (right) collisions for different mass bins, which are fully acceptance corrected. Au+Au spectra are divided by $N_{\rm part}/2$. The solid curves show the expectations from the sum of the hadronic decay cocktail and the contribution from charmed mesons. The dashed curves show the sum of the cocktail and charmed meson contributions plus the contribution from direct photons calculated by converting the photon yield from Fig. 34 to the e^+e^- pair yield using Eqs. (31) and (B14).

difference increases for the higher mass bins, leading to spectra lower by ∼10%, 20%, and 30% for the mass bins $0.3 < m_{ee} < 0.5$ GeV/c^2, $0.5 < m_{ee} < 0.75$ GeV/c^2, and $0.81 < m_{ee} < 0.99$ GeV/c^2, respectively, when the random $c\bar{c}$ correlation is used.

First we concentrate on the comparison between data and the sum of cocktail and charm. In the low-p_T region ($p_T < 1$ GeV/c) all the $p+p$ spectra are consistent with the expectations from the cocktail alone for every mass window. In the high-p_T region, however, the $p+p$ data show a small excess above the cocktail. The Au+Au data are in agreement with the cocktail in the mass region $m_{ee} < 0.1$ GeV/c^2. In higher-mass bins the Au+Au data show a large excess both at low and at high p_T.

As discussed in subsection V E, we have extracted the direct photon yield from the dileptons spectrum in the mass range of $0.1 < m_{ee} < 0.3$ GeV/c^2. The excess in this mass range is consistent with internal conversion of direct photons. As shown in Fig. 32 the direct photon component, which appears as a constant R, extends to the $m_{ee} > 0.3$ GeV/c^2. Therefore, there should be sizable contribution from direct photons in the dilepton spectra for $m_{ee} > 0.3$ GeV/c^2. The relation between real direct photons and virtual photons is presented in Appendix B. Here we use a constant factor $S(m_{ee}, q) = 1$ to extend the direct photon component to higher mass ($m_{ee} > 0.3$ GeV/c^2). The dashed curves in Fig. 37 show the sum of the cocktail, charm and direct photon contributions to the dilepton spectra for $p_T > 1$ GeV/c.

The dashed curves describe the data well for all mass bins both in the Au+Au and the $p+p$ data. This indicates that the excess above the cocktail and charm at high p_T ($p_T > 1$ GeV/c) is consistent with the contribution from direct photons. It is surprising that the agreement holds even for $m_{ee} > 0.5$ GeV/c^2, where significant modifications of the spectral function may be expected due to the presence of the vector mesons. However, the data have large statistical errors for $m_{ee} > 0.5$ GeV/c^2 and additional enhancement over the direct photon contribution is not excluded. The data at high p_T are also consistent with the cocktail alone for $m_{ee} > 0.5$ GeV/c^2.

In the Au+Au data, the enhancement over the cocktail is approximately a constant factor for $p_T > 1$ GeV/c. It grows toward low p_T. All the Au+Au p_T spectra for every mass bin above 0.3 GeV/c^2 seem to indicate that the enhancement with respect to the cocktail below 1 GeV/c is significantly larger than above 1 GeV/c. For $p_T > 1$ GeV/c, the data have a slope similar to the cocktail, as shown by solid curves. For $p_T < 1$ GeV/c, the slope of the data is much steeper than the cocktail.

In order to study this change of the slope in the Au+Au data more quantitatively, we subtract the cocktail plus charm from the data and examine the shape of the excess. The p_T spectra

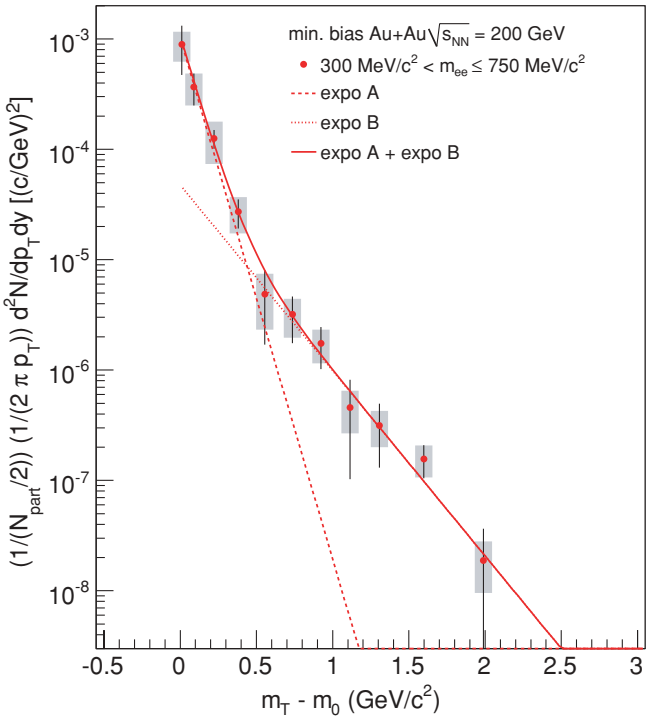

FIG. 38. (Color online) The $m_T - m_0$ spectrum for the mass range $0.3 < m_{ee} < 0.75$ GeV/c^2 after subtracting contributions from cocktail and charm. The spectrum is fully acceptance corrected. The systematic error band includes the difference in charm yields in this mass range. The spectrum is fit to the sum of two exponential functions that are also shown separately as the dashed and dotted lines. The solid line is the sum.

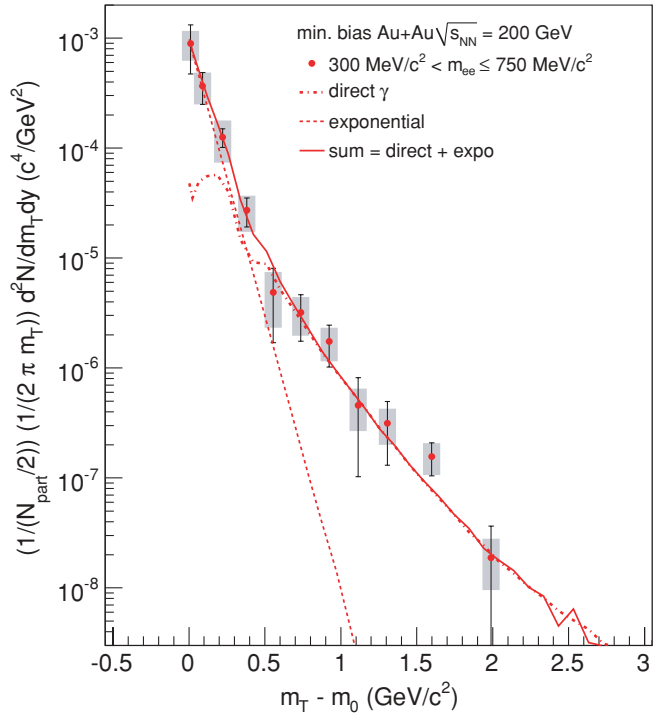

FIG. 39. (Color online) The $m_T - m_0$ spectrum for the mass range $0.3 < m_{ee} < 0.75$ GeV/c^2 after subtracting the contributions from cocktail and charm. The spectrum is fully acceptance corrected. The systematic error band includes the difference in charm yields in this mass range. The spectrum is fit to the sum of direct photons and an exponential function. The dashed-dotted line is the direct photon contribution. The exponential fit to the low-m_T enhancement is also shown (dashed line). The sum is shown with the thick solid line.

are combined in the mass range $0.3 < m_{ee} < 0.75$ GeV/c^2. In this mass range, the low-p_T cutoff which artificially truncates the p_T spectra at lower mass is avoided. The combined data also have increased statistical significance.

Figure 38 shows the pair $m_T - m_0$ spectrum in Au+Au for the pair mass range $0.3 < m_{ee} < 0.75$ GeV/c^2. Here $m_T = \sqrt{p_T^2 + m_0^2}$ is the transverse mass of the pair and m_0 is the mean value of m_{ee} weighted according to dN/dm_{ee} in the given mass range ($0.3 < m_{ee} < 0.75$ GeV/c^2 in this case). We plot the data as function of $m_T - m_0$ since invariant differential cross sections of hadrons in $p+p$, $p+A$, and $A+A$ collisions are generally well described by exponential functions in m_T. Thus the change in the slope can be seen more clearly in the m_T spectrum. The m_T spectrum shows a clear change in the slope around 0.6 GeV/c^2. The slope below $m_T - m_0 < 0.6$ GeV/c^2 is much steeper than that above 0.6 GeV/c^2. In order to characterize the change of the slope in the two m_T regions, we fit the m_T spectrum with the sum of two exponentials:

$$\frac{d^2N}{2\pi m_T dm_T dy} = A_1 \times e^{-\frac{m_T}{T_1}} + A_2 \times e^{-\frac{m_T}{T_2}}, \tag{43}$$

where A_1 and A_2 are the normalization parameters and T_1 and T_2 are the inverse slope parameters.

The result of the fit is shown in Fig. 38. The upper solid curve shows the fit function and the dashed and dotted lines are the two exponential components. The fit gives $T_1 = 92.0 \pm 11.4^{\text{stat}} \pm 8.4^{\text{syst}}$ MeV and $T_2 = 258.4 \pm 37.3^{\text{stat}} \pm 9.6^{\text{syst}}$ MeV with $\chi^2/\text{NDF} = 4.00/9$. The two-exponential fit describes the data well. We note that the value of T_2, is somewhat higher than, but consistent with, the inverse slope of the exponential component of the direct photon spectrum, $T = 221 \pm 19^{\text{stat}} \pm 19^{\text{syst}}$ MeV, obtained in the previous section.

In Fig. 39 the same Au+Au p_T spectrum is fit with the sum of direct photons and an exponential function in m_T. The exponential function is to characterize the low-p_T component. The direct photon component is obtained from the direct photon spectrum in Fig. 34 and extended to the larger mass region assuming $S(m, q) = 1$. We then convert the photon yield to the e^+e^- pair yield using Eq. (31). Thus the direct photon component is fixed and the only free parameters of the fits are the normalization and the inverse slope T of the exponential component.

The p_T spectrum and the individual components of the fit function, i.e., the direct photon component, and the exponential component are shown in Fig. 39. The spectrum is well reproduced by the fit and $\chi^2/\text{NDF} = 16.6/11$. The systematic uncertainty accounts for the uncertainty on the data and the uncertainty (~20%) of the cocktail normalization. From the fit, we extract a value of $T = 86.5 \pm 12.7^{\text{stat}} + 11.0 - 28.4^{\text{syst}}$ MeV. The yield of the low-p_T exponential

extracted from the fit contributes more than 50% of the yield of the spectrum.

Both the two exponentials fit shown in Fig. 38 and the exponential+direct photon fit shown in Fig. 39 show that there is a low inverse slope component with $T \simeq 100$ MeV for $m_T - m_0 < 0.6$ GeV/c^2. In order to further study the mass dependence of the inverse slope, we calculated the local slopes of the invariant pair m_T spectra obtained from the p_T spectra shown in Fig. 37. For all the mass bins the cocktail and charm are subtracted from the data and the average inverse slope $\langle T(m_0)\rangle$ of the excess at mass m_0 has been numerically calculated as

$$\langle T(m_0)\rangle = \frac{\Sigma\left(m_T^i - m_0\right) f\left(m_T^i\right) \Delta m_T^i}{\Sigma f\left(m_T^i\right) \Delta m_T^i}, \tag{44}$$

where

$$f(m_T) = \frac{1}{2\pi m_T} \frac{d^2N}{dm_T dy} \tag{45}$$

$$= \frac{1}{2\pi p_T} \frac{d^2N}{dp_T dy} \tag{46}$$

is the invariant spectrum of the electron pairs after cocktail subtraction shown in Fig. 37.

Figure 40 shows the inverse slopes calculated in two ranges, namely $0 < m_T < 0.6$ GeV/c^2 and $0.6 < m_T < 2.5$ GeV/c^2. For $m_0 < 0.4$ GeV/c^2 the spectra are truncated due to the acceptance; therefore, we do not quote any slope here. Also for $m_0 < 0.1$ GeV/c^2 the slope in the range $0.6 < m_T < 2.5$ GeV/c^2 is not shown because the cocktail subtraction has too large systematic uncertainty in this region. The solid and dashed lines show the inverse slope of the cocktail, calculated in the same way as the data, for the same mass ranges. The inverse slope parameters obtained from the two-exponential fit as well as the exponential+direct photon fit in the same mass ranges are also shown.

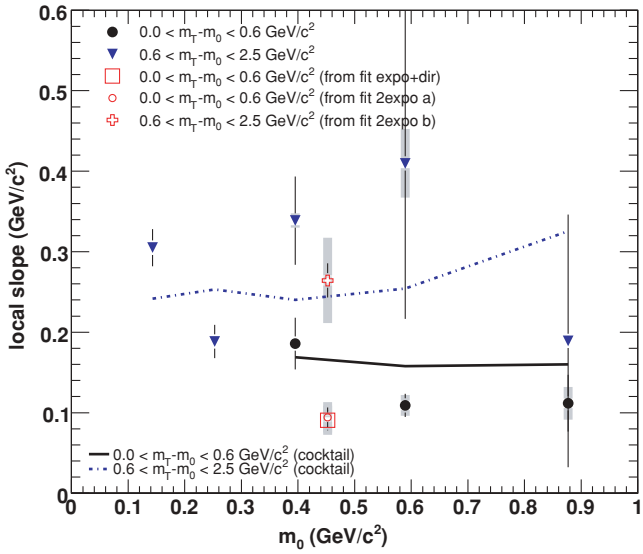

FIG. 40. (Color online) Local inverse slope of the m_T spectra of electron pairs, after subtracting the cocktail and the charm contribution, for different mass bins. The local slope is calculated in different mass ranges, $0 < m_T - m_0 < 0.6$ GeV/c^2 and $0.6 < m_T - m_0 < 2.5$ GeV/c^2. The solid and dashed lines show the local slope of the cocktail for the corresponding mass ranges.

Figure 40 suggests qualitatively different behavior for low and high m_T. In the large $m_T - m_0$ range ($0.6 < m_T - m_0 < 2.5$ GeV/c^2) the inverse slope $\langle T\rangle$ is approximately 300 MeV and similar to that of the cocktail (shown in the dashed-dotted line). In the low $m_T - m_0$ range the inverse slope is approximately 100 MeV, similar to that obtained with the two fit methods. This latter one (shown at $m_T - m_0 \sim 0.45$ GeV/c^2) is lower than that of the cocktail in similar kinematic range (shown in the solid line).

The effective temperature of the lower inverse slope component $T \simeq 100$ MeV, obtained from the two fit methods as well as the numerical calculation, is much lower than the inverse slope of hadrons with similar masses (kaons) measured by PHENIX [60]. The slope of the kaon spectrum is larger than 200 MeV. The hadron slopes rise linearly with mass, consistent with the expectations from radial expansion of the hadronic source. If arising from thermal radiation of the fireball, dominated by pion-pion annihilation $\pi^+\pi^- \to \rho \to e^+e^-$, the excess yield in the LMR would show similar temperatures and a similar linear rise, reminiscent of radial flow of a hadronic source [36]. The value of the low-p_T inverse slope is lower than or similar to the freeze-out temperature. Also the inverse slope of dileptons with an average mass smaller than 0.5 GeV/c^2 is more than a factor 2 smaller than that of kaons. The simplistic expectation, that 0.5 GeV/c^2 dilepton emission is created similarly to kaons (from an equilibrated flowing source), is not supported by the data.

VI. THEORY COMPARISON

The Au+Au e^+e^- spectra are now compared to different models of e^+e^- production in the LMR and in the IMR. These models, employed at SPS energies, identified the pion annihilation process as the main source of thermal dileptons in the hadronic phase of the fireball. However, this process, mediated by the intermediate ρ meson, failed to describe the observed enhancement in the LMR [84] at the SPS energy when vacuum properties of the ρ are used. This suggested that in-medium modifications of the ρ spectral function could be responsible for the enhancement of dilepton yield below the ρ mass. The proposed modifications mostly followed two different approaches:

(i) The *dropping mass* scenario followed the scaling conjecture of G. E. Brown and M. Rho [21], which postulates that the mass of vector mesons decreases in dense matter as the quark condensate $\langle\bar{q}q\rangle$ decreases due to partial restoration of chiral symmetry. This leads to a decrease of the mass of ρ meson from its vacuum value (0.77 GeV/c^2) and causes enhancement of the dilepton yield below the ρ mass.

(ii) The *broadening mass* scenario explains the LMR dilepton enhancement by hadronic many-body interactions [26]. The spectral function in a hot and strongly interacting hadron resonance gas is calculated. The many-body interactions cause the broadening of the

ρ resonance, leading to enhancement of dilepton yield below ρ mass. Other hadronic many-body interactions contribute to low mass enhancement.

There seems now to be consensus that the dropping mass scenario alone cannot adequately reproduce the SPS data. These two scenarios, sometimes in combination, are used by different groups to calculate the dilepton yield at the top RHIC energy ($\sqrt{s_{NN}} = 200$ GeV). Here we compare calculations by the following three groups to the PHENIX data.

(i) Rapp and van Hees [15,18,85] calculate the rate of dilepton emission from a hadronic gas in thermal equilibrium. In the calculation, the electromagnetic spectral function in the vacuum is constrained by the data of e^+e^- annihilation into hadrons, specifically
- the photoabsorption spectra on nucleon and nuclei in Ref. [86]
- $\pi - N \to \rho - N$ scattering in Ref. [26]
- meson-resonance decay branching ratios in Ref. [87].

The spectral function calculated with this model using no free parameters describes well the e^+e^- spectra in nuclear photoproduction [88]. The spectral function in the medium is modified by hadronic many-body interactions. The spectral function is characterized by the light vector resonances $\rho(770)$, $\omega(782)$, and $\phi(1020)$ at low mass according to the vector-meson dominance model (VDM) and a perturbative quark-antiquark continuum at higher masses. Dilepton production from a partonic phase outshines the hadronic gas radiation for $m_{ee} > 1.5$ GeV/c^2 at RHIC energy due to high initial temperatures.

(ii) Dusling and Zahed [19,89,90] use a chiral reduction formalism to calculate the electromagnetic current-current correlation function in the medium. The experimental data of e^+e^- annihilation, τ-decay, two-photon fusion

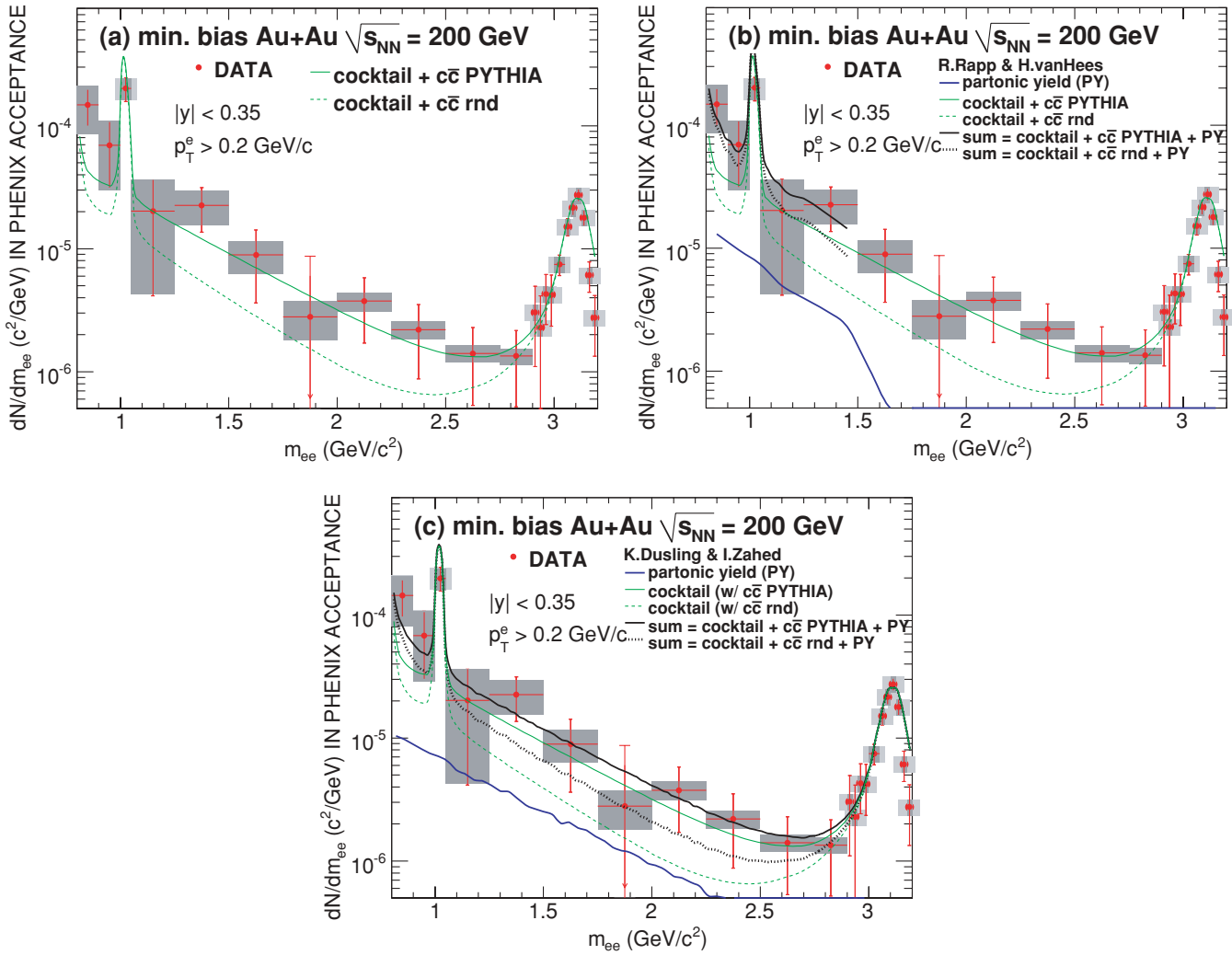

FIG. 41. (Color online) Invariant mass spectra of e^+e^- pairs in Min.Bias Au+Au collisions in the IMR. (Top left) The data are compared to the sum of cocktail+charm. The data are also compared to the sum of cocktail+charm and partonic contributions from different models. The calculations are from (center) Rapp and van Hees [15,18,85] and (right) Dusling and Zahed [19,89,90]. The partonic yields (PY) have been added to the two scenarios for charmed mesons decays, i.e., (i) PYTHIA and (ii) random $c\bar{c}$ correlation.

reactions and pion radiative decays are used to constrain the correlation function. The dilepton emission rates from hadronic gas at finite temperature and baryon density are then computed from a hydrodynamic evolution model of Au+Au collisions. The partonic contribution, which does not become dominant below the ϕ mass, is computed using the Born $q\bar{q}$ annihilation term.

(iii) Cassing and Bratkovskaya [20,27,91,92] use a microscopic relativistic transport model (HSD) that incorporates the relevant off-shell dynamics of the vector mesons. This model is well established to describe the yields, the rapidity distributions, and the transverse-momentum spectra of hadrons in $p+A$ and $A+A$ collisions from GSI Schwerionen Synchrotron to RHIC energies. The model reproduces well the dilepton mass spectrum in $p+p$ collisions. In Au+Au the model includes a modified ρ spectral function according to a collisional broadening scenario as well as a tunable dropping ρ mass scenario. No yield from the partonic QGP phase is available at the moment from the HSD model.

We received numerical values of these model calculations from the authors. The e^+e^- rates from these calculations are filtered into the PHENIX acceptance and compared to the data.

The theory calculation by Rapp and van Hees [15,18,85] is done for a fixed impact parameter $b = 8$ fm. In this calculation the number of charged tracks $N_{\rm ch} = 230$, which is consistent with the measured $N_{\rm ch}$ in Au+Au Min. Bias data [2]. The theory calculation by Dusling and Zahed [19,89,90] is done for a fixed impact parameter for $b = 0$ fm or $N_{\rm part} = 378$.

Since the calculations were provided for central collisions, or for collisions with a fixed impact parameter, in the comparison to our Min.Bias data we normalize the theory calculations by $N_{\rm part}^{\rm model}/N_{\rm part}^{\rm Min.Bias}$, i.e., assuming that the dielectron yield scales with $N_{\rm ch}$. However, this scaling procedure may have introduced some bias in the comparison, as the data show

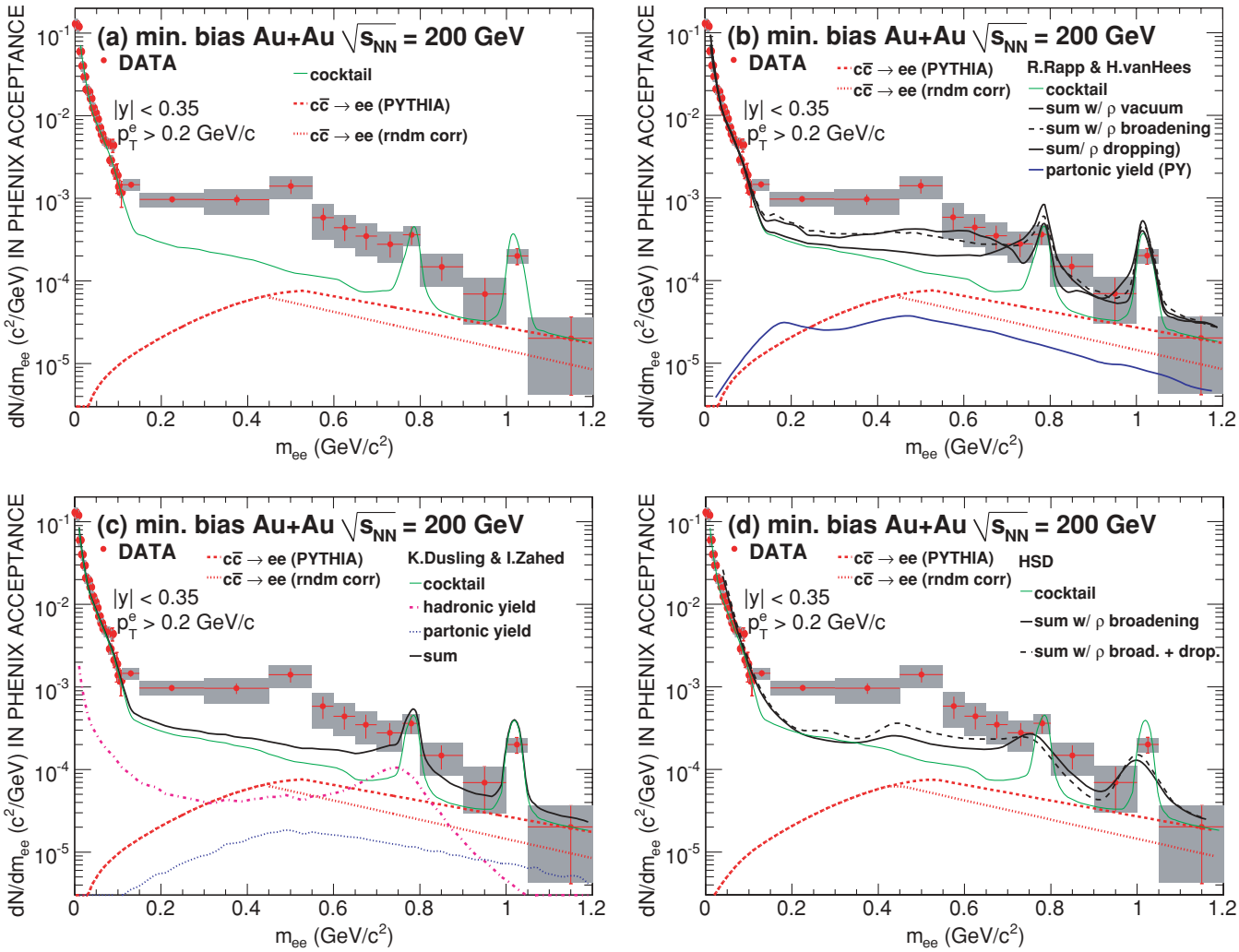

FIG. 42. (Color online) Invariant mass spectra of e^+e^- pairs in Au+Au collisions in the LMR. The data are compared to the sum of cocktail+charm (top left). The data are also compared to the sum of cocktail+charm and hadronic+partonic contributions from different models. The calculations are from. (Top right) Rapp and van Hees [15,18,85], (bottom right) Dusling and Zahed [19,89,90], and Cassing and Bratkovskaya [20,27,91,92].

(Fig. 29) that the dielectron yield increases faster than $N_{\rm part}$ (and $N_{\rm ch}$ is proportional to $N_{\rm part}$). A more detailed comparison requires knowledge of centrality dependence of the dielectron yield both in the data and in the theoretical model.

For comparison to the data, we add these calculations to the hadronic cocktail and the charm decays. The contribution from the freeze-out ρ meson is subtracted from the cocktail to avoid double counting. Because the calculation with the HSD transport model by Cassing and Bratkovskaya [20,27,91,92] can sample any impact parameter, the final Min.Bias cross section is obtained by performing the integration over impact parameter b with a proper geometrical weight. In this case the model also calculates the hadronic contributions, which are in a good agreement with the cocktail. Only the charm contribution is taken from the PYTHIA calculation [55] or from our calculation with random correlation.

In subsection VI E the Au+Au photon spectrum is compared to several theoretical predictions. These employ hydrodynamical models to calculate thermal photon emission from the thermalized partonic and hadronic phases of the reaction, added to NLO pQCD calculations that describe prompt photon emission from perturbative parton-parton scatterings in the first tenths of fm/c of the collision process.

The experimental conditions reached at midrapidity in central heavy-ion collisions at RHIC of nearly zero net baryon density and longitudinally boost invariance in the initial conditions facilitate the applicability of hydrodynamics to describe the reaction evolution. In addition, the thermalization times usually assumed in the hydrodynamical models ($\tau_{\rm therm} \lesssim 1$ fm/c) are, for the first time at RHIC, above the lower limit imposed by the transit time of the two colliding nuclei ($\tau_0 = 2R/\gamma \approx 0.15$ fm/c for Au+Au at 200 GeV).

Hydrodynamical approaches describe, under the assumption of local conservation of energy and momentum, the evolution of the system using the equations of motion of perfect relativistic hydrodynamics complemented with a set of initial

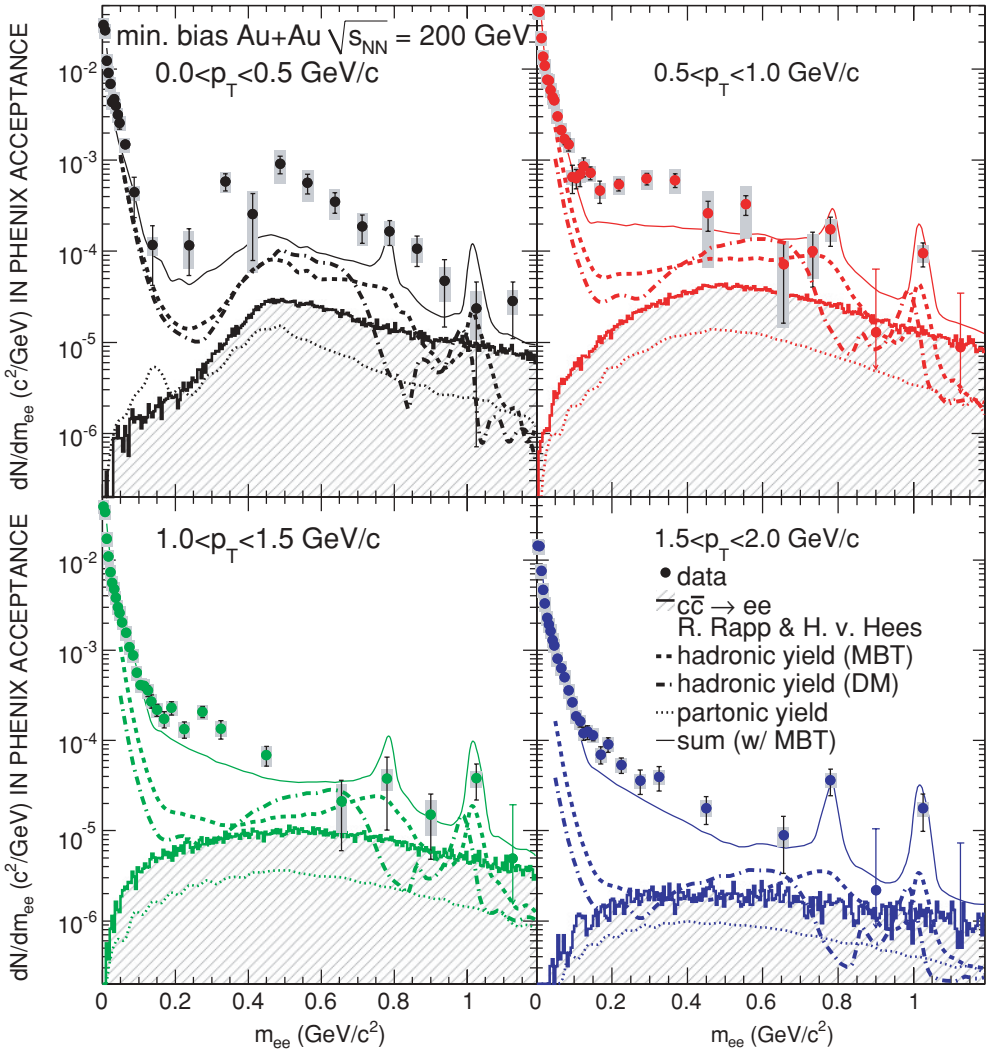

FIG. 43. (Color online) Invariant mass spectra of e^+e^- pairs in Min.Bias Au+Au collisions for different p_T windows compared to the expectations from the calculations of Rapp and van Hees [15,18,85], separately showing the partonic and the hadronic yields and the different scenarios for the ρ spectral function, namely hadron many-body theory (HMBT) and dropping mass (DM). The calculations have been added to the cocktail of hadronic decays (where the contribution of the freeze-out ρ meson is subtracted) and charmed meson decays products.

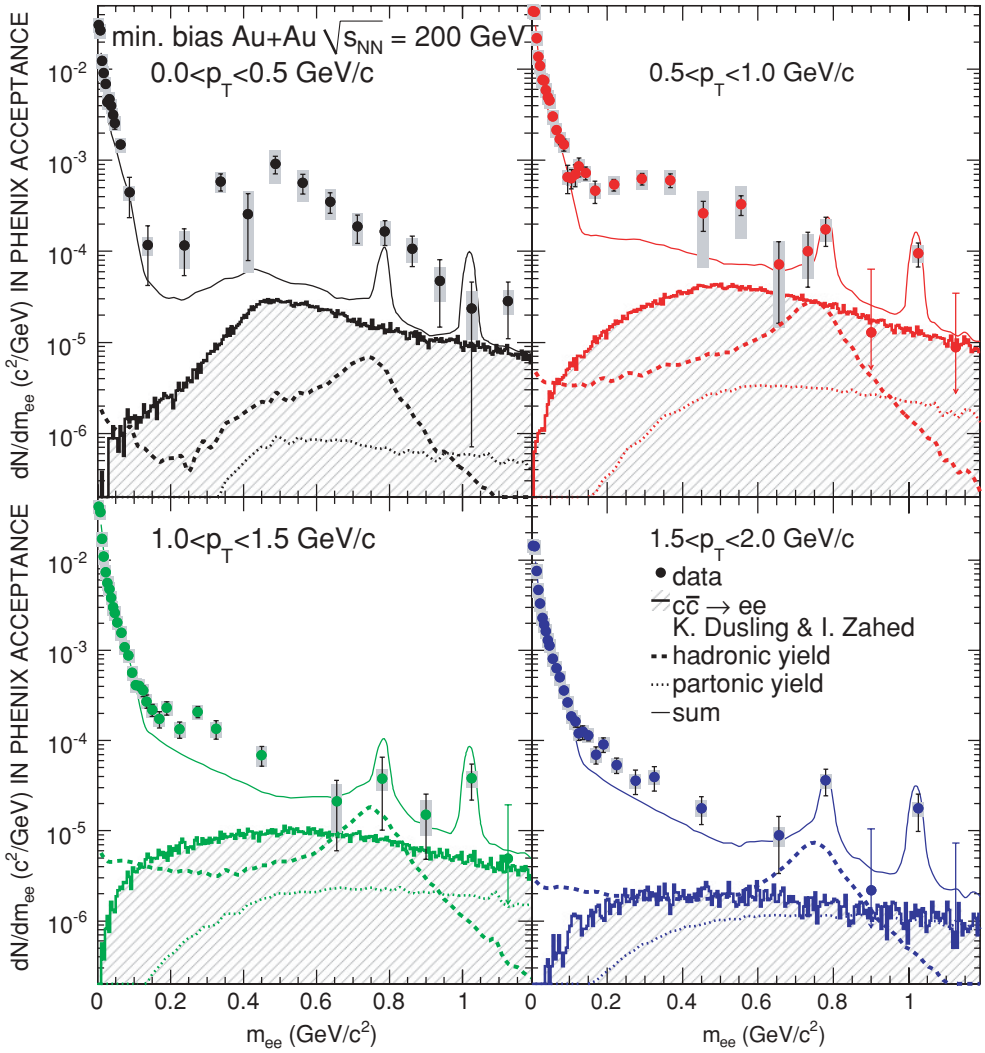

FIG. 44. (Color online) Invariant mass spectra of e^+e^- pairs in Min.Bias Au+Au collisions for different p_T windows compared to the expectations from the calculations of Dusling and Zahed [19,89,90], separately showing the partonic and the hadronic yields. The calculations have been added to the cocktail of hadronic decays (where the contribution of the freeze-out ρ meson is subtracted) and charmed meson decays products.

conditions (e.g., initial temperature $T_{\rm init}$ at thermalization time τ_0), the equation-of-state of the system, and the freeze-out conditions. These models have been very successful in describing quantitatively most of the differential observables of bulk hadronic production (in particular those sensitive to early-times pressure gradients).

The same hydrodynamical models, with initial conditions chosen so as to reproduce the bulk hadron data, are now employed to carry out the description of thermal photon production over the whole space-time evolution of the system.

A. Comparison in the IMR and constraint on possible QGP radiation

In this subsection we compare the model calculations with the data in the IMR and investigate whether the experimental data can constrain the QGP radiation in the IMR. We also study whether we can constrain contributions from charm and QGP radiation in the LMR.

All theoretical models predict that there is large contribution from QGP radiation in the IMR. The QGP radiation competes with the dileptons from correlated charm, which contribute much more than any other cocktail contribution in the IMR. There is a large uncertainty in the charm contribution in Au+Au, since charm quarks are known to suffer energy loss in the medium. Therefore the e^+e^- mass shape from semileptonic decays of charmed quarks may be modified. The shape calculated from PYTHIA [55] provides an upper limit for the expected e^+e^- yield. The shape with random $c\bar{c}$ correlation is softer for $m_{ee} > 0.5$ GeV/c^2, and this provides the lower limit. Below 0.5 GeV/c^2 the two shapes are almost identical.

These two scenarios for the open charm contribution are added to the predictions for the QGP radiation provided by the models described above and are compared to the experimental data in Fig. 41. In all the models the yield in the QGP phase arises entirely from the $q\bar{q} \rightarrow e^+e^-$ annihilation process. The magnitude of the yield is closely linked to the thermalization

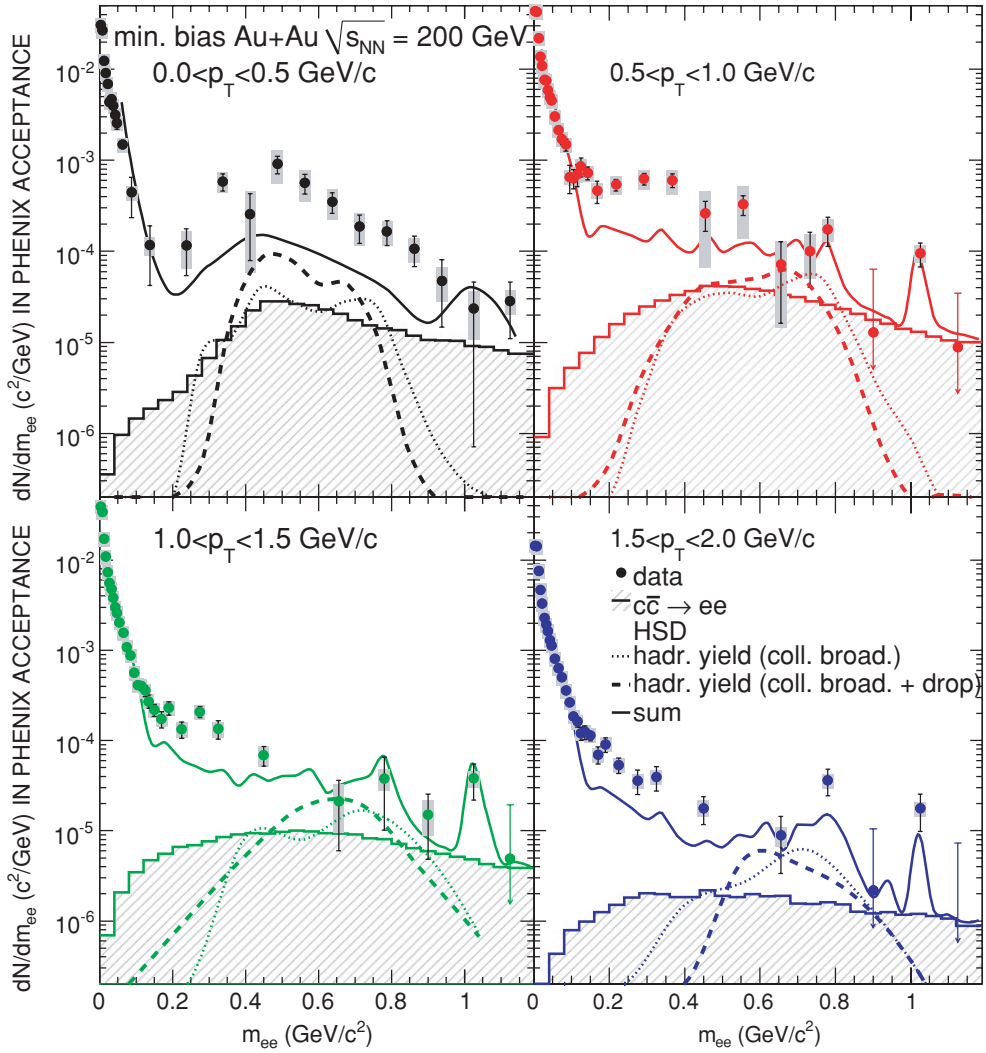

FIG. 45. (Color online) Invariant mass spectra of e^+e^- pairs in Min.Bias Au+Au collisions for different p_T windows collisions compared to the expectations from the calculations of Cassing and Bratkovskaya [20,27,91,92], separately showing the partonic and the hadronic yields calculated with different implementations of the ρ spectral function, namely according to collisional broadening, with or without a dropping mass scenario. The calculations that include the dropping mass scenario have been added to the cocktail of hadronic decays (which is calculated by the HSD model itself) and charmed meson decays products.

time τ_0. A larger τ_0 translates into a reduction of the initial temperature and thus of the total QGP radiation. In Fig. 41 the differences between the models are attributed to different initial conditions used for the hydrodynamic evolution of the QGP phase ($\tau_0 = 0.2$ fm/c for Dusling and Zahed [19,89,90], $= 0.6$ fm/c or Rapp and van Hees [15,18,85]).

In the IMR the data have large statistical errors and systematic uncertainties. Therefore, they do not allow discrimination either between the two proposed scenarios for charm production (PYTHIA [55] or random $c\bar{c}$ correlation) or among the three theoretical models.

B. Inclusive low-mass excess

The data in the IMR do allow setting an upper limit on the contribution arising from charm or from $q\bar{q} \to e^+e^-$ going to the LMR. Indeed we can saturate the IMR yield either with charm or with the partonic yield calculated by the theorists and see what their contribution would be in the LMR. Thus, neither the charm nor the contribution from $q\bar{q} \to e^+e^-$ can be solely responsible of the LMR enhancement.

In the LMR the shape and the yields of the e^+e^- mass spectra from charm calculated by PYTHIA [55] do not differ very much from those given by a calculation which assumes random $c\bar{c}$ correlation, because the shape is mostly determined by the geometrical acceptance. Thus the dilepton yield measured in the IMR gives strong constraint on the charm contribution in the LMR. Since the calculated charm contribution is consistent with the data and is less than the hadronic cocktail below $m_{ee} < 0.5\,\mathrm{GeV}/c^2$, we conclude that charm contribution alone cannot explain the large enhancement observed in the LMR. A similar consideration can be given for the QGP radiation. The contribution from $q\bar{q} \to e^+e^-$ process is negligible in LMR I.

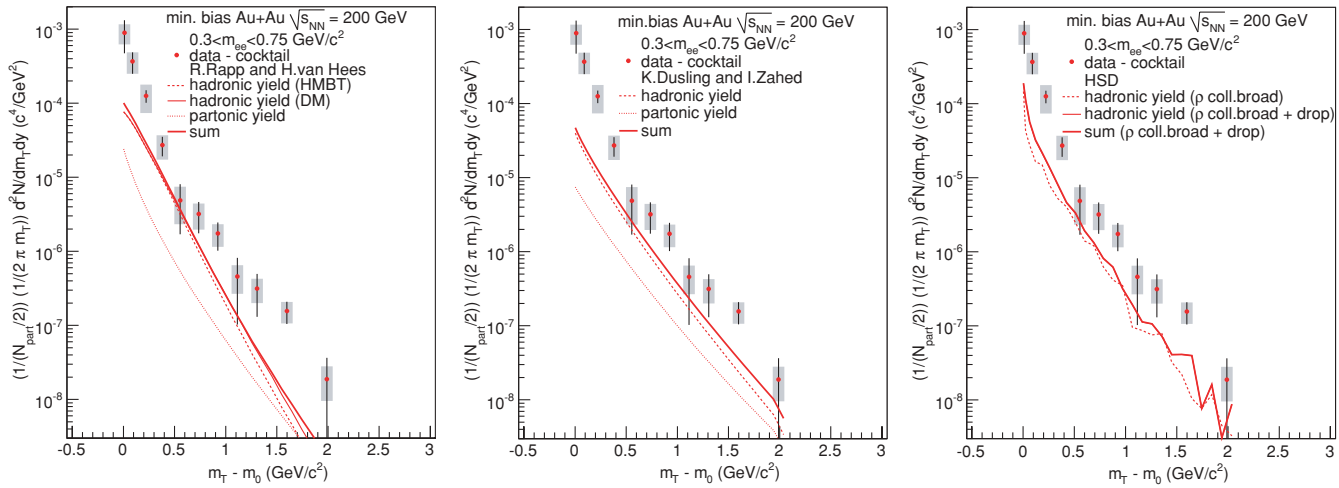

FIG. 46. (Color online) $m_T - m_0$ spectra of e^+e^- pairs for $0.3 < m_{ee} < 0.75$ GeV/c^2 in Min.Bias Au+Au collisions compared to the expectations from the calculations of, respectively, R. Rapp and van Hees [15,18,85], Dusling and Zahed [19,89,90], and Cassing and Bratkovskaya [20,27,91,92]. The spectra are fully acceptance corrected. The curves show separately partonic and hadronic yields. For the curves of Rapp and van Hees [15,18,85] the two scenarios, hadron many-body theory (HMBT) and dropping mass (DM), are shown. The sum is calculated with HMBT. The calculations are compared to the data from which the contributions of the cocktail of hadronic decays and charmed meson decays have been subtracted.

Figure 42 compares the inclusive mass spectrum in the LMR with the cocktail+charm only and with cocktail+charm and the calculations by three groups: Rapp and van Hees [15,18,85], Dusling and Zahed [19,89,90], and Cassing and Bratkovskaya [20,27,91,92]. In all three models the e^+e^- yield in the LMR arises mostly from the hadronic phase. Rapp and van Hees [15,18,85] propose three different scenarios of vector-meson spectral functions: (i) no medium effects, (ii) dropping ρ mass, and (iii) broadening ρ mass and include chemical potential. Dusling and Zahed [19,89,90] use a broadening ρ mass scenario in the hadronic phase and include chemical potential. Chemical potentials are zero at $T_c = T_{\rm chem}$ and then calculated to be nonzero toward thermal freezeout (e.g., up to 100 MeV for pions) to preserve the measured hadron ratios at the values they have at T_c [93,94]. Cassing and Bratkovskaya [20,27,91,92] propose two scenarios: (i) broadening ρ mass and (ii) dropping *and* broadening mass.

The common characteristic of the in-medium effects in these models is a slight suppression of the yield in the ρ-ω region compared with the unmodified ρ scenario and an enhancement in the region $0.4 < m_{ee} < 0.7$ GeV/c^2. The ϕ survives as a pronounced resonance, although its width is broadened. These features become less distinct once the cocktail contribution and the smooth yield from the QGP (which constitutes 15–20%) are added. The differences in the yields of e^+e^- pairs in the various models are attributed to differences in the medium effects on the spectral function, different durations of the lifetime of the fireball in the hadronic phase, and different evolutions of the temperature as a function of time.

While the calculations proposed by Rapp and van Hees [15,18,85] agree with the data for $m_{ee} > 0.5$ GeV/c^2, the ones of Cassing and Bratkovskaya [20,27,91,92] touch the lower end of the systematic uncertainty in the same mass region. The yields calculated by Dusling and Zahed [19,89,90] appear everywhere too low to add significant contribution in the LMR, where the data are enhanced with respect to the hadronic cocktail.

All of the models underpredict the data for $0.2 < m_{ee} < 0.5$ GeV/c^2 by at least a factor of two. It should be noted that the contributions in the region $m_{ee} < 0.4$ GeV/c^2 differ substantially in the three models compared. In Rapp and van Hees [15,18,85] this contribution arises from processes like $a_1 \to \pi\gamma^* \to \pi e^+e^-$ or $N \to N\gamma^* \to Ne^+e^-$. Those processes in the HSD model are suppressed by a few orders of magnitude and are not seen at all compared to the major Dalitz decays. In Dusling and Zahed [19,89,90] the main contribution below the two-pion threshold comes from Π_A, the axial-vector contribution in medium. However, the absolute yield of this process is too low because it is concentrated at very low p_T which is suppressed by our acceptance cut ($p_T^{\rm single} > 0.2$ GeV/c).

C. p_T dependence of low-mass excess

Figures 43, 44, and 45 show the e^+e^- invariant mass spectra in different p_T windows from data compared to the sum of all these contributions for the predictions of Rapp and van Hees [15,18,85], Dusling and Zahed [19,89,90], and Cassing and Bratkovskaya [20,27,91,92], respectively. The contribution from the hadronic and the partonic medium and the charm expectations from PYTHIA [55] are shown separately. The charm distribution from PYTHIA is somewhat harder than the calculations that assume random correlation of the $c\bar{c}$ pair but does not differ very much in the LMR, where the shape of the distribution is essentially determined by the detector acceptance.

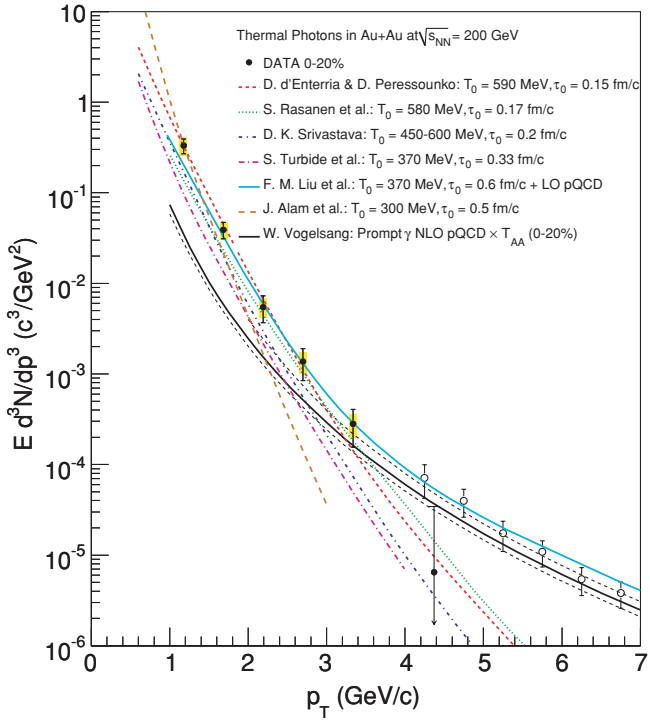

FIG. 47. (Color online) Theoretical calculations of thermal photon emission are compared with the direct photon data in central 0–20% Au+Au collisions (D. d'Enterria and D. Peressounko [95], S. Rasanen *et al.* [96], D. K. Srivastava [97], Turbide *et al.* [98], F. M. Liu *et al.* [99], J. Alam *et al.* [100]). In contrast to the others, the curve by Ref. [99] includes pQCD contributions. The black solid curve show the pQCD calculation [80], scaled by $T_{\rm AA}$. The QCD scale μ is set to p_T for this calculation. The two black dashed curves around the black solid curve show the scale uncertainty, with the upper curve and the lower curve corresponds to $\mu = 1/2 \times p_T$ and $\mu = 2 \times p_T$, respectively.

From the comparison we learn that in general the yield from these theoretical predictions is insufficient to explain the observed enhanced dilepton production, both at low and high momenta. At low p_T, where the enhancement reaches approximately a factor of five, the shape of the enhancement shown by the data differs markedly from any of the theoretical models.

At high p_T ($p_T > 1.0$ GeV/c) the enhancement is about a factor of two over the cocktail and its shape is quite similar to that of the cocktail. In the previous section we showed that this enhancement can be attributed to internal conversion of virtual direct photons. In the theoretical calculations of direct photon emission at RHIC energies, the contribution from the QGP phase, e.g., quark-gluon Compton scattering, is the dominant source of real thermal photons for $p_T > 1$ GeV/c. The process that produces real photons in the QGP should also contribute low mass e^+e^- pairs at high p_T. However, none of the three models includes such processes (e.g., $q + g \to q + \gamma^* \to q + e^+e^-$). The QGP radiation in these models only include $q + \bar{q}$ annihilation. This could explain the discrepancy between the models and the data for $p_T > 1.0$ GeV/c.

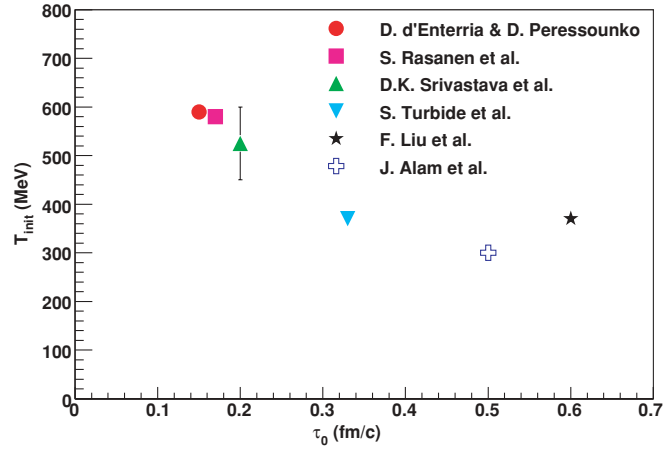

FIG. 48. (Color online) $T_{\rm init}$ vs. τ_0 for various theoretical calculations shown in Fig. 47. D. d'Enterria and D. Peressounko [95], S. Rasanen *et al.* [96], D. K. Srivastava *et al.* [97], Turbide *et al.* [98], F. Liu *et al.* [99], and J. Alam *et al.* [100].

D. p_T spectra in the low-mass region

The p_T spectra of the excess (i.e., after subtracting the hadron cocktail and the charm from the dilepton spectra) can be also compared to the theoretical models. We already noted that the yields from the partonic medium in the theoretical models are produced only via the $q\bar{q} \to e^+e^-$ annihilation process. Processes like $q + g \to qe^+e^-$ are not included.

Figure 46 shows the p_T spectrum in the mass window $0.3 < m_{ee} < 0.75$ GeV/c^2 after subtracting the contribution from the cocktail and the charm. The spectrum is compared to the theoretical calculation from Rapp and van Hees [15,18,85], Dusling and Zahed [19,89,90], and Cassing and Bratkovskaya [20,27,91,92], respectively. The figure shows separately the e^+e^- yields from the partonic phase and the hadronic phase (with two possible implementations of the ρ spectral function) and their sum is compared to the data. In all the models the sum of the cocktail contribution and the e^+e^- yield from medium effects is insufficient to explain the experimental data, and divergences are observed both at low and high p_T. While for Rapp and van Hees [15,18,85] and for Dusling and Zahed [19,89,90] the disagreement with the data is strong at low p_T, for Cassing and Bratkovskaya [20,27,91,92] a better agreement is achieved over the full p_T range. However, the data seem still higher than the theoretical calculations.

E. Theoretical comparison to direct photon measurement

In subsection V E we have extracted the direct photon yield from the analysis of LMR I. The obtained direct photon spectrum in central Au+Au, shown in Fig. 34, shows excess over $T_{\rm AA}$ scaled $p+p$ data, and the shape of the excess is well described by a pure exponential with inverse slope $T \simeq 220$ MeV. If the direct photons in Au+Au collisions are of thermal origin, the inverse slope T is related to the initial temperature $T_{\rm init}$ of the dense matter. In hydrodynamical models, $T_{\rm init}$ is 1.5 to 3 times T due to the space-time evolution [95].

Figure 47 compares the direct photon data in central 0–20% Au+Au collisions with several theoretical calculations of thermal photon emission added to the pQCD calculations [80]. Note that the curve by Ref. [99] includes pQCD contributions, while the others do not. For $p_T < 3$ GeV/c, the thermal contribution dominates over pQCD. These hydrodynamical models can reproduce the high p_T central Au+Au data within a factor of two. These models assume formation of a hot QGP with initial temperature ranging from $T_{\rm init} = 300$ MeV at thermalization time $\tau_0 = 0.6$ fm/c to $T_{\rm init} = 600$ MeV at $\tau_0 = 0.15$ fm/c [95–100]. Figure 48 summarizes the $T_{\rm init}$ and τ_0 for theoretical calculations shown in Fig. 47. There is a clear anticorrelation between $T_{\rm init}$ and τ_0. Lattice QCD predicts a phase transition from hadronic phase to quark-gluon plasma at $\simeq$170 MeV.

VII. SUMMARY AND CONCLUSIONS

PHENIX has measured dilepton production in Au+Au and p+p collisions at $\sqrt{s_{NN}} = 200$ GeV. The measured e^+e^- yield is compared with the cocktail of known sources of light hadron decays. Cocktail sources are mostly measured by PHENIX in the same experimental run via hadronic decay channels. Extrapolations to low p_T, where experimental data are not always available are obtained using an m_T-scaling procedure.

In the p+p data the e^+e^- invariant mass spectrum has been measured in the mass range from 0 to 8 GeV/c^2 for all pair p_T. The IMR is dominated by semileptonic decays of heavy flavor mesons for which the extracted production cross sections is consistent with fixed-order next-to-leading-log (FONLL) predictions and with the PHENIX measurement of single electrons [48].

The LMR can be described by known contributions from light meson decays and virtual direct photons for which the extracted cross section is consistent with NLO pQCD calculations and with PHENIX measurements of real photons.

In Au+Au collisions, the data are consistent with the expectations from correlated $c\bar{c}$ production for $m_{ee} > 1.2$ GeV/c^2. However, this interpretation is ambiguous, due to the interplay between two possible medium effects: energy loss of charm quarks in the medium which would deplete the yield in the IMR, and QGP radiation, which would increase the yield in the IMR.

In the low-mass region the Au+Au Min.Bias inclusive mass spectrum shows an enhancement by a factor of $4.7 \pm 0.4^{\rm stat} \pm 1.5^{\rm syst} \pm 0.9^{\rm model}$ compared to the expectation from the hadronic cocktail. The enhancement is concentrated at low p_T ($p_T < 1$ GeV/c). The integrated yield increases faster with the centrality of the collisions than the number of participating nucleons.

At low mass ($m_{ee} < 0.3$ GeV/c^2) and high p_T ($1 < p_T < 5$ GeV/c), an enhanced e^+e^- pair yield is observed both in p+p and Au+Au collisions. The mass dependence of the excess is consistent with that expected for virtual direct photon production. This excess is used to infer the yield of real direct photons by extrapolating to $m_{ee} = 0$. A perturbative QCD calculation is consistent with the real direct photon cross section in p+p extracted by this method, while in central Au+Au collisions much larger yields compared with the p+p cross section scaled with $T_{\rm AA}$ are observed. In central Au+Au collisions, the excess over the p+p cross section scaled by $T_{\rm AA}$ is exponential in p_T, with inverse slope $T = 221 \pm 19^{\rm stat} \pm 19^{\rm syst}$ MeV.

In Au+Au collisions at very low p_T there is a further, very significant, enhancement that increases strongly with centrality. The p_T spectrum of dileptons in this region has been analyzed with two fit methods and a numerical calculation. An inverse slope of $T \simeq 100$ MeV has been extracted for $m_T < 0.6$ GeV/c, lower than for hadrons with similar mass and similar to the freeze-out temperature.

The Au+Au data are compared to different models that provide additional e^+e^- yield in both the LMR and the IMR. In the IMR the data have too large uncertainty to discriminate different possible scenarios of charm production and QGP radiation. In the LMR no quantitative agreement has been found yet with the models.

The yield of direct photons in Au+Au collisions is compared with several hydrodynamical models of thermal photon emission at RHIC energies. The models assuming the formation of a hot system with initial temperature ranging $T_{\rm init} \simeq 300$–600 MeV at times $\tau_0 \simeq 0.6$–0.15 fm/c are in qualitative agreement with the data. Lattice QCD predicts a phase transition from hadronic phase to quark-gluon plasma at $T \simeq 170$ MeV.

In conclusion, we presented measurements of the e^+e^- continuum in p+p and Au+Au at $\sqrt{s_{NN}} = 200$ GeV in a wide range of mass and transverse momenta. In Au+Au collisions, a large enhancement of the yield of e^+e^- pairs is observed at low mass and low p_T in Au+Au. The yield of direct photons is deduced from low-mass, high-p_T e^+e^- pairs. Future measurements with an upgraded PHENIX detector with higher statistics, together with further advance in theory, will allow more detailed study of the properties of the hot dense matter formed in heavy-ion collisions at RHIC.

ACKNOWLEDGMENTS

We thank the staff of the Collider-Accelerator and Physics Departments at Brookhaven National Laboratory and the staff of the other PHENIX participating institutions for their vital contributions. We thank E. L. Bratkovskaya, W. Cassing, and O. Linnyk; K. Dusling and I. Zahed; and R. Rapp and H. van Hees for the use of unpublished calculations and we thank all of them and Y. Hidaka for useful discussions. We acknowledge support from the Office of Nuclear Physics in the Office of Science of the Department of Energy, the National Science Foundation, Abilene Christian University Research Council, Research Foundation of SUNY, and Dean of the College of Arts and Sciences, Vanderbilt University (USA); Ministry of Education, Culture, Sports, Science, and Technology and the Japan Society for the Promotion of Science (Japan); Conselho Nacional de Desenvolvimento Científico e Tecnológico and Fundação de Amparo à Pesquisa do Estado de São Paulo (Brazil); Natural Science Foundation of China (People's Republic of China); Ministry of Education, Youth

and Sports (Czech Republic); Centre National de la Recherche Scientifique; Commissariat à l'Énergie Atomique, and Institut National de Physique Nucléaire et de Physique des Particules (France); Ministry of Industry, Science and Tekhnologies, Bundesministerium für Bildung und Forschung, Deutscher Akademischer Austausch Dienst, and Alexander von Humboldt Stiftung (Germany); Hungarian National Science Fund, OTKA (Hungary); Department of Atomic Energy (India); Israel Science Foundation (Israel); National Research Foundation (Korea); Ministry of Education and Science, Russia Academy of Sciences, Federal Agency of Atomic Energy (Russia); VR and the Wallenberg Foundation (Sweden); the US Civilian Research and Development Foundation for the Independent States of the Former Soviet Union; the US-Hungarian NSF-OTKA-MTA; and the U.S.-Israel Binational Science Foundation.

APPENDIX A: BACKGROUND NORMALIZATION

1. Pairing of electrons and positrons

In the following we assume that, as dictated by the charge conservation law, e^- and e^+ are always produced in pairs and that most of these pairs are produced statistically independent of each other. Let us say N pairs are produced in a particular event and N is given by a probability distribution $P(N)$. Of the N pairs only a fraction ε_p is fully reconstructed, and then the number of reconstructed pairs n_p is given by a binomial distribution B sampling out of N "events" with a probability ε_p.

(i) Probability to get n_p pairs from N true pairs: $\omega(n_p) = B(n_p, N, \varepsilon_p)$
(ii) with an average: $\langle n_p \rangle = \varepsilon_p N$
(iii) and variance: $\sigma_p^2 = \varepsilon_p N(1-\varepsilon_p)$.

Of the remaining pairs one track is reconstructed with a probability ε_+ or ε_-. For a given N and n_p the number of additional single positive tracks n_+ and negative tracks n_- follow a multinomial distribution M with three possible outcomes for each of the $N - n_p$ unreconstructed pairs: no track, one + track, or one − track.

The probability to get n_+ and n_- single tracks from N true pairs with n_p reconstructed pairs, i.e., from $(N - n_p)$ not fully reconstructed pairs is:

$$\begin{aligned}\omega(n_+, n_-) &= M(n_+, n_-; N - n_p, \varepsilon_+, \varepsilon_-)\\ \omega(n_+) &= \sum_{n_-=1}^{N-n_p} M(n_+, n_-; N - n_p, \varepsilon_+, \varepsilon_-)\\ \omega(n_-) &= \sum_{n_+=1}^{N-n_p} M(n_+, n_-; N - n_p, \varepsilon_+, \varepsilon_-)\end{aligned} \tag{A1}$$

(i) with average: $\langle n_\pm \rangle = \varepsilon_\pm (N - n_p)$
(ii) variance: $\sigma_\pm^2 = \varepsilon_\pm (N - n_p)(1 - \varepsilon_\pm)$
(iii) and covariance: $\mathrm{cov}(n_+, n_-) = -(N - n_p)\varepsilon_+\varepsilon_-$.

In this case the number of unlike-sign pairs for a given N and n_p is:

$$\begin{aligned}\langle n_{+-} \rangle &= n_p^2 + n_p \sum_{n_+=1}^{N-n_p} n_+ \omega(n_+) + n_p \sum_{n_-=1}^{N-n_p} n_- \omega(n_-)\\ &\quad + \sum_{n_+=1}^{N-n_p}\sum_{n_-=1}^{N-n_p} n_+ n_- \omega(n_+, n_-)\\ &= n_p^2 + n_p\varepsilon_+(N-n_p) + n_p\varepsilon_-(N-n_p) + \langle n_+ n_- \rangle\\ &= n_p^2 + n_p\varepsilon_+(N-n_p) + n_p\varepsilon_-(N-n_p)\\ &\quad + \varepsilon_+\varepsilon_-(N-n_p)^2 - \varepsilon_+\varepsilon_-(N-n_p)\\ &= n_p^2 + \varepsilon_+ N n_p - \varepsilon_+ n_p^2 + \varepsilon_- N n_p - \varepsilon_- n_p^2\\ &\quad + \varepsilon_+\varepsilon_- N^2 - 2\varepsilon_+\varepsilon_- N n_p + \varepsilon_+\varepsilon_- n_p^2\\ &\quad - \varepsilon_+\varepsilon_- N + \varepsilon_+\varepsilon_- n_p\\ &= [n_p + \varepsilon_+(N-n_p)][n_p + \varepsilon_-(N-n_p)]\\ &\quad - \varepsilon_+\varepsilon_-(N-n_p).\end{aligned} \tag{A2}$$

Similarly we can calculate the number of like-sign pairs:

$$\begin{aligned}2\langle n_{++} \rangle &= \sum_{n_+=1}^{N-n_p} (n_p + n_+)(n_p + n_+ - 1)\omega(n_+)\\ &= n_p^2 - n_p + \langle n_+^2 \rangle - \langle n_+ \rangle + 2n_p\langle n_+ \rangle\\ &= n_p^2 - n_p + \varepsilon_+^2(N-n_p)^2 + \varepsilon_+(1-\varepsilon_+)(N-n_p)\\ &\quad - \varepsilon_+(N-n_p) + 2\varepsilon_+ n_p(N-n_p)\\ &= n_p^2 - n_p + \varepsilon_+^2(N-n_p)^2 - \varepsilon_+^2(N-n_p)\\ &\quad + 2\varepsilon_+ n_p(N-n_p)\end{aligned} \tag{A3}$$

and

$$\begin{aligned}2\langle n_{--} \rangle &= n_p^2 - n_p + \varepsilon_-^2(N-n_p)^2\\ &\quad - \varepsilon_-^2(N-n_p) + 2\varepsilon_- n_p(N-n_p).\end{aligned} \tag{A4}$$

To obtain the expected number of like- and unlike-sign pairs for a fixed number of real pairs N we need to average over all possible reconstructed pairs n_p:

$$\begin{aligned}\langle N_{+-} \rangle &= \sum_{n_p} \langle n_{+-} \rangle B(n_p, N, \varepsilon_p)\\ &= (1 - \varepsilon_+ - \varepsilon_- + \varepsilon_+\varepsilon_-)\langle n_p^2 \rangle\\ &\quad + (\varepsilon_+ N + \varepsilon_- N - 2\varepsilon_+\varepsilon_- N + \varepsilon_+\varepsilon_-)\langle n_p \rangle\\ &\quad + \varepsilon_+\varepsilon_- N^2 - \varepsilon_+\varepsilon_- N\\ &= (1 - \varepsilon_+ - \varepsilon_- + \varepsilon_+\varepsilon_-)\left(\varepsilon_p^2 N^2 + \varepsilon_p(1-\varepsilon_p)N\right)\\ &\quad + (\varepsilon_+ N + \varepsilon_- N - 2\varepsilon_+\varepsilon_- N + \varepsilon_+\varepsilon_-)\varepsilon_p N\\ &\quad + \varepsilon_+\varepsilon_- N^2 - \varepsilon_+\varepsilon_- N\\ &= \left(\varepsilon_p^2 - \varepsilon_p^2\varepsilon_+ - \varepsilon_p^2\varepsilon_- + \varepsilon_p^2\varepsilon_+\varepsilon_- + \varepsilon_p\varepsilon_+ + \varepsilon_p\varepsilon_-\right.\\ &\quad \left. - 2\varepsilon_p\varepsilon_+\varepsilon_- + \varepsilon_+\varepsilon_-\right)(N^2 - N) + \varepsilon_p N\\ &= [\varepsilon_p + \varepsilon_+(1-\varepsilon_p)][\varepsilon_p + \varepsilon_-(1-\varepsilon_p)]\\ &\quad (N^2 - N) + \varepsilon_p N.\end{aligned} \tag{A5}$$

Now we calculate the like-sign background:

$$\begin{aligned}2\langle N_{++}\rangle &= \sum_{n_p} 2\langle n_{++}\rangle B(n_p, N, \varepsilon_p)\\ &= \varepsilon_p^2 N^2 + \varepsilon_p(1-\varepsilon_p)N - \varepsilon_p N + \varepsilon_p^2\varepsilon_+^2 N^2\\ &\quad + \varepsilon_+^2\varepsilon_p(1-\varepsilon_p)N - 2\varepsilon_+^2\varepsilon_p N^2 + \varepsilon_+^2 N^2\\ &\quad - \varepsilon_+^2 N + \varepsilon_+^2\varepsilon_p N + 2\varepsilon_+\varepsilon_p N^2\\ &\quad - 2\varepsilon_+\varepsilon_p^2 N^2 - 2\varepsilon_+\varepsilon_p(1-\varepsilon_p)N\\ &= \varepsilon_p^2(N^2-N) + \varepsilon_+^2\varepsilon_p^2(N^2-N) + \varepsilon_+^2\varepsilon_p N\\ &\quad - 2\varepsilon_+^2\varepsilon_p N^2 + \varepsilon_+^2(N^2-N) + \varepsilon_+^2\varepsilon_p N\\ &\quad + 2\varepsilon_+\varepsilon_p N^2 - 2\varepsilon_+\varepsilon_P^2 N^2 - 2\varepsilon_+\varepsilon_p N + 2\varepsilon_+\varepsilon_p^2 N\\ &= \left(\varepsilon_p^2 + \varepsilon_+^2 + \varepsilon_+^2\varepsilon_p^2\right)(N^2-N) - 2\varepsilon_+^2\varepsilon_p(N^2-N)\\ &\quad + 2\varepsilon_+\varepsilon_p(N^2-N) - 2\varepsilon_+\varepsilon_p^2(N^2-N)\end{aligned}$$

$$\langle N_{++}\rangle = \frac{1}{2}[\varepsilon_p + \varepsilon_+(1-\varepsilon_p)]^2(N^2-N) \tag{A6}$$

and

$$\langle N_{--}\rangle = \tfrac{1}{2}[\varepsilon_p + \varepsilon_-(1-\varepsilon_p)]^2(N^2-N). \tag{A7}$$

Finally we need to average over all N to get the foreground unlike-sign pairs:

$$\begin{aligned}\langle \mathrm{FG}_{+-}\rangle &= \sum_N \langle N_{+-}\rangle P(N)\\ &= [\varepsilon_p + \varepsilon_+(1-\varepsilon_p)][\varepsilon_p + \varepsilon_-(1-\varepsilon_p)]\\ &\quad \times (\langle N^2\rangle - \langle N\rangle) + \varepsilon_p\langle N\rangle\\ &\equiv \langle \mathrm{BG}_{+-}\rangle + \langle \mathrm{S}\rangle.\end{aligned} \tag{A8}$$

The unlike-sign foreground FG_{+-} consists of the sum of the unlike-sign background BG_{+-} and the signal $S = \varepsilon_p\langle N\rangle$. Similarly the like-sign foreground is calculated as:

$$\begin{aligned}\langle \mathrm{FG}_{++}\rangle &= \sum_N \langle N_{++}\rangle P(N)\\ &= \frac{1}{2}[\varepsilon_p + \varepsilon_+(1-\varepsilon_p)]^2(\langle N^2\rangle - \langle N\rangle)\\ &\equiv \langle \mathrm{BG}_{++}\rangle\end{aligned} \tag{A9}$$

$$\begin{aligned}\langle \mathrm{FG}_{--}\rangle &= \sum_N \langle N_{--}\rangle P(N)\\ &= \frac{1}{2}[\varepsilon_p + \varepsilon_-(1-\varepsilon_p)]^2(\langle N^2\rangle - \langle N\rangle)\\ &\equiv \langle \mathrm{BG}_{--}\rangle.\end{aligned} \tag{A10}$$

The like-sign foreground contains no signal.

So due to the fact that electrons and positrons are always created in pairs, the unlike-sign background is the geometric mean of the like-sign backgrounds, independent of the primary multiplicity distribution

$$\langle BG_{+-}\rangle = 2\sqrt{\langle BG_{++}\rangle\langle BG_{--}\rangle}. \tag{A11}$$

Let us compare the background to the product of the average track multiplicities. For a fixed n_p:

$$\begin{aligned}\langle n_+\rangle &= \sum_{n_+=1}^{N-n_p}(n_p + n_+)\omega(n_+)\\ &= n_p + \langle n_+\rangle\\ &= n_p + \varepsilon_+(N-n_p)\end{aligned} \tag{A12}$$

averaged over all possible n_p:

$$\begin{aligned}\langle N_+\rangle &= \sum_{n_p=0}^{N}\langle n_+\rangle\omega(n_p)\\ &= \varepsilon_p N + \varepsilon_+ N - \varepsilon_+\varepsilon_p N\\ &= [\varepsilon_p + \varepsilon_+(1-\varepsilon_p)]N\end{aligned} \tag{A13}$$

or averaged over all possible N:

$$\begin{aligned}\langle FG_+\rangle &= \sum_N \langle N_+\rangle P(N)\\ &= [\varepsilon_p + \varepsilon_+(1-\varepsilon_p)]\langle N\rangle\end{aligned} \tag{A14}$$

and thus:

$$\langle \mathrm{FG}_+\rangle\langle \mathrm{FG}_-\rangle = [\varepsilon_\mathrm{p} + \varepsilon_+(1-\varepsilon_\mathrm{p})][\varepsilon_\mathrm{p} + \varepsilon_-(1-\varepsilon_\mathrm{p})]\langle \mathrm{N}\rangle^2 \tag{A15}$$

or

$$\frac{\langle \mathrm{BG}_{+-}\rangle}{\langle \mathrm{FG}_+\rangle\langle \mathrm{FG}_-\rangle} = 1 + \frac{\sigma^2 - \langle N\rangle}{\langle N\rangle^2}. \tag{A16}$$

So in general $\langle \mathrm{BG}_{+-}\rangle \neq \langle \mathrm{FG}_+\rangle\langle \mathrm{FG}_-\rangle$, except for the special case that $P(N)$ is a Poisson distribution. Note this is the opposite conclusion one derives in the case that the sources of + and − tracks are independent, i.e., + and − tracks are produced as singles and not as pairs as in the case of muons. In that case $\langle \mathrm{FG}_+\rangle\langle \mathrm{FG}_-\rangle$ is the correct background normalization.

APPENDIX B: RELATION BETWEEN REAL PHOTONS, VIRTUAL PHOTONS, AND ELECTRON PAIRS

1. Introduction

Figure 49 illustrates that, in general, any source of high-energy real photons can also emit virtual photons that materialize into electron pairs. On the left side a real photon is emitted by a source labeled as $M(Q^2 = 0)$. On the right side is an analogous diagram, where a virtual photon with mass m_{γ^*} is emitted. The virtual photon can then convert to an e^+e- pair if $m_{\gamma^*} > 2m_e$. This e^+e^- pair production process is a QED correction to the real photon production process and is often called internal conversion.

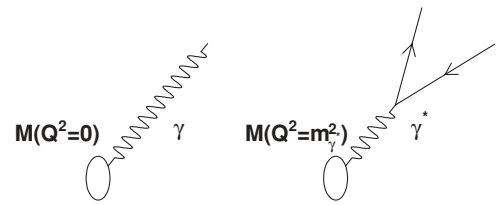

FIG. 49. Diagram for real photon production (left) and its associated process producing an e^+e^- pair (right). M stands for the matrix element of the photon-producing process, and Q is the four-momentum of the virtual (or real) photon.

In the energy region, where electroweak effects are negligible, an electron pair can only be produced through a virtual photon. (Here we do not include e^+e^- pairs from correlated weak decays such as $c\bar{c} \to e^+e^-$.) Thus any electron pair production process can be described as production of a virtual photon and its subsequent decay into an e^+e^-pair.

The yields of virtual photons dN_{γ^*} and electron pairs dN_{ee} are related:

$$\frac{d^2N_{ee}}{dM^2} = \frac{\alpha}{3\pi}\frac{L(M)}{M^2}dN_{\gamma^*}, \tag{B1}$$

$$L(M) = \sqrt{1-\frac{4m_e^2}{M^2}}\left(1+\frac{2m_e^2}{M^2}\right), \tag{B2}$$

where M is the mass of the virtual photon or the electron pair ($M = m_{\gamma^*} = m_{ee}$) and α is the fine structure constant ($\alpha \simeq 1/137$). The factor, $\frac{\alpha}{3\pi}\frac{L(M)}{M^2}$, is a universal factor describing the decay of the virtual photon into an e^+e^- pair. This relation is exact to first order in the electromagnetic coupling α.

Equation (B1) can be written as

$$\frac{d^2N_{ee}}{dM^2} = \frac{\alpha}{3\pi}\frac{L(M)}{M^2}S(M,q)dN_{\gamma}. \tag{B3}$$

Here q is the three-momentum of the virtual photon and we have introduced $S(M,q) = dN_{\gamma^*}(M)/dN_{\gamma}$ to factor out the difference between real photon emission and virtual photon emission. The factor $S(M,q)$ is process dependent and accounts for effects such as form factors, phase space, and spectral functions. $S(M,q)$ approaches 1 for small M, $S(M,q) \to 1$ for $M \to 0$. Additionally, since $L(M) \simeq 1 - 6m_e^4/M^4$ for $m_e \ll M$, $L(M) = 1$ is a very good approximation. Thus the relationship between the electron pair yield and the direct photon yield simplifies to

$$\frac{d^2N_{ee}}{dM^2} \simeq \frac{\alpha}{3\pi}\frac{1}{M^2}dN_{\gamma}, \tag{B4}$$

$$\frac{d^2N_{ee}}{dM} \simeq \frac{2\alpha}{3\pi}\frac{1}{M}dN_{\gamma}. \tag{B5}$$

The relation between real photon production and electron pair production shown by Eq. (B5) is valid if $M \ll E_{\gamma}$, i.e., if the virtual photon is quasireal. In this region, the yield of electron pairs in the mass range $m_1 < M < m_2$ is related to the photon yield as

$$dN_{ee}(m_1 < M < m_2) \simeq \int_{m_1}^{m_2}\frac{2\alpha}{3\pi}\frac{1}{M}dN_{\gamma} \tag{B6}$$

$$\simeq \frac{2\alpha}{3\pi}\log\frac{m_2}{m_1}dN_{\gamma}. \tag{B7}$$

In the following, we discuss two examples of internal conversions: Dalitz decays and high p_T Drell-Yan production. We then discuss the relationship between direct photons and electron pairs from thermal sources. At the end, we illustrate the relationship between electron pairs and virtual photons using a theoretical model calculation.

2. Dalitz decays

Dalitz decays of pseudoscalar and vector mesons are prime examples of internal conversion. In these processes, a virtual photon, instead of a real photon, is emitted in the decay of a hadron and subsequently decays into an e^+e^- pair. The relation between $A \to Be^+e^-$ and $A \to B\gamma$ is given by [76]

$$\frac{d\Gamma(A \to Be^+e^-)}{dM^2} = \frac{\alpha}{3\pi}\frac{L(M)}{M^2}S_{\rm AB}(M)\Gamma(A \to B\gamma), \tag{B8}$$

$$S_{\rm AB}(M) = |F_{\rm AB}(M^2)|^2\left[\left(1+\frac{M^2}{m_A^2-m_B^2}\right)^2 - \frac{4m_A^2M^2}{(m_A^2-m_B^2)^2}\right]^{3/2}, \tag{B9}$$

where m_A and m_B are the mass of hadrons A and B and $F_{\rm AB}$ is the electromagnetic transition form factor. $S_{AB}(M)$ here is an example of $S(M,q)$ in Eq. (B3). For decays of pseudoscalar mesons ($P = \pi^0, \eta, \eta'$), the relationship between the photonic decay ($P \to \gamma\gamma$) and the corresponding Dalitz decay ($P \to e^+e^-\gamma$) is given by the well known Kroll-Wada formula [74,76].

$$\frac{d\Gamma(P \to e^+e^-\gamma)}{dM^2} = \frac{2\alpha}{3\pi}\frac{L(M)}{M^2}S_{\rm KW}(M)\Gamma(P \to \gamma\gamma),$$

$$S_{\rm KW}(M) = F_P(M^2)|^2\left(1-\frac{M^2}{m_P^2}\right)^3, \tag{B10}$$

where m_P is the meson mass and $F_P(M^2)$ is the electromagnetic form factor. Note that the factor 2 in $\frac{2\alpha}{3\pi}$ accounts for the fact that each of the two decay photons can convert to an electron pair. The form factor is usually parameterized as $F_P(Q^2) = 1/(1 - Q^2/\Lambda_P^2)$. Experimental measurements of the transition form factor by Lepton-G [75] and Cello [101] show $\Lambda_P \simeq M_{\rho}$, consistent with the VDM.

3. High p_T Drell-Yan process

In $p+p$ collisions, the cross section for Drell-Yan electron pair production can be expressed in terms of the cross section for virtual photon production as follows [102]:

$$\frac{d^3\sigma_{pp\to l^+l^-X}}{dM^2dp_T^2dy} = \frac{\alpha}{3\pi}\frac{L(M)}{M^2}\frac{d^2\sigma_{pp\to\gamma^*X}}{dp_T^2dy}, \tag{B11}$$

where M, p_T, and y are the mass, the transverse momentum, and the rapidity of the virtual photon. For $p_T \gg M$, the virtual photon cross section becomes equal to the real photon cross section ($d\sigma_{\gamma^*} \to d\sigma_{\gamma}$ as $M/p_T \to 0$). Thus the electron pair cross section can be described as

$$\frac{d\sigma_{pp\to e^+e^-X}}{dM^2dp_T^2dy} \simeq \frac{\alpha}{3\pi}\frac{L(M)}{M^2}\frac{d\sigma_{pp\to\gamma X}}{dp_T^2dy}. \tag{B12}$$

Direct photon production via gluon-Compton scattering ($q + g \to q + \gamma$) has an associated electron pair production process ($q + g \to q + \gamma^* \to q + e^+e^-$). For the lowest-order pQCD calculation, the following relation between the two

processes is obtained by an explicit calculation,

$$\frac{d^2\sigma_{ee}}{dM^2dt} = \frac{\alpha}{3\pi}\frac{L(M)}{M^2}\frac{d\sigma_\gamma}{dt} \times S_{qg}(u,t,s), \tag{B13}$$

where

$$S_{qg}(u,t,s) = \left(1 + \frac{2u}{t^2+s^2}M^2\right) = 1 - \frac{2x}{(x+\sqrt{1+x^2})(3x^2+1+2x\sqrt{1+x^2})}. \tag{B14}$$

Here $x = M/p_T$ and s, t, u are the Mandelstam variables defined as $s = (p+k)^2$, $t = (p-k')^2$, $u = (p-p')^2$; p, k, k', p' are four-momenta of the incoming quark, the incoming gluon, the outgoing (virtual or real) photon, and the outgoing quark, respectively. The factor $S_{qg}(u,t,s)$ accounts for the difference between the virtual photon cross section and the real photon cross section, and $S_{qg}(u,t,s)$ becomes unity for small M. It is an example of $S(M,q)$ in Eq. (B3). For 90° scattering in the center-of-mass system, $S_{qg} \simeq (1 - M^2/5p_T^2)$. Thus $S_{qg} \to 1$ as $M^2/p_T^2 \to 0$. This means that the approximation $S_{qg} \simeq 1$ is valid as long as $M^2/p_T^2 \ll 1$ even if M is relatively large.

In a kinematic region, where M/p_T is not very large, contributions from parton fragmentation into direct photon (real and virtual) become significant. Unfortunately hadronic effects in parton fragmentation into photons are poorly understood. Kang, Qui, and Vogelsang discussed [102] the theoretical uncertainties in this process. However, the uncertainty due to this effect is relatively small, except for very low p_T ($p_T \lesssim 1$ GeV/c) [102].

4. Thermal radiation

In heavy-ion collisions, thermal radiation from the hot and dense matter formed in the collision may contribute to both real direct photon production and electron pair production. The emission rate of electron pairs per space-time volume from a thermal source can be described in terms of the electromagnetic (EM) spectral function as [26,103]

$$\frac{dR_{ee}}{d^4q} = -\frac{\alpha^2}{3\pi^3}\frac{L(M)}{M^2}\mathrm{Im}\Pi^\mu_{em,\mu}(M,q;T)f^B(q_0,T) \tag{B15}$$

$$= -\frac{\alpha^2}{3\pi^3}\frac{L(M)}{M^2}\mathrm{Im}\left(2\Pi^T_{em} + \Pi^L_{em}\right)f^B(q_0,T). \tag{B16}$$

Here Π^T_{em} and Π^L_{em} are the transverse and the longitudinal components of the in-medium photon self-energy tensor $\Pi^\mu_{em,\nu}$, and $f^B(q_0,T) = 1/(e^{q_0/T} - 1)$ is the Boltzmann factor.

Using the same notation, the emission rate of virtual photons is described as [26,104]

$$q_0\frac{dR_{\gamma^*}}{d^3q} = -\frac{\alpha}{2\pi^2}\mathrm{Im}\Pi^\mu_{em,\mu}(M,q;T)f^B(q_0,T). \tag{B17}$$

The real photon emission rate is obtained in the limit of $M \to 0$. The longitudinal polarization contribution Π^L_{em} vanishes for real photons: $\Pi^T_{em}(M,q;T) \to \Pi^T_{em}(0,q;T)$, $\Pi^L_{em}(M,q;T) \to 0$ for $M \to 0$. The real photon emission rate is given by

$$q_0\frac{dR_\gamma}{d^3q} = -\frac{\alpha}{\pi^2}\mathrm{Im}\Pi^T_{em}(M=0,q;T)f^B(q_0,T). \tag{B18}$$

The virtual photon and electron pair emission rates are thus related by

$$q_0\frac{dR_{ee}}{dM^2d^3q} = \frac{1}{2}\frac{dR_{ee}}{d^4q} = \frac{\alpha}{3\pi}\frac{L(M)}{M^2}q_0\frac{dR_{\gamma^*}}{d^3q}, \tag{B19}$$

$$q_0\frac{dR_{ee}}{dM^2d^3q} \simeq \frac{\alpha}{3\pi}\frac{L(M)}{M^2}q_0\frac{dR_\gamma}{d^3q}. \tag{B20}$$

Note that Eq. (B19), describing the relationship between the virtual photon and electron pair emission, is exact to order α in QED and is exact to all orders of the strong coupling constant. Note also that this relationship between electron pairs and photons is the same as that shown in Eq. (B11). This reflects the fact that an e^+e^- pair can only be produced through virtual photon and that the conversion rate of a virtual photon into an e^+e^- pair is described by a universal factor, $\frac{\alpha}{3\pi}\frac{L(M)}{M^2}$. Equation (B20) is equivalent to Eq. (B12) and is an approximation for small M, where $dR^*_\gamma \simeq dR_\gamma$.

The relations above are for the emission rates per space-time volume. The yields dN_{ee} and dN_γ are obtained from space-time integral over the rates.

$$\frac{d^2N_{ee}}{dM^2} = \frac{\alpha}{3\pi}\frac{L(M)}{M^2}dN_{\gamma^*}, \tag{B21}$$

$$\frac{d^2N_{ee}}{dM} = \frac{2\alpha}{3\pi}\frac{L(M)}{M}dN_{\gamma^*} \tag{B22}$$

$$= \frac{2\alpha}{3\pi}\frac{L(M)}{M}S(M,q)dN_\gamma. \tag{B23}$$

These are the same equations as Eq. (B1)–(B3). Here, following Eq. (B3), the difference between real and virtual photons is factored out in $S(M,q)$. The $S(M,q)$ factor for radiation from thermal sources can be written as

$$S(M,q) = \frac{\left\langle \mathrm{Im}\left(2\Pi^T_{em}(M,q) + \Pi^L_{em}(M,q)\right)f^B(q_0)\right\rangle}{\left\langle \mathrm{Im}2\Pi^T_{em}(0,q)f^B(q_0;M=0)\right\rangle}, \tag{B24}$$

Here $\langle\ \rangle$ indicates the space-time average.

Deviation of $S(M,q)$ from unity can arise from nonzero $\Pi^L_{em}(M,q)$ in the medium and a change of $\Pi^T_{em}(M,q)$ from $\Pi^T_{em}(0,q)$. The behavior of Π^T_{em} and Π^L_{em} is model dependent. However, on very general grounds we can conclude that the in-medium spectral function Π_{em} is a smooth function of M for the low-mass region ($M <$ a few 100 MeV/c^2).

Hadronic interactions yield and almost flat behavior in $S(M)$ as we see in a model calculation by Rapp later. $q+g$ scattering gives an almost flat contribution in $S(M)$; see S_{qg} of gluon Compton scattering. As we see later, the contribution from $q\bar{q}$ annihilation is not constant and is $\propto M^2$ [see Eq. (B27)]. This means that it is strongly suppressed in the low-mass region relative to hadronic and qg-scattering contributions. Thus $S(M,q)$ is a smooth and almost constant function of M at low masses. Furthermore, the short time

($\leqslant$1 fm/c) between rescattering among hadrons and partons in the medium should smear any feature in $S(M)$ smaller than a mass scale of a few 100 MeV/c^2.

5. Conversion of e^+e^- pairs to virtual photons

Equation (B21) can be used to determine the virtual photon yield from the electron pair yield. The equation can be rewritten as

$$q_0 \frac{dN_{\gamma^*}}{d^3q} = S(M,q) q_0 \frac{dN_\gamma}{d^3q} \tag{B25}$$

$$\simeq \frac{3\pi}{2\alpha} M q_0 \frac{dN_{ee}}{d^3q dM}. \tag{B26}$$

Using this relationship, the virtual photon spectrum as a function of mass M and p_T can be determined from the double differential electron pair spectrum. In particular, the mass dependence for a given p_T bin can be measured. This is a direct measurement of the shape of the $S(M,q)$ function and the shape of $\langle \mathrm{Im}\Pi^{em}(M,T) f^B(T) \rangle$ as a function of M. The real photon yield is then obtained by extrapolation of $dN_{\gamma^*}(M)$ to the $M \to 0$ limit.

6. Electron pairs and virtual photons in a theoretical model calculation

Figure 50 illustrates the relationship between the electron pair mass spectrum and the virtual photon cross section. Figure 50(a) shows the double differential electron pair spectrum, $(1/p_T) dN_{ee}/dM dp_T dy$ at $p_T = 1.525$ GeV/c, from a model calculation of electron pair production by Rapp [85]. The dashed and solid curve show electron pairs from the hadronic gas. The calculation shown in the dashed curve uses the spectral function Π_{em} that is unchanged from its vacuum value so the line shapes of vector mesons (ρ, ω, ϕ) are unmodified. The calculation shown in the solid curve, uses a spectral function calculated by a model Lagrangian of hadronic many-body interactions, and the line shapes of vector mesons are broadened due to the interactions. It also includes the contributions like $a_1(1260) \to \pi + e^+e^-$, $\rho \to \pi + e^+e^-$, and $N + \pi \to N^* \to N e^+e^-$ that fill out the low-mass regions below two-pion threshold. In the low-mass region, the mass spectrum steeply increases with decreasing M. This steep behavior is due to the $1/M$ factor in $\gamma^* \to e^+e^-$. The dotted curve shows the contribution from the leading order (LO) $q\bar{q}$ annihilation that is augmented with a $q = 0$ hard thermal loop (HTL) correction factor [105].

Figure 50(b) shows the same calculations presented as the differential yield of virtual photons as a function of mass. The electron pair yield shown in Fig. 50(a) is converted to the virtual photon yield using Eq. (B26). In this plot, the solid curve becomes almost constant for $M < 0.3$ GeV. The steep $1/M$ behavior of the electron pair spectrum is removed, and much more smooth behavior of the virtual photon spectrum is revealed. The plot shows that the virtual photon yield is almost constant as function of M. The value of the solid curve at $M = 0$ corresponds to the real photon yield. Thus in this model calculation, the yield of virtual photons for $0.1 < M < 0.3$ GeV is almost the same as that of real photons. The solid curve illustrates that in a consistent theory calculation the yield of virtual photons is a smooth function of M and it becomes the real photon yield in the limit of $M = 0$, $dN^*_\gamma(M, p_T) \to dN_\gamma(p_T)$ as $M \to 0$.

The flat behavior of the solid curve in this low-mass region comes from the fact that hadronic scattering processes such as $a_1(1260) \to \pi + e^+e^-$, $\rho \to \pi + e^+e^-$, and $N + \pi \to N^* \to N e^+e^-$ dominate this low-mass region. These processes are internal conversion of the corresponding real photon production processes, i.e., $a_1 \to \pi + \gamma$, $\rho \to \pi + \gamma$, $N + \pi \to N + \gamma$. Thus production of virtual photons from these processes should be very close to that of real photons at low mass. In the language of the spectral function Π_{em}, these processes contribute to Π_{em} at $M = 0$ as well as $M > 0$. Their

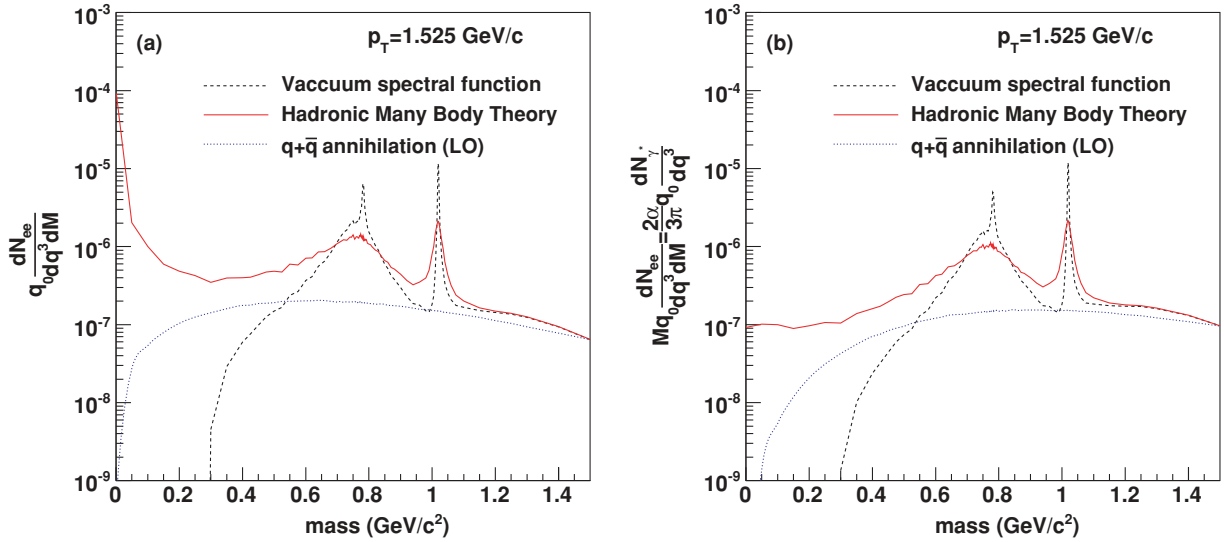

FIG. 50. (Color online) (a) Electron pair emission rate and (b) virtual photon emission rate calculations at a fixed pair $p_T = 1.525$ GeV/c [85]. The solid curve shows the hadronic many-body theory in the medium. The dashed curve shows the calculation when the EM spectral function in the vacuum is used. The dotted curve shows the $q\bar{q}$ annihilation contribution.

contribution to Π_{em} is a smooth, almost a constant function of virtual photon mass M.

In Fig. 50(b), the contribution from $q\bar{q}$ annihilation is shown by the dotted curve. In perturbation theory, the $q\bar{q}$ contribution is given by

$$\mathrm{Im}\Pi_{em}(M) = \frac{M^2}{12\pi}\left(1 + \frac{\alpha_s}{\pi} + \cdots\right) N_c \Sigma(e_q)^2. \qquad \text{(B27)}$$

The quark annihilation contribution behaves as $\propto M^2$ in the low-mass region. Thus it is strongly suppressed and has little contribution in the low-mass region. In the high-mass region, the M^2 behavior of the quark annihilation is suppressed by the Boltzmann factor.

There is a large uncertainty in the approximation used in the dotted curve, and it is shown here just to illustrate that the $q\bar{q}$ annihilation contribution is subleading contribution in the low-mass region ($M <$ a few 100 MeV/c^2). Many effects can alter the shape and magnitude of the $q\bar{q}$ contribution. The calculation shown in Fig. 50 uses zero quark mass. The effective quark mass in the medium is uncertain, but in most theoretical calculations it is the order of the temperature of the medium. Quarks in the medium should also have a large width (more than a few 100 MeV/c^2) due to the short time between interactions. A nonzero effective quark mass would further suppress the quark annihilation contribution in the very low-mass region while a finite quark width would smear the M^2 behavior and can cause nonzero $q\bar{q}$ contribution at $M = 0$.

It should be noted that the dotted curve does not include processes like $q + g \to q + \gamma^*$ that are associated with real direct photon production. This is because HTL calculation of thermal radiation from QGP is available only in the real photon case. Contributions from processes associated with real photon production can be much larger than those from the LO $q\bar{q}$ annihilation shown in Fig. 50 in the low-mass region. Turbide, Gale, and Rapp [98] calculated real photon production in a hadronic gas using the same model and compared it with real photon production in the QGP phase using the complete leading order HTL analysis. They found that real photons from the QGP outshine those from a hadronic gas for $p_T > 1.5$ GeV/c in Au+Au collisions at RHIC. Since the virtual photon yield should be continuous from $M = 0$ (i.e., real photons) to $M > 0$, this implies that the contribution from the QGP, including processes like $q + g \to q + \gamma^*$, is as large as or even greater than that shown in the solid curve in Fig. 50(b) in the low-mass and high-p_T region (i.e., $M <$ a few 100 MeV/c^2 and $p_T > 1.5$ GeV/c^2) at RHIC energies.

[1] K. Adcox *et al.* (PHENIX Collaboration), Nucl. Phys. A **757**, 184 (2005).
[2] S. S. Adler *et al.* (PHENIX Collaboration), Phys. Rev. C **71**, 034908 (2005).
[3] K. Adcox *et al.* (PHENIX Collaboration), Phys. Rev. Lett. **88**, 022301 (2002).
[4] S. S. Adler *et al.* (PHENIX Collaboration), Phys. Rev. Lett. **96**, 202301 (2006).
[5] S. S. Adler *et al.* (PHENIX Collaboration), Phys. Rev. Lett. **96**, 032301 (2006).
[6] A. Adare *et al.* (PHENIX Collaboration), Phys. Rev. Lett. **98**, 172301 (2007).
[7] S. S. Adler *et al.* (PHENIX Collaboration), Phys. Rev. Lett. **91**, 182301 (2003).
[8] A. Adare *et al.* (PHENIX Collaboration), Phys. Rev. Lett. **98**, 162301 (2007).
[9] S. Afanasiev *et al.* (PHENIX Collaboration), Phys. Rev. Lett. **99**, 052301 (2007).
[10] P. Stankus, Annu. Rev. Nucl. Part. Sci. **55**, 517 (2005).
[11] R. Rapp and E. Shuryak, Phys. Lett. B **473**, 13 (2000).
[12] T. Matsui and H. Satz, Phys. Lett. B **178**, 416 (1986).
[13] P. Braun-Munzinger and J. Stachel, Phys. Lett. B **490**, 196 (2000); P. Braun-Munzinger, K. Redlich, and J. Stachel, *Quark Gluon Plasma, Vol. 3* (World Scientific, Singapore, 2003).
[14] R. L. Thews, M. Schroedter, and J. Rafelski, Phys. Rev. C **63**, 054905 (2001).
[15] R. Rapp, Phys. Rev. C **63**, 054907 (2001).
[16] K. Gallmeister, B. Kampfer, and O. P. Pavlenko, Phys. Rev. C **57**, 3276 (1998); B. Kaempfer, O. P. Pavlenko, and K. Gallmeister, Phys. Lett. B **419**, 412 (1998).
[17] E. V. Shuryak, Phys. Rev. C **55**, 961 (1997); C. M. Hung, and E. V. Shuryak, *ibid.* **56**, 453 (1997).
[18] R. Rapp, SUNY-NTG-02-13, Apr 2002. 10pp. Contributed to 18th Winter Workshop on Nuclear Dynamics, 20–22 January 2002 (SUNY, Stony Brook, Nassau, Bahamas), arXiv:nucl-th/0204003; W. Liu and R. Rapp, Nucl. Phys. A **796**, 101 (2007).
[19] K. Dusling and I. Zahed, Nucl. Phys. A **825**, 212 (2009); K. Dusling, Ph.D. thesis, Stony Brook University (2008).
[20] E. L. Bratkovskaya, W. Cassing, and O. Linnyk, Phys. Lett. B **670**, 428 (2009).
[21] G. E. Brown and M. Rho, Phys. Rev. Lett. **66**, 2720 (1991).
[22] J. H. Cobb *et al.*, Phys. Lett. B **78**, 519 (1978).
[23] C. Albajar *et al.* (UA1 Collaboration), Phys. Lett. B **209**, 397 (1988).
[24] M. Masera (HELIOS/3 Collaboration), Nucl. Phys. A **590**, 103c (1995).
[25] G. Agakichiev *et al.* (CERES Collaboration), Phys. Rev. Lett. **75**, 1272 (1995).
[26] R. Rapp, and J. Wambach, Adv. Nucl. Phys. **25**, 1 (2000), and references therein.
[27] W. Cassing and E. Bratkovskaya, Phys. Rep. **308**, 65 (1999), and references therein.
[28] R. Arnaldi *et al.* (NA60 Collaboration), Phys. Rev. Lett. **96**, 162302 (2006).
[29] G. Agakichiev *et al.* (CERES Collaboration), Eur. Phys. J. **41**, 475 (2005).
[30] D. Adamova *et al.* (CERES Collaboration), Phys. Lett. B **666**, 425 (2008).
[31] G. Agakichiev *et al.* (HADES Collaboration), Phys. Rev. Lett. **98**, 052302 (2007).
[32] R. Arnaldi *et al.* (NA60 Collaboration), Phys. Rev. Lett. **100**, 022302 (2008).
[33] A. L. S. Angelis *et al.* (HELIOS/3 Collaboration), Eur. Phys. J. **13**, 433 (2000).
[34] M. C. Abreu *et al.* (NA38 Collaboration), Phys. Lett. B **368**, 230 (1996).
[35] M. C. Abreu *et al.* (NA50 Collaboration), Eur. Phys. J. **14**, 443 (2000).

[36] R. Arnaldi *et al.* (NA60 Collaboration), Eur. Phys. J. **61**, 711 (2009).

[37] S. Afanasiev *et al.* (PHENIX Collaboration), arXiv:0706.3034 [nucl-ex] (to be published).

[38] A. Adare *et al.* (PHENIX Collaboration), Phys. Lett. B **670**, 313 (2009).

[39] A. Adare *et al.* (PHENIX Collaboration), arXiv:0804.4168 [nucl-ex] (to be published).

[40] K. Adcox *et al.* (PHENIX Collaboration), Nucl. Instrum. Methods **499**, 469 (2003).

[41] C. Adler *et al.* (PHENIX Collaboration), Nucl. Instrum. Methods **470**, 488 (2001).

[42] S. H. Aronson *et al.* (PHENIX Collaboration), Nucl. Instrum. Methods **499**, 480 (2003).

[43] K. Adcox *et al.* (PHENIX Collaboration), Nucl. Instrum. Methods **499**, 489 (2003).

[44] M. Aizawa *et al.* (PHENIX Collaboration), Nucl. Instrum. Methods **499**, 508 (2003).

[45] L. Aphecetche *et al.* (PHENIX Collaboration), Nucl. Instrum. Methods **499**, 521 (2003).

[46] M. Allen *et al.* (STAR Collaboration), Nucl. Instrum. Methods **499**, 549 (2003).

[47] K. Adcox *et al.* (PHENIX Collaboration), Phys. Rev. Lett. **86**, 3500 (2001).

[48] A. Adare *et al.* (PHENIX Collaboration), Phys. Rev. Lett. **97**, 252002 (2006).

[49] S. S. Adler *et al.* (PHENIX Collaboration), Phys. Rev. Lett. **96**, 012304 (2006).

[50] K. Adcox *et al.* (PHENIX Collaboration), Phys. Rev. Lett. **87**, 052301 (2001).

[51] T. Sjöstrand *et al.*, Comput. Phys. Commun. **135**, 238 (2001); we used PYTHIA 6.319 with MSEL = 0 and the following processes switched on: MSUB 11, 12, 13, 28, 53, 68, PARP(91) = 1.5 ($\langle k_t \rangle$), MSTP(32) = 4 (Q^2 scale), and CKIN(3) = 2.0 (min. parton p_T).

[52] A. Adare *et al.* (PHENIX Collaboration), Phys. Rev. C **78**, 014901 (2008).

[53] GEANT User's Guide, 3.15, CERN Program Library.

[54] W. M. Yao *et al.* (Particle Data Group), J. Phys. G **33**, 1 (2006).

[55] We used PYTHIA 6.152 with parameters as in K. Adcox *et al.* (PHENIX Collaboration), Phys. Rev. Lett. **88**, 192303 (2002); CTEQ5L PDF as in H. L. Lai *et al.*, Eur. Phys. J. **12**, 375 (2000).

[56] A. Adare *et al.* (PHENIX Collaboration, in preparation).

[57] A. Adare *et al.* (PHENIX Collaboration), Phys. Rev. D **76**, 051106 (2007).

[58] S. S. Adler *et al.* (PHENIX Collaboration), Phys. Rev. C **74**, 024904 (2006).

[59] S. S. Adler *et al.* (PHENIX Collaboration), Phys. Rev. Lett. **91**, 072301 (2003).

[60] S. S. Adler *et al.* (PHENIX Collaboration), Phys. Rev. C **69**, 034909 (2004).

[61] S. S. Adler *et al.* (PHENIX Collaboration), Phys. Rev. C **75**, 024909 (2007).

[62] S. S. Adler *et al.* (PHENIX Collaboration), Phys. Rev. C **75**, 051902 (2007).

[63] Y. Riabov *et al.* (PHENIX Collaboration), J. Phys. G **34** No.8, S925 (2007).

[64] A. Adare *et al.* (PHENIX Collaboration), Phys. Rev. Lett. **98**, 232002 (2007).

[65] S. S. Adler *et al.* (PHENIX Collaboration), Phys. Rev. C **72**, 014903 (2005).

[66] A. Adare *et al.* (PHENIX Collaboration), Phys. Rev. Lett. **98**, 232301 (2007).

[67] V. Ryabov, Nucl. Phys. A **827**, 1–4, 395c (2009).

[68] A. Milov, *Proc. of 15th Int. Workshop on Deep Inelastic Scattering and Related Subjects, Munich*, 731 (2007); http://dx.doi.org/10.3360/dis.2007.127; arXiv:0707.1258 [nucl-ex]; Y. Nakamiya, J. Phys. G: Nucl. Part. Phys. **35**, 104158 (2008).

[69] R. Gavai *et al.*, Int. J. Mod. Phys. A **10**, 3043 (1995).

[70] C. da Silva, Nucl. Phys. A **830**, 227C, (2009).

[71] A. Milov, Eur. Phys. J. **61**, 721 (2009).

[72] M. Naglis, Eur. Phys. J. **61**, 835 (2009).

[73] J. Manninen, and F. Becattini, Phys. Rev. C **78**, 054901 (2008).

[74] N. M. Kroll and W. Wada, Phys. Rev. **98**, 1355 (1955).

[75] R. I. Dzhelyadin *et al.*, Phys. Lett. B **102**, 296 (1981).

[76] L. G. Landsberg, Phys. Rep. **128**, 301 (1985).

[77] G. J. Gounaris and J. J. Sakurai, Phys. Rev. Lett. **21**, 244 (1968).

[78] M. Cacciari, P. Nason, and R. Vogt, Phys. Rev. Lett. **95**, 122001 (2005).

[79] K. Adcox *et al.* (PHENIX Collaboration), Nucl. Phys. A **757**, 184 (2005).

[80] L. E. Gordon and W. Vogelsang, Phys. Rev. D **48**, 3136 (1993); W. Vogelsang (private communication, 2008).

[81] S. S. Adler *et al.* (PHENIX Collaboration), Phys. Rev. Lett. **94**, 232301 (2005).

[82] S. S. Adler *et al.* (PHENIX Collaboration), Phys. Rev. Lett. **98**, 012002 (2007).

[83] S. S. Adler *et al.* (PHENIX Collaboration), Phys. Rev. Lett. **91**, 241803 (2003).

[84] G. Agakichiev *et al.* (CERES Collaboration), Eur. Phys. J. **4**, 231 (1998).

[85] R. Rapp (private communication). The numerical table of the double differential yield of lepton pair based on the same theoretical model of [103] is provided by Rapp.

[86] R. Rapp *et al.*, Phys. Lett. B **417**, 1 (1998).

[87] R. Rapp and C. Gale, Phys. Rev. C **60**, 024903 (1999).

[88] F. Riek *et al.*, Phys. Lett. B **677**, 109 (2009).

[89] K. Dusling, D. Teaney, and I. Zahed, Phys. Rev. C **75**, 024908 (2007).

[90] K. Dusling (private communication). The numerical table of the double differential yield of lepton pair based on the same theoretical model of Ref. [19] is provided by Dusling; for more recent calculations see K. Dusling and I. Zahed, arXiv:0911.2426 [nucl-th].

[91] E. L. Bratkovskaya and W. Cassing, Nucl. Phys. A **807**, 214 (2008).

[92] E. L. Bratkovskaya (private communication). The numerical table of the double differential yield of lepton pair based on the same theoretical model of Ref. [20] is provided by Bratkovskaya.

[93] R. Rapp, Phys. Rev. C **66**, 017901 (2002).

[94] K. Dusling and I. Zahed, Nucl. Phys. A **825**, 212 (2009).

[95] D. d'Enterria and D. Peressounko, Eur. Phys. J. **46**, 451 (2006).

[96] P. Huovinen, P. V. Ruuskanen, and S. S. Rasanen, Phys. Lett. B **535**, 109 (2002).

[97] D. K. Srivastava and B. Sinha, Phys. Rev. C **64**, 034902 (2001).

[98] S. Turbide, R. Rapp, and C. Gale, Phys. Rev. C **69**, 014903 (2004).
[99] F. M. Liu, T. Hirano, K. Werner, and Y. Zhu, Phys. Rev. C **79**, 014905 (2009).
[100] Jan-e Alam, S. Sarkar, T. Hatsuda, T. K. Nayak, and B. Sinha, Phys. Rev. C **63**, 021901(R) (2001).
[101] H. J. Behrend *et al.* (CELLO Collaboration), Z. Phys. C **49**, 401 (1991).
[102] Z-B. Kang, J.-W. Qiu, and W. Vogelsang, Phys. Rev. D **79**, 054007 (2009).
[103] H. van Hees and R. Rapp, Nucl. Phys. A **806**, 339 (2008).
[104] S. Turbide, C. Gale, E. Frodermann, and U. Heinz, Phys. Rev. C **77**, 024909 (2008).
[105] E. Braaten, R. D. Pisarski, T.-C. Yuan, Phys. Rev. Lett. **64**, 2242 (1990).